

UNIVERSITÀ DEGLI STUDI DI TRIESTE

Facoltà di Scienze Matematiche, Fisiche e
Naturali

Corso di Laurea in Fisica

Tesi di Laurea Magistrale

**Search for a Standard Model Higgs
Boson in the Channel
 $VH \rightarrow VW$ With
Leptons and Hadronic τ in the Full
CDF Run II Data Set**



Relatore:
dott. Massimo CASARSA

Correlatore:
dott. Giuseppe DELLA RICCA

Laureando:
Gabriele BERTOLI

ANNO ACCADEMICO 2010-2011

*Alla mia famiglia,
† A Marta.*

Sommario

In questo lavoro viene presentato il risultato della ricerca a CDF di un bosone di Higgs che decade in una coppia di bosoni W con elettroni, muoni e tau adronici nello stato finale. In particolare, la ricerca viene effettuata nel canale con due leptoni ed un tau nello stato finale. In 9.7 fb^{-1} di dati ci aspettiamo 40.0 ± 5.4 eventi di fondo e 0.54 ± 0.05 eventi di segnale per un'ipotesi di massa del bosone di Higgs di $160 \text{ GeV}/c^2$, nei dati si contano 28 eventi. Viene stabilito un limite superiore al 95% C.L. su σ/σ_{SM} di 12.6 per un'ipotesi di massa del bosone di Higgs di $160 \text{ GeV}/c^2$. Il limite aspettato per lo stesso valore di massa risulta 12.4. Viene presentato lo stesso risultato anche per altre diciannove ipotesi di massa nell'intervallo di masse che va da $110 \text{ GeV}/c^2$ a $200 \text{ GeV}/c^2$.

Abstract

We present the results of the CDF search for a Standard Model Higgs boson decaying into a pair of W bosons with electrons, muons and hadronically decaying taus in the final state. In particular, we investigate a channel with three objects, two leptons and a tau. In 9.7 fb^{-1} of data we expect 40.0 ± 5.4 background events and 0.54 ± 0.05 signal events for a Higgs mass hypothesis of $160 \text{ GeV}/c^2$, whereas in data we count 28 events. We set a 95% C.L. upper limit on σ/σ_{SM} of 12.6 for a Higgs mass hypothesis of $160 \text{ GeV}/c^2$. The expected 95% C.L. upper limit for the same mass is 12.4. Results for other nineteen Higgs mass hypotheses ranging from $110 \text{ GeV}/c^2$ to $200 \text{ GeV}/c^2$ are also presented.

Acknowledgments

Ringrazio mia mamma e mio papà che negli anni mi hanno sostenuto, incoraggiato e lottato per e con me. Ringrazio mio fratello, che spero mi taglierà gratis i capelli. Ringrazio il mio cane, che non può leggere queste parole perchè non glie l'ho insegnato ma che capisce lo stesso. Ringrazio la nonna ed il nonno per tutti i viaggi e le passeggiate che abbiamo fatto insieme e per le storie che ho sentito e mi piacerebbe scrivere. Ringrazio Marta perchè la amo.

Ringrazio il Dio Bacco senza il quale la mia vita sarebbe stata un po' più noiosa a ringrazio gli amici senza i quali il Dio Bacco sarebbe stato inutile da venerare. Ringrazio la mia moto per non essere nata scooter.

Contents

Sommario	VI
Abstract	VII
Acknowledgments	VIII
1 The Standard Model and The Higgs Mechanism	1
1.1 The Standard Model	1
1.1.1 Electro-Weak Symmetry Group	2
1.1.2 Electro-Weak Interactions	3
1.2 The Higgs Mechanism	5
1.2.1 Non Abelian Spontaneously Broken Symmetry	6
1.2.2 The Higgs Mechanism	7
1.2.3 Masses for the W^\pm and Z^0 Gauge Bosons	8
1.3 Experimental Hunt for The Higgs Boson	8
1.3.1 Higgs Boson Production	8
1.3.2 Higgs Boson Decays	9
1.3.3 Higgs Boson Search Strategies	10
2 Experimental Apparatus	13
2.1 The Tevatron Accelerator Complex	13
2.1.1 The Proton Source	14
2.1.2 The Antiproton Source	14
2.1.3 The Tevatron Ring	15
2.1.4 Luminosity and Tevatron Performance	15
2.2 The CDF II Detector	16
2.2.1 Coordinates System and Standard Definitions at CDF	16
2.3 The Tracking System	18
2.3.1 The Silicon Tracker	19
2.3.2 Central Outer Tracker	20
2.3.3 Track Reconstruction	21
2.3.4 Tracking Algorithm	23
2.3.5 Primary Vertex Reconstruction	23
2.4 Calorimeters	24
2.4.1 The Central Electromagnetic Calorimeter	24
2.4.2 The Plug Calorimeter	26
2.5 Muon Detectors	26

3	The Online Trigger Selection	29
3.1	The CDF Trigger System	29
3.1.1	LEVEL 1	30
3.1.2	LEVEL 2	30
3.1.3	LEVEL 3	31
3.1.4	Trigger Paths	31
3.2	Trigger Paths used in the $H \rightarrow WW$ Analysis	31
4	Physical Object Reconstruction	35
4.1	Lepton Reconstruction and Identification	35
4.1.1	Electron Identification	35
4.1.2	Muon Identification	38
4.1.3	Jet Reconstruction	42
4.2	Hadronic Tau Reconstruction	44
4.3	Missing Energy	45
4.4	Fake Leptons	46
4.5	Trigger Efficiency and Lepton Scale Factor	46
4.5.1	Trigger Efficiency	46
4.5.2	Lepton Scale Factor	47
5	The Trilepton Signature	49
5.1	Motivation	49
5.2	Event Selection	49
5.3	Backgrounds	50
5.4	Background Modeling	50
5.4.1	MET Control Region	51
5.4.2	Z Mass Region	52
5.4.3	Signal Region	53
5.5	Signal - Background Discrimination	54
5.5.1	The Boosted Decision Tree	54
5.6	Systematic Uncertainties	58
5.7	Limit Calculation	59
5.8	Results	60
6	Conclusions	63
	Appendix A BDT Distribution Plots	65
	Appendix B Distribution Plots	71
B.1	MET Control Region	71
B.2	Z -Mass Control Region	77
B.3	Trilepton Signal Region	83
	Bibliography	83

List of Tables

1.1	Weak Isospin and Hypercharge Quantum Numbers of Leptons and Quarks	4
2.1	Accelerator nominal parameters for Run II configuration.	15
2.2	Summary of the main characteristics of the CDF II calorimeter system.	26
2.3	Design parameters of the muon detectors. Assembled from Ref. [9], [3]	27
4.1	Definition of fully identified Tight Central Electron (TCE).	36
4.2	Definition of Forward Electrons (PHX)	37
4.3	Definition of central electron probe.	38
4.4	Definition of central electron fakeable object.	38
4.5	Definition of CMUP central muons.	39
4.6	Definition of CMU central muons. CMU wasn't used till RUN 270012 due to a bug.	40
4.7	Definition of CMP central muons.	40
4.8	Definition of CMX central muons. The exit radius, ρ_{COR} is defined as $\rho_{\text{COR}} = (z_{\text{COR}} - z_0) \cdot \tan \theta$	41
4.9	Definition of CMXMsKs central muons.	41
4.10	Definition of BMU central muons.	42
4.11	Definition of CMIOCES central muons.	42
4.12	Definition of CMIOPES central muons.	43
4.13	Definition of CrkTrk central muons.	43
4.14	Tau reconstruction cut.	46
4.15	Lepton Scale Factors.	48
4.16	Lepton Scale Factors.	48
5.1	Yields for the MET Control Region.	51
5.2	Yields for the Z mass control region.	52
5.3	Yields for the trilepton signal sample.	53
5.4	Ranking of the BDT input variables in the trilepton channel for $m_H = 125, 160, 195 \text{ GeV}/c^2$. The variables are defined in the text.	56
5.5	Systematic uncertainties on the background for the trilepton channel (expressed in %).	59
5.6	Systematic uncertainties on the signals in the trilepton channel (expressed in %).	59
5.7	Observed and expected limits for the trilepton channel.	61

List of Figures

1.1	Leading order Feynman diagrams of the dominant Higgs production mechanisms at hadron colliders: gluon fusion (top left), associated production (top right and bottom left) and vector boson fusion (bottom right).	9
1.2	Cross-sections as a function of the Higgs mass for different Higgs production processes in $p\bar{p}$ collisions at 1.96 TeV (left) and Higgs.	9
1.3	Higgs boson decay branching fractions.	10
2.1	The accelerator system operating at FNAL.	13
2.2	Integrated luminosity as a function of the Run II weeks (2.2a) and Tevatron peak luminosity as a function of the calendar date (2.2b). Empty periods correspond to Tevatron shut-down periods.	17
2.3	Isometric view of the CDF II Detector.	18
2.4	The SVX silicon detector: on the left, a three-dimensional view of the detector allows to see the barrel structure along the beam axes; on the right, the transverse plane section shows in detail the layer sequence.	20
2.5	A 1/6 section of the COT end-plate (2.5a): for each super-layer the total number of cells, the wire orientation (axial or stereo), and the average radius in cm are given. The enlargement shows in detail the slot where the wire planes (sense and field) are installed. Fig. 2.5 represents the cross-section of three axial cells in super-layer 2, the arrow indicates the radial direction.	20
2.6	CDF tracking subdetectors and impact parameter d_0 definition.	22
2.7	One azimuthal electromagnetic calorimeter wedge 2.7a, the elevation view of one quarter of the plug calorimeter 2.7b. In 2.7c elevation view of the CDF detector showing the components of the CDF calorimeter: CEM, CHA, WHA, PEM and PHA.	25
2.8	Muon detectors coverage in the η - ϕ plane.	26
3.1	Functional block diagram of the CDF II trigger and data acquisition systems.	29
4.1	Tau signal cone and isolation annulus for tracks and π^0 's.	44
4.2	Electromagnetic fraction vs. E/P for MC taus and electrons. Entries with $\xi > 0.1$ are in the region below the solid line.	45
5.1	MET Control Region distribution plots.	52
5.2	Z Control Region distribution plots.	53
5.3	Trilepton signal region distribution plots.	54
5.4	Schematic view of a decision tree.	54
5.5	BDT output (left) and background rejection rate versus signal efficiency (right) for three representative Higgs mass hypotheses in the trilepton channel.	57
5.6	Trilepton BDT templates for Higgs masses 125, 160 and 195 GeV/c^2	58

5.7	Observed and expected (median, for the background-only hypothesis) 95% C.L. upper limits on the ratios to the SM cross section, as functions of the Higgs boson mass. The limits are expressed as a multiple of the SM prediction for test masses (every 5 GeV/c^2). The points are joined by straight lines for better readability. The bands indicate the 68% and 95% probability regions where the limits can fluctuate, in the absence of signal.	61
6.1	CDF and $D\bar{O}$ combined limit.	63
A.1	Trilepton BDT templates for Higgs masses 110, 115 and 120 GeV/c^2	65
A.2	Trilepton BDT templates for Higgs masses 125, 130 and 135 GeV/c^2	66
A.3	Trilepton BDT templates for Higgs masses 140, 145 and 150 GeV/c^2	67
A.4	Trilepton BDT templates for Higgs masses 155, 160 and 165 GeV/c^2	68
A.5	Trilepton BDT templates for Higgs masses 170, 175 and 180 GeV/c^2	69
A.6	Trilepton BDT templates for Higgs masses 185, 190 and 195 GeV/c^2	70
A.7	Trilepton BDT template for the Higgs mass 200 GeV/c^2	70
B.1	Data-MC comparison in the trilepton MET control region.	71
B.2	Data-MC comparison in the trilepton MET control region.	72
B.3	Data-MC comparison in the trilepton MET control region.	73
B.4	Data-MC comparison in the trilepton MET control region.	74
B.5	Data-MC comparison in the trilepton MET control region.	75
B.6	Data-MC comparison in the trilepton MET control region.	76
B.7	Data-MC comparison in the trilepton Z -mass control region.	77
B.8	Data-MC comparison in the trilepton Z -mass control region.	78
B.9	Data-MC comparison in the trilepton Z -mass control region.	79
B.10	Data-MC comparison in the trilepton Z -mass control region.	80
B.11	Data-MC comparison in the trilepton Z -mass control region.	81
B.12	Data-MC comparison in the trilepton Z -mass control region.	82
B.13	Data-MC comparison in the trilepton signal region.	83
B.14	Data-MC comparison in the trilepton signal region.	84
B.15	Data-MC comparison in the trilepton signal region.	85
B.16	Data-MC comparison in the trilepton signal region.	86
B.17	Data-MC comparison in the trilepton signal region.	87
B.18	Data-MC comparison in the trilepton signal region.	88

*Si sta,
come d'autunno,
sugli alberi,
le foglie*

[G. UNGARETTI, Soldati]

Introduction

The search for the Standard Model Higgs boson represents one of the main topics of the physics programme at the Tevatron collider. Search strategies are driven by the Higgs production mechanism and the main Higgs decay modes. The Higgs boson production is dominated by the gluon fusion contribution $gg \rightarrow H$. The production in association with a gauge boson, be it a W boson or a Z boson, exhibits cross sections smaller by one order of magnitude. With the increase in integrated luminosity delivered by the Tevatron collider and collected by the CDF detector, the search has also become sensitive to the production via vector boson fusion.

The SM Higgs boson is predicted to decay predominantly into a $b\bar{b}$ final state for values of its mass lower than $135 \text{ GeV}/c^2$, while for higher mass values it decays mostly into a W^+W^- pair, where one of the W 's may be virtual Fig. 1.2. Thanks to a good sensitivity in the high mass regime (the fully leptonic mode of the W^+W^- decay yields a low background final state if compared to the $b\bar{b}$ final state), the Tevatron has reached sensitivity to the Higgs production in the mass range between 156 and $177 \text{ GeV}/c^2$. The search for $H \rightarrow WW$ production with hadronic taus in the final state is complementary to the mainstream dilepton and trilepton searches. The latter are based on selecting events containing electrons and muons and has only a partial acceptance to the final states with taus through the τ leptonic decays, whereas 65% of taus decay semi-hadronically, mostly to charged and neutral pions plus a tau neutrino.

This thesis reports the results of the search for a Standard Model Higgs boson exploiting the experimental signatures with hadronic taus. In particular, we analyze the final state with three leptons including one hadronic tau.

Chapter 1

The Standard Model and The Higgs Mechanism

1.1 The Standard Model

The *Standard Model* (SM) is a theoretical model which describes the elementary constituents of matter and their interactions. Up to now, we discovered four kind of different interactions, the *electromagnetic*, the *gravitational*, the *strong* and the *electro-weak interaction*; excluding gravity, all of them are described by means of a *quantum field gauge theory*.

The Standard Model is the collection of these gauge theories, it is based on the gauge symmetry group $SU(3)_C \times SU(2)_L \times U(1)_Y$ where $SU(3)_C$ is the symmetry group of the *Quantum Chromo-Dynamics* (QCD), the “C” subscript stand for *color charge* which is the conserved charge in the strong interaction. The $SU(2)_L$ is the weak isotopic spin group acting on *left-handed* doublet of fermions while the $U(1)_Y$ group is the *hypercharge* symmetry group of the *right-handed* fermion singlets. Together $SU(2)_L \times U(1)_Y$ form the electro-weak symmetry group.

The Standard Model also contains and (sometimes) predicts the existence of *elementary particles* that interacts between them via the forces mentioned above. The matter constituents are called *fermions*, the interaction are mediated by other particles called *gauge bosons*. Fermions are further categorized into *quark* and *leptons* and are the true fundamental constituents of matter; the gauge bosons arise by means of symmetry property of the Standard Model symmetry group.

The existence of all the leptons, quarks and gauge bosons is confirmed by experimental tests, all but one: the Higgs boson. The Higgs boson is peculiar because, unlike the other bosons, it is not associated with any interaction, instead is postulated as a consequence of the *spontaneously broken symmetry* of the electroweak sector which is the property, responsible of giving mass to all the elementary particles and the weak gauge bosons.

1.1.1 Electro-Weak Symmetry Group

We can now see how to find out the weak interaction symmetry group, to this end, let us start by writing out the *Hamiltonian*

$$H_{weak} = \frac{4G_F}{\sqrt{2}} J_\mu^\dagger J^\mu \quad (1.1.1)$$

where

$$\begin{aligned} J_\mu &\equiv J_\mu^{(+)} = \bar{\psi}_{\nu_e} \gamma_\mu \frac{1}{2} (1 - \gamma_5) \psi_e \equiv \bar{\nu}_{eL} \gamma_\mu e_L \\ J_\mu^\dagger &\equiv J_\mu^{(-)} = \bar{\psi}_e \gamma_\mu \frac{1}{2} (1 - \gamma_5) \psi_{\nu_e} \equiv \bar{e}_L \gamma_\mu \nu_{eL} \end{aligned} \quad (1.1.2)$$

to easy the notation, let us write

$$\chi_L = \begin{pmatrix} \nu_{eL} \\ e_L^- \end{pmatrix} \equiv \begin{pmatrix} \nu_e \\ e^- \end{pmatrix} \quad (1.1.3)$$

and using the Pauli matrices

$$\tau_\pm = \frac{1}{2} (\tau_1 \pm i\tau_2) \quad (1.1.4)$$

we have

$$\begin{aligned} J_\mu^{(+)} &= \bar{\chi}_L \gamma_\mu \tau_+ \chi_L \\ J_\mu^{(-)} &= \bar{\chi}_L \gamma_\mu \tau_- \chi_L \end{aligned} \quad (1.1.5)$$

by introducing a “neutral” current

$$J_\mu^{(3)} = \bar{\chi}_L \gamma_\mu \frac{\tau_3}{2} \chi_L = \frac{1}{2} \bar{\nu}_L \gamma_\mu \nu_L - \frac{1}{2} \bar{e}_L \gamma_\mu e_L \quad (1.1.6)$$

we have a “triplet” of currents

$$J_\mu^i = \bar{\chi}_L \gamma_\mu \frac{\tau_i}{2} \chi_L. \quad (1.1.7)$$

Now if we pick up an $SU(2)_L$ transformation

$$\chi_L(x) \rightarrow \chi'_L(x) = e^{i\vec{\varepsilon} \cdot \vec{T}} \chi_L(x) = e^{i\vec{\varepsilon} \cdot \frac{\vec{\tau}}{2}} \chi_L(x), \quad (1.1.8)$$

where $T_i = \tau_i/2$ are the $SU(2)_L$ generators, and think the χ_L as the *fundamental representation*, then the current triplet is a triplet of $SU(2)_L$, the *weak isotopic spin*.

The right handed fermions are singlet for the $SU(2)_L$, thus

$$e_R \rightarrow e'_R = e_R. \quad (1.1.9)$$

Since we are considering the global transformations, we have no interaction, so the Lagrangian reads

$$\mathcal{L} = \bar{e}_i \gamma^\mu \partial_\mu e + \bar{\nu}_i \gamma^\mu \partial_\mu \nu \equiv \bar{\chi}_L i \gamma \partial \chi_L + \bar{e}_R i \gamma \partial e_R; \quad (1.1.10)$$

for now we are bounded to set $m_e = 0$, in fact the mass term couples right and left fermion’s components and it is not $SU(2)_L$ invariant. In 1973, experiments detected events of the type

$$\bar{\nu}_\mu e^- \rightarrow \bar{\nu}_\mu e^- \quad (1.1.11)$$

$$\begin{cases} \nu_\mu N \rightarrow \nu_\mu X \\ \bar{\nu}_\mu N \rightarrow \bar{\nu}_\mu X \end{cases} \quad (1.1.12)$$

which are evidence of a neutral current. Further investigations yielded that the neutral weak current is predominantly $V - A$ (i.e. left-handed) but not purely $V - A$ so the $J_\mu^{(3)}(x)$ current introduced above can not be used as it involves only left handed fermions. We know a neutral current that mixes left and right components namely the electromagnetic current

$$J_\mu \equiv eJ_\mu^{(em)} = e\bar{\psi}\gamma_\mu Q\psi \quad (1.1.13)$$

where Q is the charge operator with eigenvalue $Q = -1$ for the electron. Q is the generator of the $U(1)_{(em)}$ group. So we have an isospin triplet and we have included the right hand components, the isospin singlet, what we want to do, is to combine them and define the hypercharge operator

$$Y = 2(Q - T_3) \rightarrow Q = T_3 + \frac{Y}{2}, \quad (1.1.14)$$

for the current we have

$$J_\mu^{(em)} = J_\mu^{(3)} + \frac{1}{2}J_\mu^Y \quad (1.1.15)$$

where

$$J_\mu^Y = \bar{\psi}\gamma_\mu Y\psi \quad (1.1.16)$$

so, by analogy, the hypercharge Y generates a $U(1)_Y$ symmetry, and, as it is a $SU(2)_L$ singlet, leaves (1.1.10) invariant under the transformations

$$\begin{aligned} \chi_L(x) &\rightarrow \chi'_L(x) = e^{i\beta Y} \chi_L(x) \equiv e^{i\beta y_L} \chi_L \\ e_R(x) &\rightarrow e'_R(x) = e^{i\beta Y} e_R(x) \equiv e^{i\beta y_R} e_R. \end{aligned} \quad (1.1.17)$$

We thus have incorporated the electromagnetic interactions extending the group to $SU(2)_L \times U(1)_Y$ and instead of having a single symmetry group we have a direct product of groups, each with his own *coupling constant*, so, in addition to e we will have another coupling to be found. Since we have a direct product of symmetry groups, the generators of $SU(2)_L$, T_i , and the generators of $U(1)_Y$, Y commute, the commutation relations are

$$[T_+, T_-] = 2T_3 \quad ; \quad [T_3, T_\pm] = \pm T_\pm \quad ; \quad [Y, T_\pm] = [Y, T_3] = 0, \quad (1.1.18)$$

member of the same isospin triplet, have same hypercharge eigenvalue; the relevant quantum numbers are summarized in the table 1.1.

1.1.2 Electro-Weak Interactions

As stated before, interactions are mediated by a gauge boson, we now want to find out those for the electroweak interaction, to this end let us consider *local* gauge transformations

$$\begin{aligned} \chi_L &\rightarrow \chi'_L = e^{i\vec{\epsilon}(x)\cdot\vec{T} + i\beta(x)Y} \chi_L \\ \psi_R &\rightarrow \psi'_R = e^{i\beta(x)Y} \psi_R, \end{aligned} \quad (1.1.19)$$

Lepton	T	$T^{(3)}$	Q	Y	Quark	T	$T^{(3)}$	Q	Y
ν_e	$\frac{1}{2}$	$\frac{1}{2}$	0	-1	u_L	$\frac{1}{2}$	$\frac{1}{2}$	$\frac{2}{3}$	$\frac{1}{3}$
e_L^-	$\frac{1}{2}$	$-\frac{1}{2}$	-1	-1	d_L	$\frac{1}{2}$	$-\frac{1}{2}$	$-\frac{1}{2}$	$\frac{1}{3}$
e_R^+	0	0	-1	-2	u_R	0	0	$\frac{2}{3}$	$\frac{4}{3}$
					d_R	0	0	$-\frac{1}{3}$	$-\frac{2}{3}$

Table 1.1: Weak Isospin and Hypercharge Quantum Numbers of Leptons and Quarks

introducing four gauge bosons, $W_\mu^{(1)}, W_\mu^{(2)}, W_\mu^{(3)}, B_\mu$ (same as the number of generators) and the *covariant derivative*

$$\begin{aligned}
 D_\mu \chi_L &= (\partial_\mu + ig \frac{\vec{\tau}}{2} \cdot \vec{W}_\mu(x) + i \frac{g'}{2} y_L B_\mu(x)) \chi_L \\
 &= (\partial_\mu + ig \frac{\vec{\tau}}{2} \cdot \vec{W}_\mu(x) - i \frac{g'}{2} B_\mu(x)) \chi_L \\
 D_\mu \psi_R &= (\partial_\mu + i \frac{g'}{2} y_R B_\mu(x)) \psi_R \\
 &= (\partial_\mu - i \frac{g'}{2} B_\mu(x)) e_R
 \end{aligned} \tag{1.1.20}$$

the Lagrangian (1.1.10) reads

$$\begin{aligned}
 \mathcal{L} &= \bar{\chi}_L i \gamma \partial \chi_L + \bar{e}_R i \gamma \partial e_R - g \bar{\chi}_L \gamma^\mu \frac{\vec{\tau}}{2} \chi_L \vec{W}_\mu + \frac{g'}{2} (\bar{\chi}_L \gamma^\mu \chi_L + 2 \bar{e}_R \gamma^\mu e_R) B_\mu \\
 &\quad - \frac{1}{4} \vec{W}_{\mu\nu} \vec{W}^{\mu\nu} - \frac{1}{4} B_{\mu\nu} B^{\mu\nu}
 \end{aligned} \tag{1.1.21}$$

where

$$\begin{aligned}
 \vec{W}_{\mu\nu} &= \partial_\mu \vec{W}_\nu - \partial_\nu \vec{W}_\mu - g \vec{W}_\mu \times \vec{W}_\nu \\
 B_{\mu\nu} &= \partial_\mu B_\nu - \partial_\nu B_\mu
 \end{aligned} \tag{1.1.22}$$

are the kinetic plus non abelian interaction term for the $SU(2)_L$ symmetry (first equation) and the kinetic term for the abelian symmetry group $U(1)_Y$. We can now split the Lagrangian terms to find out the field of the vector bosons coupled to the charged current and to the neutral current.

Charged Currents Interaction Let us consider the term

$$\mathcal{L}_{int}^{ew} = -g \bar{\chi}_L \gamma_\mu \frac{\vec{\tau}}{2} \chi_L \vec{W}_\mu + \frac{g'}{2} \bar{\chi}_L \gamma_\mu \chi_L B^\mu + g' \bar{e}_R \gamma_\mu e_R B^\mu \tag{1.1.23}$$

defining

$$W_\mu^\pm = \frac{1}{\sqrt{2}} W^{(1)} \mp i W^{(2)} \tag{1.1.24}$$

we can write

$$\mathcal{L}^{CC} = -\frac{g}{\sqrt{2}} (J_\mu^{(+)} W^{-\mu} + J_\mu^{(-)} W^{+\mu}) \tag{1.1.25}$$

and recognize two charged vector bosons with coupling given by “ g ”.

Neutral Current Interaction The relevant term left to consider for what concerns the electroweak currents is

$$\mathcal{L}^{NC} = -gJ_\mu^{(3)}W^{(3)\mu} - \frac{g'}{2}J_\mu^Y B^\mu, \quad (1.1.26)$$

the electromagnetic interaction, $-ieJ^{(em)\mu}A_\mu$, is embedded in this expression as will become clear considering the *spontaneously broken symmetry* phenomena, for now, is sufficient to define

$$\begin{aligned} W_\mu^{(3)} &= \cos\theta_w Z_\mu + \sin\theta_w A_\mu \\ B_\mu &= -\sin\theta_w Z_\mu + \cos\theta_w A_\mu \end{aligned} \quad (1.1.27)$$

and invert to get

$$\begin{aligned} A_\mu &= \sin\theta_w W_\mu^{(3)} + \cos\theta_w B_\mu \\ Z_\mu &= \cos\theta_w W_\mu^{(3)} - \sin\theta_w B_\mu \end{aligned} \quad (1.1.28)$$

where θ_w is the electroweak *mixing angle*. Plugging this into (1.1.26) and rearranging terms

$$\begin{aligned} \mathcal{L}^{NC} &= -\left[(g \sin\theta_w J_\mu^{(3)} + \frac{g'}{2} \cos\theta_w J_\mu^Y)A^\mu\right. \\ &\quad \left.+ (g \cos\theta_w J_\mu^{(3)} - \frac{g'}{2} \sin\theta_w J_\mu^Y)Z^\mu\right] \end{aligned} \quad (1.1.29)$$

since A^μ is the photon field, the first parenthesis must be identified with the electromagnetic current, thus

$$-(g \sin\theta_w J_\mu^{(3)} + \frac{g'}{2} \cos\theta_w J_\mu^Y)A^\mu = -eJ_\mu^{(em)}A^\mu \equiv -e\left(J_\mu^{(3)} + \frac{J_\mu^Y}{2}\right)A^\mu \quad (1.1.30)$$

from which we get the relation

$$g \sin\theta_w = g' \cos\theta_w = e \quad (1.1.31)$$

and so we can rewrite (1.1.26),

$$\mathcal{L}^{NC} = -\frac{g}{\cos\theta_w}[J_\mu^{(3)} - \sin^2\theta_w J_\mu^{(em)}]Z^\mu \quad (1.1.32)$$

so that Z^μ can be identified with the field for the neutral vector boson.

1.2 The Higgs Mechanism

Up to now, we have massless gauge vector bosons, in fact no term such as $M^2 B_\mu B^\mu/2$ appear in the Lagrangian (1.1.21), but this kind of terms are not gauge invariant and thus we can not just add them or we will end up with troubles later when trying to renormalize the theory.

A gauge invariant way to recover the fermions and bosons masses, is to spontaneously brake the local $SU(2)_L \times U(1)_Y$ electroweak symmetry.

1.2.1 Non Abelian Spontaneously Broken Symmetry

Let us consider a local symmetry breaking and refer to [10] for a more complete explanation. Be ϕ a complex scalar field,

$$\mathcal{L} = (\partial_\mu \phi^*)(\partial_\mu \phi) - \underbrace{\mu^2 \phi^* \phi - \lambda(\phi^* \phi)^2}_{V(\phi^* \phi)} \quad (1.2.1)$$

setting

$$\begin{aligned} \phi &= \frac{\phi_1 + i\phi_2}{\sqrt{2}} \\ \phi^* &= \frac{\phi_1 - i\phi_2}{\sqrt{2}} \end{aligned} \quad (1.2.2)$$

we get

$$\mathcal{L} = \frac{1}{2}(\partial_\mu \phi_1)^2 + \frac{1}{2}(\partial_\mu \phi_2)^2 - \frac{\mu^2}{2}(\phi_1^2 + \phi_2^2) - \frac{\lambda}{4}(\phi_1^2 + \phi_2^2)^2 \quad (1.2.3)$$

the gauge transformations are

$$\begin{cases} \phi(x) \rightarrow \phi'(x) = e^{i\epsilon} \phi(x) \\ \phi^\dagger(x) \rightarrow \phi^{\dagger'}(x) = e^{-i\epsilon} \phi^\dagger(x). \end{cases} \quad (1.2.4)$$

There are two possible choices for the potential

- $\mu^2 > 0$, which gives a stable configuration around $|\phi| = 0$.
- $\mu^2 < 0$, which gives a circle of minima such that $\phi_1^2 + \phi_2^2 = v^2$, with $v^2 = -\mu^2/\lambda$.
This minima are not gauge invariant, in fact

$$\phi_0 = \langle 0|\phi|0\rangle \rightarrow \frac{v}{\sqrt{2}} e^{i\alpha} \quad \text{if} \quad \phi \rightarrow e^{i\alpha} \phi \quad (1.2.5)$$

To get the particle interaction we make a perturbative expansion around one minimum, we chose one, for example $\alpha = 0$, for which $\phi_1 = v$ and $\phi_2 = 0$ and introduce the two perturbations $\eta(x)$ and $\xi(x)$ so that

$$\phi(x) = \frac{1}{\sqrt{2}} \overbrace{v + \xi(x)}^{\phi_1} + i \overbrace{\eta(x)}^{\phi_2} \quad (1.2.6)$$

and plug them in the Lagrangian (1.2.3) to obtain

$$\begin{aligned} \mathcal{L}'(\xi, \eta) &= \frac{1}{2}(\partial_\mu \xi)^2 + \frac{1}{2}(\partial_\mu \eta)^2 - \frac{1}{2}(-2\mu^2)\eta^2 \\ &\quad - \lambda v(\eta^2 + \xi^2)\eta - \frac{1}{4}(\eta^2 + \xi^2)^4 + \dots \end{aligned} \quad (1.2.7)$$

as we can see, the third term looks like a mass term so that the field η has mass $m_\eta^2 = -2\mu^2$ while we have no mass term for the field ξ .

This “trick” to give mass to one of the gauge field, is the *braking of the symmetry*. In fact, by choosing one particular vacuum among the infinite ones, we lost our gauge invariance; moreover, we ended up with a scalar gauge boson, known as *Goldstone boson*. We need to find a way to recover the masses of the gauge bosons in a gauge invariant way by getting rid of massless scalar fields; the solution is the topic of the very next section. next section.

1.2.2 The Higgs Mechanism

Consider now a local gauge $SU(2)$ symmetry, the field transformations are

$$\phi(x) \rightarrow \phi'(x) = e^{i\sum_{k=1}^3 \epsilon^k T^k} \phi(x), \quad (1.2.8)$$

where $T^k = \frac{\tau^k}{2}$ and $[T^i, T^j] = i\epsilon^{ijk} T^k$ with $i, j, k = 1, 2, 3$. To achieve invariance for the Lagrangian

$$\mathcal{L} = (\partial_\mu \phi)^\dagger (\partial^\mu \phi) - \mu^2 \phi^\dagger \phi - \lambda (\phi^\dagger \phi)^2, \quad (1.2.9)$$

where

$$\phi \equiv \begin{pmatrix} \phi_i \\ \phi_j \end{pmatrix} = \frac{1}{\sqrt{2}} \begin{pmatrix} \phi_1 + i\phi_2 \\ \phi_3 + i\phi_4 \end{pmatrix}, \quad (1.2.10)$$

we need to introduce the covariant derivative

$$D_\mu = \partial_\mu + ig \frac{\vec{\tau}}{2} \cdot \vec{W}_\mu(x). \quad (1.2.11)$$

In the case of infinitesimal transformations, the fields transform like

$$\phi(x) \rightarrow \phi'(x) \simeq (1 + i\vec{\epsilon}(x) \cdot \frac{\vec{\tau}}{2}) \phi(x) \quad (1.2.12)$$

while the gauge bosons transformations are

$$\vec{W}_\mu(x) \rightarrow \vec{W}_\mu(x) - \frac{1}{g} \partial_\mu \vec{\epsilon}(x) - \vec{\epsilon}(x) \times \vec{W}_\mu(x). \quad (1.2.13)$$

Replacing everything in the Lagrangian we obtain

$$\mathcal{L} = (\partial_\mu \phi + ig \frac{\vec{\tau}}{2} \cdot \vec{W}_\mu \phi)^\dagger (\partial_\mu \phi + ig \frac{\vec{\tau}}{2} \cdot \vec{W}_\mu \phi) - V(\phi) - \frac{1}{4} \vec{W}_{\mu\nu} \cdot \vec{W}^{\mu\nu}, \quad (1.2.14)$$

where the potential is given by

$$V(\phi) = \mu^2 \phi^\dagger \phi + \lambda (\phi^\dagger \phi)^2 \quad (1.2.15)$$

and the kinetic term is

$$\vec{W}_{\mu\nu} = \partial_\mu \vec{W}_\nu - \partial_\nu \vec{W}_\mu - g \vec{W}_\mu \times \vec{W}_\nu. \quad (1.2.16)$$

We are interested in the case of the spontaneously broken symmetry, thus $\mu^2 < 0$ and $\lambda > 0$. The minima of the potential lie on

$$\phi^\dagger \phi = \frac{1}{2} (\phi_1^2 + \phi_2^2 + \phi_3^2 + \phi_4^2) = -\frac{\mu^2}{2\lambda} \quad (1.2.17)$$

and we have to choose one of them, let it be

$$\phi_1 = \phi_2 = \phi_4 = 0, \quad \phi_3^2 = -\frac{\mu^2}{\lambda} \equiv v^2. \quad (1.2.18)$$

To expand ϕ around this particular vacuum

$$\phi_0 \equiv \frac{1}{\sqrt{2}} \begin{pmatrix} 0 \\ v \end{pmatrix} \quad (1.2.19)$$

it is sufficient to substitute the expansion

$$\phi(x) = \frac{1}{\sqrt{2}} \begin{pmatrix} 0 \\ v + h(x) \end{pmatrix} \quad (1.2.20)$$

in the Lagrangian (1.2.14) in order to get rid of the, unobserved, Goldstone bosons and retain only one neutral scalar field, the *Higgs field*.

1.2.3 Masses for the W^\pm and Z^0 Gauge Bosons

The gauge bosons masses are generated simply substituting the vacuum expectation value, ϕ_0 , in the Lagrangian, the relevant term is

$$\begin{aligned}
 \left| \left(g \frac{\vec{\tau}}{2} \cdot \vec{W}_\mu + \frac{g'}{2} B_\mu \right) \phi \right|^2 &= \\
 &= \frac{1}{8} \left| \begin{pmatrix} gW_\mu^3 + g'B_\mu & g(W_\mu^1 - iW_\mu^2) \\ g(W_\mu^1 + iW_\mu^2) & -gW_\mu^3 + g'B_\mu \end{pmatrix} \begin{pmatrix} 0 \\ v \end{pmatrix} \right|^2 \\
 &= \frac{1}{8} v^2 g^2 [(W_\mu^1)^2 + (W_\mu^2)^2] + \frac{1}{8} v^2 (g'B_\mu - gW_\mu^3)(g'B_\mu - gW_\mu^3) \\
 &= \left(\frac{1}{2} gv \right)^2 W_\mu^+ W_\mu^- + \frac{1}{8} v^2 \begin{pmatrix} W_\mu^3 & B_\mu \end{pmatrix} \begin{pmatrix} g^2 & -gg' \\ -gg' & g^2 \end{pmatrix} \begin{pmatrix} W_\mu^3 \\ B_\mu \end{pmatrix}
 \end{aligned} \tag{1.2.21}$$

having used $W^\pm = (W^1 \mp iW^2)/\sqrt{2}$. The mass term, lead us to conclude that

$$M_W = \frac{1}{2} gv. \tag{1.2.22}$$

The remaining term is off diagonal

$$\begin{aligned}
 \frac{1}{8} v^2 [g^2 (W_\mu^3)^2 - 2gg'W_\mu^3 B_\mu + g'^2 B_\mu^2] &= \frac{1}{8} v^2 [gW_\mu^3 - gB_\mu]^2 \\
 &+ 0 \quad [g'W_\mu^3 - g'B_\mu]^2
 \end{aligned} \tag{1.2.23}$$

but one can diagonalize and find that

$$\begin{aligned}
 A^\mu &= \frac{g'W_\mu^3 + gB_\mu}{\sqrt{g^2 + g'^2}} \\
 Z^\mu &= \frac{gW_\mu^3 - g'B_\mu}{\sqrt{g^2 + g'^2}}
 \end{aligned} \tag{1.2.24}$$

with $M_A = 0$ and $M_Z = v\sqrt{g^2 + g'^2}/2$ which are the photon and neutral weak vector boson fields. Thus the mass eigenstates are a massless vector boson, A_μ and a massive gauge boson Z_μ .

We have shown in this section how the Higgs mechanism can be applied to give mass to the gauge bosons of the electroweak model.

1.3 Experimental Hunt for The Higgs Boson

The Higgs boson mass m_H represents the only unknown parameter of the Standard Model. Given m_H , the production modes and corresponding cross sections of the Higgs boson, as well as its lifetime and decay branching ratios, can be predicted.

1.3.1 Higgs Boson Production

At hadron colliders the main production modes for a Standard Model Higgs boson are the *gluon fusion*, *vector boson fusion* and *associated production* to a Z or a W weak gauge boson. Fig. 1.1 shows the leading order Feynman diagrams for the aforementioned production processes.

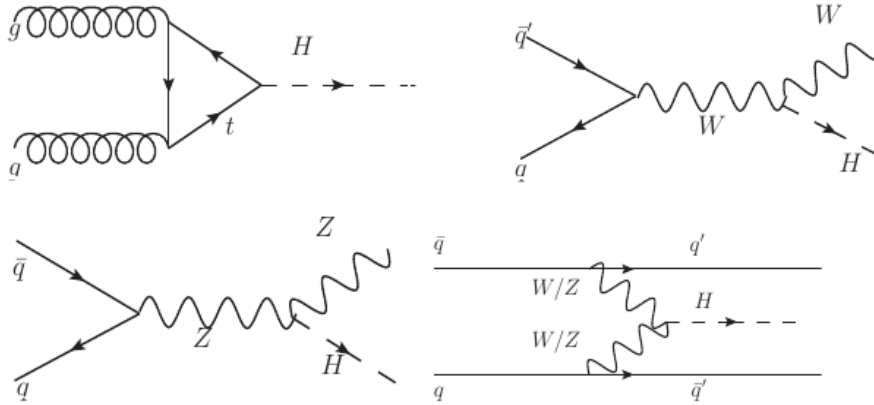


Figure 1.1: Leading order Feynman diagrams of the dominant Higgs production mechanisms at hadron colliders: gluon fusion (top left), associated production (top right and bottom left) and vector boson fusion (bottom right).

Fig. 1.2 shows the expected production cross section at the Tevatron for the four processes. As one can see, the gluon fusion contributes the most having a cross section of 0.1 - 1 pb in the mass range $100 < m_H < 200 \text{ GeV}/c^2$ and thus contributing for the 78% to the inclusive Higgs production cross section. The associated production ranges from 0.3 to 0.01 pb , together they contribute for the 15% of the total cross section. Vector boson fusion only contributes for the 7%.

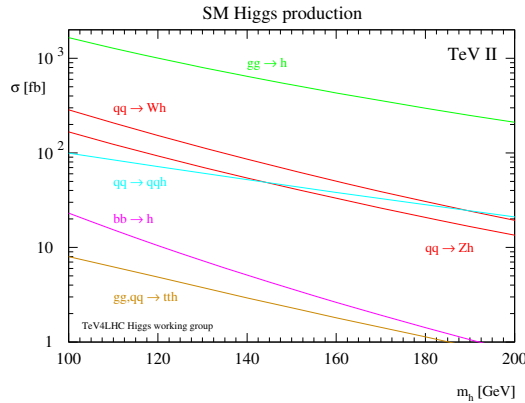


Figure 1.2: Cross-sections as a function of the Higgs mass for different Higgs production processes in $p\bar{p}$ collisions at 1.96 TeV (left) and Higgs.

1.3.2 Higgs Boson Decays

Higgs boson search through the process $gg \rightarrow H \rightarrow b\bar{b}$ suffers of large background from non-resonant $b\bar{b}$ production that has the cross section several orders of magnitude larger. Tevatron $H \rightarrow b\bar{b}$ searches exploit the associated production of the Higgs boson, with the W or Z bosons leptonic decays, to increase the expected signal to background ratio. However, for the rapid decrease of the $H \rightarrow b\bar{b}$ branching ratio and for the small cross section of the associated production, these searches are not

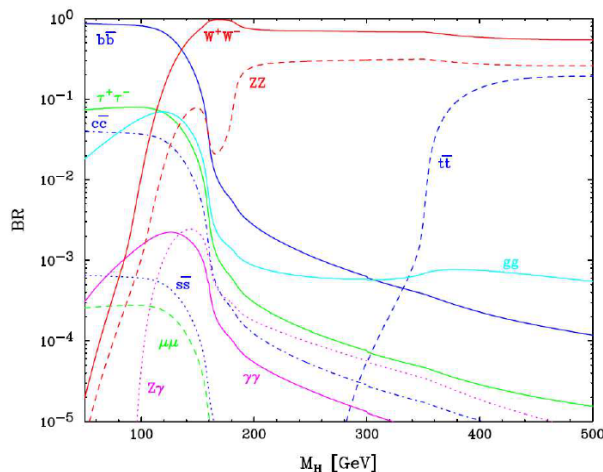


Figure 1.3: Higgs boson decay branching fractions.

powerful for $m_H > 120 \text{ GeV}/c^2$. Fig. 1.3 shows that for $m_H = 135 \text{ GeV}/c^2$ the number of events obtained by associated production with $H \rightarrow b\bar{b}$ are four times less than $m_H = 100 \text{ GeV}/c^2$.

$H \rightarrow \gamma\gamma$ at Tevatron suffers the low number of expected events and detectors not designed for having good photon reconstruction. The results in this decay channel are not competitive with $H \rightarrow b\bar{b}$ searches. Higgs searches for mass up to $140 \text{ GeV}/c^2$, exploiting either the $b\bar{b}$ or $\gamma\gamma$ decay channels, are commonly referred to *Low Mass Higgs* searches.

If the Higgs mass $m_H > 120 \text{ GeV}/c^2$ the number of expected $H \rightarrow WW$ events is larger than that expected for $H \rightarrow b\bar{b}$ by associated production. Higgs searches exploiting di-boson Higgs decay channels are commonly referred as *High Mass Higgs* searches. The main background contributor to these processes is the non-resonant WW and ZZ production.

1.3.3 Higgs Boson Search Strategies

The best decay channels to search for a Higgs boson with mass $m_H > 120 \text{ GeV}/c^2$ are the WW and ZZ . The expected backgrounds are very different for different decay channels thus the analysis strategy strongly depends on the decay modes of the gauge bosons. The *HWW* group focuses on the W gauge boson, it can decay hadronically, 68% of the times or leptonically.

Hadronic WW Decays Final states involving only hadronic jets suffer a large background due to multi-jet production which has a cross section larger that signal by several orders of magnitude. When one of the two W bosons decays to leptons and the other one to hadrons, we have a final state with one high- p_T lepton (ℓ), two jets (j) and energy imbalance in the detector for the undetected neutrino: $\ell jj + \cancel{E}_T$. The latter quantity is referred to as missing transverse energy (\cancel{E}_T): since we expect the transverse energy to be almost zero before the collision any imbalance in the measured energy of the decay products in the transverse plane can indicate undetected particles.

Leptonic WW Decays The leptonic decay channel offers the best signal/background ratio. Direct production of the Higgs boson has no jets in the final state at Leading Order, the signature of such process is then two opposite charged high- p_T leptons, \cancel{E}_T coming from the two neutrinos and low jet activity in the detector. Associated production of the Higgs boson with a W or Z boson, is likely to have jets in the final state that come from the hadronic decay of the gauge boson. In this case the signature will be two opposite charged leptons, missing transverse energy coming from the leptonic decays of the W bosons, and the presence of additional jets in the detector. The vector boson fusion Higgs production process, naturally has two jets in the final state. In addition to the non-resonant WW production, we can also expect significant background contribution from $t\bar{t}$ pairs in the sample. In fact it has the same final state as the signal when each top decays $t \rightarrow Wb \rightarrow \ell\nu b$, with two b-jets in the final state.

Chapter 2

Experimental Apparatus

2.1 The Tevatron Accelerator Complex

The Tevatron, is a proton-antiproton accelerator located at the “Fermi National Accelerator Laboratory” (FNAL) and producing $p\bar{p}$ collisions at a center-of-mass energy of $\sqrt{s} = 1.96 \text{ TeV}$. Proton and antiprotons collide at two interaction points, where the “Collider Detector at Fermilab” (CDF) and $D\bar{O}$ detectors are installed. The Tevatron proton and antiproton beams are the result of a complex apparatus, which involves proton and antiproton production, antiproton storage, an intermediate acceleration chain up to the injection into the Tevatron ring. The tevatron acceleration complex is shown in Fig. 2.1.

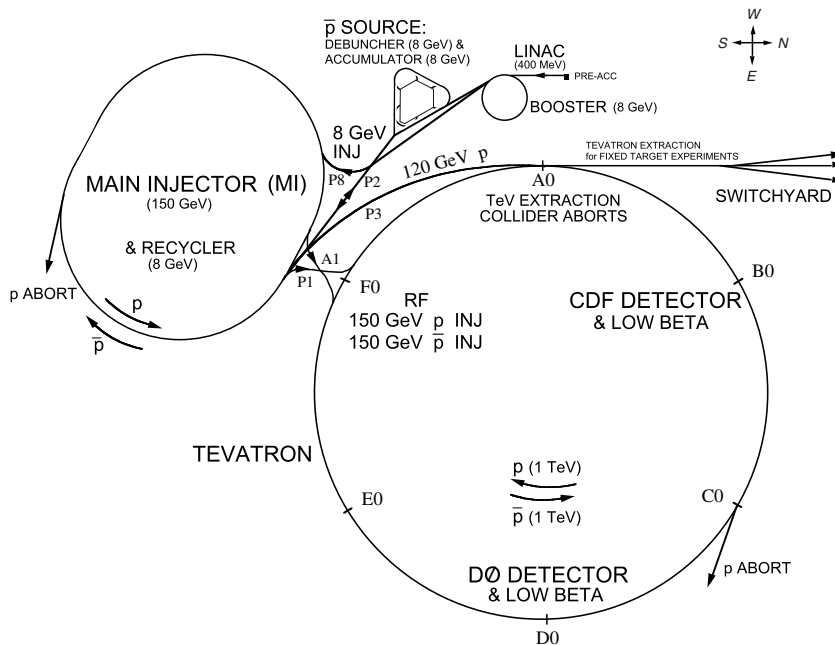


Figure 2.1: The accelerator system operating at FNAL.

2.1.1 The Proton Source

The acceleration cycle of the proton beam begins with the production of negatively ionized hydrogen atoms, H^- , which are initially accelerated to a kinetic energy of 750 KeV by a Cockroft-Walton electrostatic accelerator. Preaccelerated H^- ions are then injected into the LINAC, where they reach an energy of 400 MeV by traveling through a 150 m long chain of radio-frequency (RF) accelerating cavities. Prior to being injected into the *Booster*, the H^- ions pass through a carbon foil which strips their electrons off. In the booster the protons are accelerated to 8 GeV by a number of RF cavities and then they are transferred to another synchrotron, called *Main Injector*¹, which brings their energy up to 150 GeV . This is the final step before protons are injected into the Tevatron.

2.1.2 The Antiproton Source

The production of the antiproton beam is significantly more complicated. The cycle starts with the extraction from the *Main Injector* of a 120 GeV proton beam, which is directed onto a Nickel alloy target. The collisions creates a variety of different particles, among which are \bar{p} , that are produced with an efficiency of about $18\bar{p}/10^6 p$ through the following reaction:

$$p + \binom{p}{n} \rightarrow p + p + \binom{p}{n} + \bar{p}. \quad (2.1.1)$$

The particles, coming off the target at different angles, are focused into a beam line by means of a magnetic lithium collection lens. In order to select only the antiprotons, the beam is sent through a pulsed magnet which acts as a charge-mass spectrometer. The emerging antiprotons, which have a bunch structure similar to that of the incident protons and a large momentum spread, are stored in the *Debuncher*, a storage ring where the \bar{p} momentum spread is reduced via stochastic cooling² [15].

At the end of the debunching process, the bunch structure is destroyed resulting in a continuous beam of 8 GeV antiprotons which are successively transferred to the *Accumulator*. The accumulator is a triangle-shaped storage ring, housed in the same tunnel as the debuncher, where the antiprotons are further cooled down and stored until all the debuncher cycles are completed. When the collected antiprotons saturate the accumulator acceptance ($\sim 6 \times 10^{11}$ antiprotons), they are transferred to the *Recycler*³, a 8 GeV fixed energy storage ring with a larger acceptance, made of permanent magnets and placed in the main injector enclosure. In the recycler the size and spread of the antiproton beam is further shrunk by the electron cooling process: in one of

¹Completed in 1999 for Run II, it is located in a 3 km circumference tunnel, which houses also the antiproton *Recycler* and is approximately tangent to the Tevatron.

²Stochastic cooling is a technique used to reduce the transverse momentum and energy spread of a particle beam without any accompanying beam-loss. This is achieved by applying iteratively a feedback mechanism that senses the beam deviation from the ideal orbit with a set of electrostatic plates, processes and amplifies the signal, and transmits an adequately-sized synchronized correction pulse to another set of plates downstream.

³Antiproton availability is the most limiting factor at the Tevatron for attaining high luminosities: keeping a large antiproton beam inside the recycler has been one of the most significant engineering challenges and the excellent performance of the recycler is an achievement of prime importance for the good operation of the accelerator.

the sections of the recycler a beam of electrons travels close to the antiprotons at the same velocity, absorbing energy from the antiprotons. When a current sufficient to create 36 bunches with the required density is available, the \bar{p} are injected into the main injector where they are accelerated to 150 GeV .

2.1.3 The Tevatron Ring

The Tevatron is a 1 km -radius superconducting synchrotron, that accelerates particles from 150 GeV to 980 GeV . The proton and antiproton beams circulate in opposite directions in the same beam pipe. Electrostatic separators produce a strong electric field that keeps the two beams away from each other except at the collision points. The beam is steered by 774 super-conducting dipole magnets and focused by 240 quadrupole magnets with a maximum magnetic field of 4.2 Tesla. A cryogenic system based on liquid helium and nitrogen cools down the Tevatron magnets to 4.2 K, at which temperature the niobium-titanium alloy of the magnet coils becomes superconducting. The process of injecting particles into the machine, accelerating them, and initiating collisions is referred to as a “shot”. It starts with the injection from the main injector of 150 GeV protons, two bunches at a time. Once the proton beam is in the machine, groups of four antiproton bunches are mined from the recycler, accelerated to 150 GeV in the main injector and injected into the Tevatron. The RF cavities accelerate the beams to 980 GeV , and then some electrostatic separators switch polarity to cause the beams to collide at two points. Each interaction point lies at the center of a particle detector: DØ named after its location in the Tevatron optics, and CDF located at BØ. Successively, beams are scraped with remotely-operated collimators to remove the beam halo and, as soon as the beam conditions are stable, the experiments begin to take data. A continuous period of collider operation with the same protons and antiproton beams is called a “store”.

Parameter	Run II value
number of bunches (N_b)	36
revolution frequency [MHz] (f_{bc})	1.7
bunch rms [m] σ_l	0.37
bunch spacing [ns]	396
protons/bunch (N_p)	2.7×10^{11}
antiprotons/bunch ($N_{\bar{p}}$)	3.0×10^{10}
total antiprotons	1.1×10^{12}
β^* [cm]	35

Table 2.1: Accelerator nominal parameters for Run II configuration.

2.1.4 Luminosity and Tevatron Performance

The performance of a collider is evaluated in terms of two key parameters: the available center-of-mass energy, \sqrt{s} , and the instantaneous luminosity, \mathcal{L} . The former defines the accessible phase-space for the production of final state particles. The latter is defined as the interaction rate per unit cross section of the colliding beams (collisions/(cm^2s)). In the absence of a crossing angle or position offset, the luminosity

at CDF or DØ is given by the expression:

$$\mathcal{L} = \frac{f_{bc} N_b N_p N_{\bar{p}}}{2\pi(\sigma_p^2 + \sigma_{\bar{p}}^2)} F\left(\frac{\sigma_l}{\beta^*}\right), \quad (2.1.2)$$

where f_{bc} is the revolution frequency, N_b is the number of bunches, $N_{p(\bar{p})}$ is the number of protons (antiprotons) per bunch, and $\sigma_{p(\bar{p})}$ is the transverse proton (antiproton) beam size at the interaction point. F is a form factor with a complicated dependence on the beta function value at the interaction point ⁴, β^* , and the bunch length, σ_l . Tab. 2.1 shows the design Run II accelerator parameters while Fig. 2.2 shows the evolution of the integrated luminosity, defined as $L = \int \mathcal{L} dt$, and the instantaneous luminosity at the start of Tevatron stores during the Run II. The steady increase of the integrated luminosity and the continuous improvement of the instantaneous luminosity prove the outstanding performance of the accelerator. The Tevatron program was terminated on September 30, 2011. During the Run II the Tevatron delivered $12 fb^{-1}$ of data per experiment, ~ 10 of which were collected by the CDF and DØ detectors.

2.2 The CDF II Detector

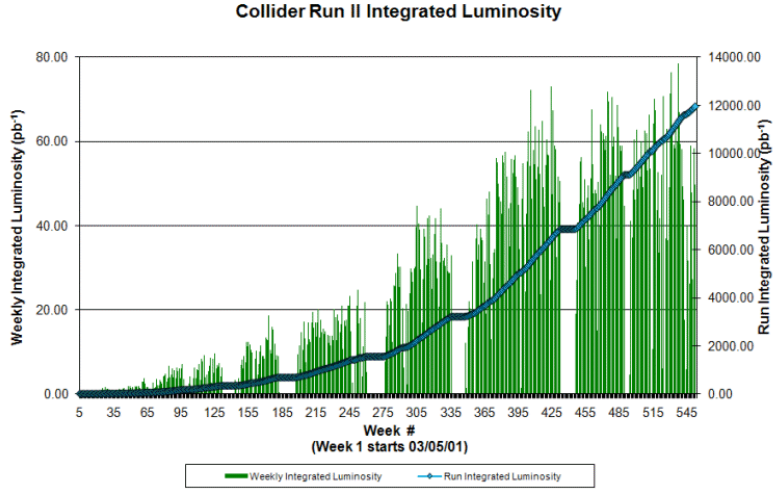
The CDF II detector, in operation from 2001 to 2011, is an azimuthally and forward-backward symmetric apparatus designed to study the $p\bar{p}$ collisions at the BØ interaction point of the Tevatron. It is a general purpose, cylindrical-shaped detector (Fig. 2.3), which consists of:

- a **tracking system**, which comprises three silicon microstrip trackers (Layer 00, SVXII and ISL) and an open-cell drift chamber (COT) inside a superconducting solenoid, that provides a constant $1.4T$ magnetic field parallel to the beam direction, with the purpose of reconstructing the trajectories (helices) of charge particles and determining their momentum and charge;
- a **Time of Flight** system (TOF), located outside the COT, for identification of charged particles with momenta up to $2 GeV/c$;
- a **calorimeter system**, with the purpose of measuring the energy of charged and neutral particles;
- **muon chambers and scintillators**, used to track and identify muons, that pass through the calorimeters interacting as minimum-ionizing-particles (m.i.p.);
- **luminosity monitors**, for the instantaneous luminosity measurement, necessary to predict event yields.

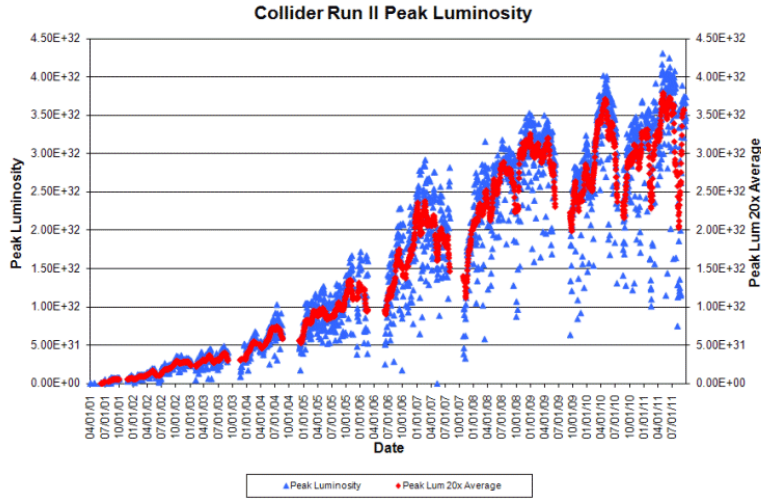
2.2.1 Coordinates System and Standard Definitions at CDF

CDF adopts a left handed Cartesian coordinate system with origin at the nominal BØ interaction point, coincident with the center of the drift chamber. The positive z -axis lies along the nominal beam-line and has the direction of the proton beam (eastwards). The x - y plane is therefore perpendicular to the beam-line, with the y -axis pointing

⁴The beta function represents a measure of the transverse beam size along the accelerator ring. β^* is the value of this function at the collision point.



(a)



(b)

Figure 2.2: Integrated luminosity as a function of the Run II weeks (2.2a) and Tevatron peak luminosity as a function of the calendar date (2.2b). Empty periods correspond to Tevatron shut-down periods.

upwards and the x -axis in the horizontal plane, pointing radially outward with respect to the center of the accelerator ring. Since the colliding beams of the Tevatron are unpolarized, the resulting physical observations are invariant under rotations around the beam line axis. Thus, a cylindrical (r, ϕ, z) coordinate system is particularly convenient to describe the detector geometry, where

$$r = \sqrt{x^2 + y^2} \quad \text{and} \quad \phi = \tan^{-1} \frac{y}{x}. \quad (2.2.1)$$

A momentum-dependent particle coordinate, named *rapidity*, is also commonly

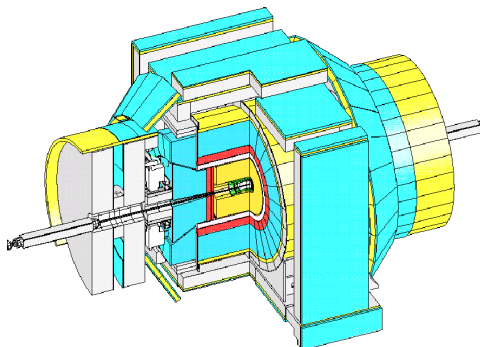


Figure 2.3: Isometric view of the CDF II Detector.

used in particle physics for its transformation properties under Lorentz boosts. The rapidity is defined as

$$Y = \frac{1}{2} \ln \frac{E + p_z}{E - p_z}, \quad (2.2.2)$$

where E is the energy and p_z is the z component of the particle momentum. Rapidity intervals turn out to be Lorentz invariant. In the relativistic limit, or when the mass of the particle is negligible, rapidity depends only upon the production angle of the particle with respect to the beam axis, $\theta = \tan^{-1} \frac{\sqrt{x^2 + y^2}}{z}$. This approximation is called *pseudorapidity* η and is defined as

$$Y \xrightarrow{p \gg m} \eta = -\ln \left(\tan \frac{\theta}{2} \right). \quad (2.2.3)$$

A value of $\theta = 90^\circ$, perpendicular to the beam axis, corresponds to $\eta = 0$. Since the event-by-event longitudinal position of the interaction is distributed around the nominal interaction point with a 30 cm rms width, sometimes a distinction between the detector pseudorapidity (usually indicated with η_{det}), measured with respect to the $(0,0,0)$ nominal interaction point, and the event pseudorapidity (η), which is measured with respect to the z position of the actual event vertex, is considered. The spatial separation between particles in the detector is commonly given in terms of a Lorentz invariant variable defined as:

$$\Delta R = \sqrt{\Delta\phi^2 + \Delta\eta^2}. \quad (2.2.4)$$

Other quantities, useful to describe the kinematics of $p\bar{p}$ interactions, are the transverse momentum and the transverse energy, defined as $p_T = p \sin \theta$ and $E_T = E \sin \theta$, respectively.

2.3 The Tracking System

A three-dimensional tracking of charged particles is achieved through an integrated system consisting of three inner silicon subdetectors and a large outer drift-chamber, all immersed in the magnetic field of a superconducting solenoid. The silicon detectors provide a precise determination of the track impact parameter, the azimuthal angle and the z coordinate, whereas the drift chamber has excellent resolution on the

transverse momentum, ϕ and η . The combined information of the tracking detectors provides very accurate measurements of the helical paths of charged particles inside the detector. We will describe this system starting from the devices closest to the beam and moving outwards (see Fig. 2.5a).

2.3.1 The Silicon Tracker

The full CDF silicon detector is composed of three approximately cylindrical coaxial subsystems: the Layer 00 (L00), the *Silicon Vertex* detector (SVX) and the Intermediate *Silicon Layers* (ISL). Silicon sensors operate as reverse-biased p - n junctions. When a charged particle passes through the detector, it releases energy and ionizes the material producing electron-hole pairs. If an electric field is applied the electrons and holes drift to opposite electrodes. The amount of charge collected at the anode and the cathode is proportional to the path length traversed by the charged particle in the detector. By segmenting the p or n side of the junctions into “strips” and reading out the charge deposition separately on every strip we can measure the position of the charged particle. At CDF the typical distance between two strips is about $60\ \mu\text{m}$. There are two types of microstrip detectors: single- and double-sided. In single-sided detectors only one side (p) of the junction is segmented into strips, double-sided detectors have both sides of the junction segmented into strips. In general single-sided sensors have strips parallel to the z direction and provide only r - ϕ position measurements, while double-sided detectors have strips at an angle (stereo angle) with respect to the z direction on one side and, therefore, provide also information on the particle position along z .

L00 is a $90\ \text{cm}$ -long, radiation hard, assembly of single sided silicon detectors, structured in longitudinal strips. It is mounted directly on the beam pipe at $1.35 - 1.62\ \text{cm}$ from the beam axis. The detector support structure is in carbon fiber with integrated cooling system. Being so close to the beam, L00 allows to reach a resolution of $\sim 25 - 30\ \mu\text{m}$ on the impact parameter of tracks of moderate p_T , providing a powerful handle to identify long-lived hadrons containing a b quark.

SVX is composed of three $29\ \text{cm}$ -long cylindrical barrels, radially organized in five layers of double-sided silicon wafers extending from $2.5\ \text{cm}$ to $10.7\ \text{cm}$ (see Fig. 2.4a). Each barrel is segmented into 12 wedges, each covering $\sim 30^\circ$ in ϕ . The double-side structure of the wafers allows a three dimensional position measurement: one side of the wafer has axial strips (parallel to the beam), the other one has either 90° strips (perpendicular to the beam) or 1.2° stereo strips (at small angle with respect to the beam). This detector provides position information with a $12\ \mu\text{m}$ resolution on the single hit and some dE/dx ionization information.

ISL consists of two layers of double sided silicon wafers, similar to those of SVX, one of which is assembled in a twofold telescopes with planes at a radial distance of $22\ \text{cm}$ and $29\ \text{cm}$ from the beam-line and covering $1 < |\eta| < 2$. One single central layer is located at $r = 22\ \text{cm}$, covering $|\eta| < 1$. The two ISL layers are important to increase the tracking coverage in the forward region, where the COT coverage is limited, and to improve the matching between SVX and COT tracks.

The combined resolution of the CDF inner trackers for high momentum tracks is $\sim 40\ \mu\text{m}$ in impact parameter and $\sim 70\ \mu\text{m}$ along the z direction. All silicon detectors are used in the off-line track reconstruction algorithms, while SVX plays a

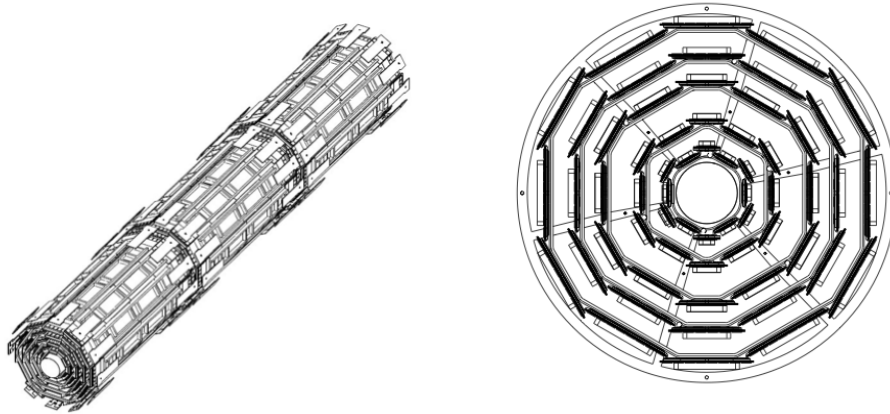


Figure 2.4: The SVX silicon detector: on the left, a three-dimensional view of the detector allows to see the barrel structure along the beam axes; on the right, the transverse plane section shows in detail the layer sequence.

crucial role also in the on-line track reconstruction of the trigger system. The CDF trigger employs an innovative processor, the Silicon Vertex Trigger (SVT) [19, 4], which uses the SVX information to measure the track impact parameter on-line with a precision that allows to resolve the secondary vertices, displaced from the primary interaction point, produced in B hadron decays.

2.3.2 Central Outer Tracker

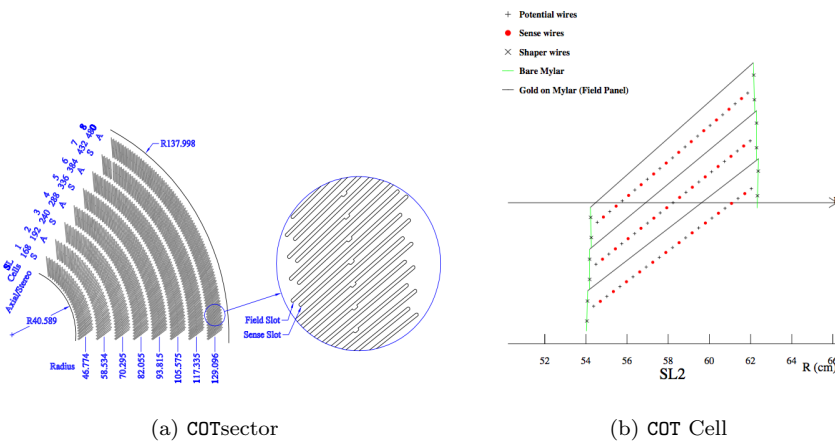


Figure 2.5: A 1/6 section of the COT end-plate (2.5a): for each super-layer the total number of cells, the wire orientation (axial or stereo), and the average radius in [cm] are given. The enlargement shows in detail the slot where the wire planes (sense and field) are installed. Fig. 2.5 represents the cross-section of three axial cells in super-layer 2, the arrow indicates the radial direction.

Surrounding the silicon detector is the Central Outer Tracker (COT) [2]. It is a 3.1 m-long cylindrical drift chamber, coaxial with the beam, which covers the radial

range from 40 to 137 *cm* for $|\eta| < 1$. The COT contains 96 sense wire layers, which are radially grouped into 8 superlayers, as inferred from the end plate slot structure shown in Fig. 2.5. Each superlayer is divided in ϕ into supercells, and each supercell has 12 alternated sense and field shaping wires. So within the supercell width the trajectory of a particle is sampled 12 times. The maximum drift distance is approximately the same for all superlayers. Therefore, the number of supercells in a given superlayer scales approximately with the radius of the superlayer. The entire COT contains 30240 sense wires. Approximately half the wires run along the z direction (*axial*), the other half are strung at a small stereo angles (2°) with respect to the z direction (*stereo*). The combination of the axial and stereo information allows to measure the z positions and a three-dimensional reconstruction of tracks. Particles originated from the interaction point, which have $|\eta| < 1$, pass through all the 8 COT superlayers. The COT is filled with an Argon-Ethane gas mixture and isopropyl alcohol (49.5:49.5:1). The mixture is chosen to have a constant drift velocity, approximately $50 \mu\text{m}/\text{ns}$, across the cell width. When a charged particle passes through a chamber cell, the gas is ionized and pairs of free electrons and positive ions are created. The electric field inside the cell attracts the electrons towards the sense wires. As the electrons get closer to the wires the field intensity become more and more intense until, eventually, an avalanche multiplication of charge occurs due to electron-atom collisions, providing a gain of $\sim 10^4$. The movement of charges in the cell electric field induces a signal on the sense wire, a “hit”, which is read out by electronics. The maximum electron drift time is approximately 100 *ns*. Due to the magnetic field that the COT is immersed in, electrons drift at a Lorentz angle of 35° . The supercells are tilted by 35° with respect to the radial direction to compensate for this effect and make the drift path perpendicular to the radial direction.

The hit position resolution in the r - ϕ plane is about 140 μm . Tracking algorithms are utilized to reconstruct particle trajectories (helices) that best fit to the observed hits. The reconstructed trajectories are referred to as “tracks”. Particle momentum and charge are determined from the bending of tracks in the magnetic field. The COT hits are also processed on-line by the XFT, which reconstructs the tracks used in the trigger system, (Sec. 3.1.4). The transverse momentum resolution of off-line tracks, estimated using cosmic ray events, is:

$$\frac{\sigma_{p_T}}{p_T^2} = [0.017][\text{GeV}/c]^{-1} \quad (2.3.1)$$

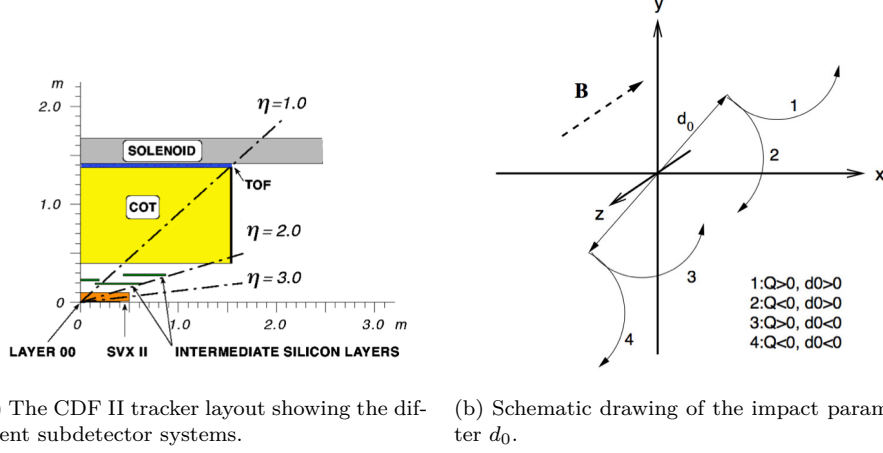
for tracks with $p_T > 2 \text{ GeV}/c$ [1].

2.3.3 Track Reconstruction

Charged particles traveling through a homogeneous solenoidal magnetic field along the z direction follow helical trajectories. Knowing that the projection of the helix on the x - y plane is a circle, to uniquely parametrize a helix in three dimensions, five parameters are needed:

C – signed helix (half)-curvature, defined as $C = q/2R$, where R is the radius of the helix and q is the particle charge. This is directly related to the transverse momentum. When the magnetic field (B) is measured in Tesla, C in m^{-1} and p_T in GeV/c : $p_T = 0.15 qB/|C|$.

ϕ_0 – ϕ azimuthal angle of the particle trajectory at the point of closest approach to the z -axis.


 Figure 2.6: CDF tracking subdetectors and impact parameter d_0 definition.

d_0 – signed impact parameter, i.e. the radial distance of closest approach to the z -axis. defined as $d_0 = q(\sqrt{x_0^2 + y_0^2} - R)$, where (x_0, y_0) are the coordinates of the center. This is schematically drawn in Fig. 2.6b.

λ – helix pitch, i.e. $\cot(\theta)$, where θ is the polar angle of the particle at the point of its closest approach to the z -axis. This is directly related to the longitudinal component of the momentum: $p_z = p_T \cot \theta$.

z_0 – the z coordinate of the point of closest approach.

Another useful quantity is the displacement of the secondary vertices of decaying particles in the transverse plane, L_{xy} :

$$L_{xy} = \frac{\hat{x}_V \cdot \vec{p}_T}{|p_T|} \quad (2.3.2)$$

where \hat{x}_V is the decay vertex position in the transverse plane.

The trajectory of a charged particle satisfies the following equations

$$\begin{aligned} x &= r \sin \phi - (r - d_0) \sin \phi_0 \\ y &= -r \cos \phi + (r + d_0) \cos \phi_0 \\ z &= z_0 + s\lambda \end{aligned} \quad (2.3.3)$$

where s is the projected length along the track, $r = 1/2C$ and $\phi = 2Cs + \phi_0$. The reconstruction of a charged particle trajectory consists in determining the above parameters through an helical fit of a set of spatial measurements (“hits”) reconstructed in the tracking detectors by clustering and pattern-recognition algorithms. The helical fit takes into account field non-uniformities and scattering by the detector material. All tracks are first fit in the COT and then extrapolated inward the silicon. This approach guarantees fast and efficient tracking with high tracks purities. The greater radial distance of the COT with respect to the silicon tracker results in a lower track density and consequent fewer accidental combination of hits in the track reconstruction. A brief overview of the tracking algorithms is given in the following, for more details see Ref. [7], [14].

2.3.4 Tracking Algorithm

Using the hit positions in the tracking system, pattern recognition algorithms reconstruct the particle original trajectory measuring the five parameters of the helix that best match to the observed hits.

CDF employs several algorithms for track reconstruction, depending on which component of the detector a particle travels through. The principal one is the Outside-In (OI) reconstruction. This algorithm, which exploits the information from both the central drift chamber and the silicon detectors, is used to track the particles in the central region ($|\eta| < 1$). It first reconstructs tracks in the COT and then extrapolates them inwards toward the beam.

The first step of pattern recognition in the COT looks for circular paths⁵ in the axial superlayers. Cells in the axial superlayers are searched for sets of 4 or more hits that can be fit to a straight line. These sets are called “segments”. Once segments are found, there are two approaches to track finding [18] (“segment linking” and “histogram linking” algorithms). One approach is to link together the segments which are consistent with lying tangent to a common circle. The other approach is to constrain its circular fit to the “beam-line” (see Sec. 2.3.5). Once a circular path is found in the r - ϕ plane, segments and hits in the stereo superlayers are added depending on their proximity to the circular fit. This results in a three-dimensional track fit. Typically, if one algorithm fails to reconstruct a track, the other algorithm will not. This results in high track reconstruction efficiency in the COT for tracks passing through all 8 superlayers (97% for tracks with $p_T > 10 \text{ GeV}/c$)⁶.

Once a track is reconstructed in the COT, it is extrapolated inward to the silicon system. Based on the estimated errors on the track parameters, a three dimensional “road” is formed around the extrapolated track. Starting from the outermost layer, and working inwards, silicon hits found inside the road are added to the track. As hits are added, the road gets narrowed according to the knowledge of the updated track parameters and their covariance matrix. A reduction of the road width decreases the chance of adding wrong hits to the track, and also reduces the computation time. In the first pass of this algorithm, axial hits are added. In the second pass, hits with stereo information are added to the track. At the end, the track combination with the highest number of hits and lowest χ^2/ndf for the five parameters helix fit is kept.

2.3.5 Primary Vertex Reconstruction

The primary vertex position for a given event is found by fitting high quality tracks to a common point of origin. At high luminosities, multiple collisions occur on a given bunch crossing. For a luminosity of $10^{32} \text{ cm}^{-2} \text{ s}^{-1}$, there is an average of 2.3 interactions per bunch crossing. Typically, since the luminous region is sufficiently long (with $\sigma_z = 29 \text{ cm}$), the primary vertices associated to the collisions are well separated in z . An iterative algorithm is used to find the vertex associated to the hardest collision: the first estimate of its position (x_V, y_V, z_V) is binned in the z coordinate, then the z position of each vertex is calculated from the weighted average of the z coordinates of all tracks within 1 cm of the first iteration vertex, with a typical

⁵The helical track, when projected onto the r - ϕ plane, is a circle.

⁶The track reconstruction efficiency mostly depends on how many tracks are reconstructed in the event. If there are many tracks close to each other, hits from one track can shadow hits from the other track, resulting in efficiency losses.

resolution of $100\ \mu\text{m}$; finally the vertex associated with the highest sum of the tracks p_T is defined as primary vertex of the event.

The locus of all primary vertices defines the beam-line, the position of the luminous region of the beam-beam collisions through the detector. The beam-line is used as a constraint to refine the knowledge of the primary vertex in a given event. Typically the beam transverse section is circular with a width of $\sim 30\ \mu\text{m}$ at $z = 0$, rising to $\sim 50 - 60\ \mu\text{m}$ at $|z| = 40\ \text{cm}$. The beam is not necessarily parallel nor centered in the detector and moves as a function of time.

2.4 Calorimeters

The calorimeter system, together with the muon and tracking systems, represents one of the main sub-detector apparatuses of CDF II detector. A detailed description of this system can be found in the CDF II Technical Design Report [6]. The CDF II calorimetry system has been designed to measure energy and direction of neutral and charged particles leaving the tracking region. In particular, it is devoted to jet reconstruction and it is also used to measure the missing energy associated to neutrinos. Particles hitting the calorimeter can be divided in two classes, according to their main interaction with matter: electromagnetically interacting particles, such as electrons and photon, and hadronically interacting particles, such as mesons or baryons produced in hadronization processes. To detect these two classes of particles, two different calorimetric parts have been developed: an inner electromagnetic and an outer hadronic section, providing coverage up to $|\eta| < 3.64$. In order to supply information on particle position, the calorimeter is also segmented in towers, projected toward the geometrical center of the detector. Each tower consists of alternating layers of passive material and scintillator tiles. The signal is read out via wavelength shifters (WLS) embedded in the scintillator and light from WLS is then carried by light guides to photomultiplier tubes. The central sector of the calorimeter, covering the region $|\eta| < 1.1$, was recycled from Run I, while brand new calorimeters (called plug calorimeters) were built up to cover the forward and backward regions. Fig. 2.7b shows the plug calorimeter system while Fig. 2.7c shows an elevation view of the components of the CDF calorimeter: CEM, CHA, WHA, PEM and PHA.

2.4.1 The Central Electromagnetic Calorimeter

Apart from upgrades on the readout electronics, needed to cope with the increased collision rate, the central calorimeter is almost the same as in Run I. The Central Electro-Magnetic calorimeter (CEM) is segmented in $\Delta\eta \times \Delta\phi = 0.11 \times 15^\circ$ projective towers consisting of 31 alternate layers of lead and scintillator, for a total material depth of $19\ X_0$ ⁷. The Central and End-Wall Hadronic calorimeters (CHA and WHA respectively), whose geometry tower segmentation matches the CEM one, use 32 steel layers sampled each $2.5\ \text{cm}$ by $1\ \text{cm}$ thick acrylic scintillator. The total thickness of the hadronic section is approximately constant and corresponds to 4.5 interaction

⁷The radiation length X_0 describes the characteristic amount of matter transversed by high energy electrons to lose all but $1/e$ of their energy due to bremsstrahlung, which is equivalent to $7/9$ of the length of the mean free path for e^+e^- pair production of high energy photons. The average energy loss due to bremsstrahlung for an electron of energy E is related to the radiation length by $\left(\frac{dE}{dx}\right)_{brem} = -\frac{E}{X_0}$

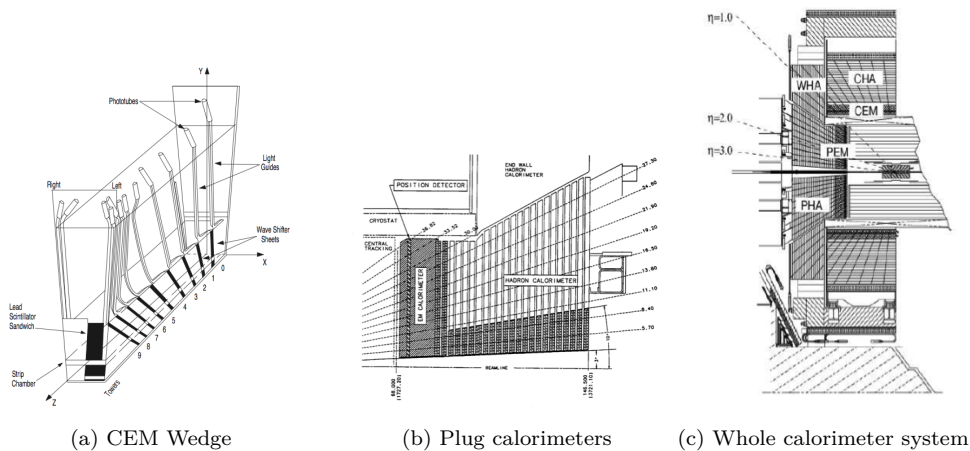


Figure 2.7: One azimuthal electromagnetic calorimeter wedge 2.7a, the elevation view of one quarter of the plug calorimeter 2.7b. In 2.7c elevation view of the CDF detector showing the components of the CDF calorimeter: CEM, CHA, WHA, PEM and PHA.

lengths (λ_0)⁸. A perspective view of a central electromagnetic calorimeter module (*wedge*) is shown in Fig. 2.7a, where both the arrangement in projected towers and the light-gathering system are visible. The projective geometry has been used in order to take advantage of the momentum conservation in the transverse plane: before the $p\bar{p}$ collision, the projection in the transverse plane w.r.t. the beam direction of the beam energy is zero, therefore this quantity has to be the same also after the collision took place. Thus, for each tower the transverse energy E_T is defined as $E_T = E \sin \theta$, where E is the energy detected by the tower and θ is the angle between the beam axis and the tower direction, in the CDF detector coordinates system. Two position detectors are embedded in each wedge of CEM:

- The Central Electromagnetic Strip chamber (CES) is a two-dimensional strip-wire chamber arranged in correspondence to maximum shower development ($\sim 5.9X_0$). It measures the charge deposit of the electromagnetic showers, providing information on their pulse-height and position with a finer azimuthal segmentation than calorimeter towers. This results in an increased purity on electromagnetic object reconstruction. The CES purpose is to measure the position and the shape of electromagnetic showers in both transverse plane and longitudinal direction, which is used to distinguish electrons and photons from hadrons.
- The Central Pre-Radiator (CPR) consists of two wire chamber modules placed immediately in front of the calorimeter. It acts as pre-shower detector by using the tracker and the solenoid coil material as radiators, resulting to be a very useful tool in rejection of electron and photon background.

⁸An interaction length is the average distance that a particle will travel before interacting with a nucleus: $\lambda = \frac{A}{\rho\sigma N_A}$, where A is the atomic weight, ρ is the material density, σ the cross section and N_A the Avogadro number.

Tab. 2.2 summarizes the basic quantities of calorimeter detectors. The energy resolution for each calorimeter section was measured in the test beam and, for a perpendicularly incident beam, can be parametrized as:

$$\frac{\sigma}{E} = \frac{\sigma_1}{\sqrt{E}} \oplus \sigma_2 \quad (2.4.1)$$

where the first term comes from the sampling fluctuations and the photostatistics of the PMTs, (stochastic term) and the second term comes from the non-uniform response of the calorimeter (constant term).

2.4.2 The Plug Calorimeter

The plug calorimeter, covers the η region from 1.1 to 3.64. Both electromagnetic and hadronic sectors are divided in 12 concentric η regions, with $\Delta\eta$ ranging from 0.10 to 0.64, according to increasing pseudorapidity, each of them is segmented in 48 or 24 (for $|\eta| < 2.11$ or $|\eta| > 2.11$ respectively) projective towers. The actual size of these towers was chosen so that identification of electron in b -jets would be optimized. Projective towers consist of alternating layers of absorbing material (lead and iron for electromagnetic and hadronic sectors, respectively) and scintillator tiles. The first layer of the electromagnetic tiles is thicker (10 mm instead of 6 mm) and made of material with higher photon yield. It acts as a pre-shower detector.

Calorimeter	CEM	CHA	WHA	PEM	PHA
Absorber	Lead	Steel	Steel	Lead	Iron
Segmentation ($\eta \times \phi$)	0.1×15	0.1×15	0.1×15	(0.1 ÷ 0.6)×(7.5 ÷ 15)	(0.1 ÷ 0.6)×(7.5 ÷ 15)
Num. Towers ($\eta \times \phi$)	20×24	9×24	6×24	12×24(48)	11×24(48)
Thickness	[19] $X_{0,1} \lambda_0$	4.7 λ_0	4.7 λ_0	[23] $X_{0,1} \lambda_0$	6.8 λ_0
Resolution (%)	14/ $\sqrt{E_T} \oplus 2$	50/ $\sqrt{E_T} \oplus 3$	75/ $\sqrt{E_T} \oplus 4$	16/ $\sqrt{E} \oplus 1$	80/ $\sqrt{E} \oplus 5$

Table 2.2: Summary of the main characteristics of the CDF II calorimeter system.

2.5 Muon Detectors

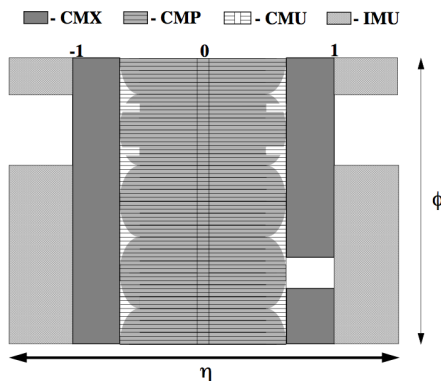


Figure 2.8: Muon detectors coverage in the η - ϕ plane.

Most of the particles produced in the primary interaction or in subsequent decays have a very high probability of being absorbed in the calorimeter system. Muons represent

Parameter	CMU	CMP	CMX	IMU
Pseudorapidity range	$ \eta < 0.6$	$ \eta < 0.6$	$0.6 < \eta < 1.0$	$1.0 < \eta < 1.5$
Azimuthal coverage [°]	360	360	360	270
Maximum drift time [ns]	800	1400	1400	800
Drift tube cross section[cm]	2.68×6.35	2.5×15	2.5×15	2.5×8.4
Pion interaction length	5.5	7.8	6.2	62 - 20.0
Minimum $p_T(\mu)$ [GeV/c]	1.4	2.2	1.4	1.4-2.0

Table 2.3: Design parameters of the muon detectors. Assembled from Ref. [9], [3]

an exception. They are over 200 times more massive than electrons, so bremsstrahlung radiation, inversely proportional to the mass squared of the incident particle, is suppressed by a factor of $4 \cdot 10^4$ with respect to electrons. Muons do not interact via strong interaction with nuclei in matter either. Therefore, a muon with enough energy will pass through the calorimeter systems releasing only a small amount of its energy. At CDF the minimum muon energy required to reach the muon detectors, placed radially outside of the calorimeters, is 1.4 GeV . The muon system is the outermost layer of the CDF II detector and consists of four layers of drift cells and scintillation counters which are used to reconstruct track segments (“stubs”) of minimum ionizing particles. These stubs are matched using dedicated algorithms with the COT information in order to reconstruct the full trajectory of the muons. Some additional steel shielding layers, in between the chambers and the calorimeters, reduce the probability for other particles to escape the calorimetric system. Four independent systems detect muons in the $|\eta| \lesssim 1.5$ pseudo-rapidity range reconstructing a small segment of their path (stub) sampled by the chambers, employing similar combinations of drift tubes, scintillation counters, and absorbers with differential azimuthal coverage [9], [3]. The momentum measurement is performed by pointing back the stub to the corresponding track in the COT. Scintillators serve as trigger and vetoes while the drift chambers measure the ϕ coordinate using the absolute difference of drift electrons arrival time between two cells, and the z coordinate by charge division. All types of muon detectors use single wire, rectangular drift chambers, arranged in arrays with fine azimuthal segmentation and coupled with scintillator counters. The chambers use a 50:50 gas admixture of Argon and Ethane, and operates in proportional regime. The four sub-detector systems are (see Fig. 2.8):

- CMU:** the CMU detector is located around the central hadronic calorimeter at a radius of 347 cm from the beam-line with coverage $0.03 \lesssim |\eta| \lesssim 0.63$. It is segmented into 24 wedges of 15° , but only 12.6° in ϕ , with a gap of 2.4° , of each wedge is active, resulting in an overall azimuthal acceptance of 84%. Each wedge is further segmented into three 4.2° modules each containing four layers of four drift cells.
- CMP:** the CMP is a second set of muon drift chambers outside of CMU with an additional 60 cm -thick steel absorber between them. The material further reduces the probability of hadronic punch-through to the CMP. Muons need a transverse momentum of about 2.2 GeV to reach the CMP. The CMP system is arranged in a box shape of similar acceptance as the CMU and conventionally serves as a confirmation of CMU for higher momentum muons. A layer of scintillation counters (CSP) is mounted on the outer surfaces of the CMP. The CMP and CMU have a large overlap in coverage and are often used together. CMP helps to cover CMU ϕ gaps and the CMU covers the CMP η gaps. Muon candidates which have both CMU

and CMP stubs are the least contaminated by fake muons.

CMX: the CMX consists of drift tubes and scintillation counters (CSX) assembled in conically arranged sections. The CMX extends the pseudo-rapidity coverage to $0.6 \lesssim |\eta| \lesssim 1$. There are 8 layers of drift chambers in total with a small stereo angle between layers.

IMU: the IMU extends the pseudo-rapidity coverage even further to $1.0 \lesssim |\eta| \lesssim 1.5$. The IMU is mounted on the toroid magnets which provide shielding and consists of BMU, BSU and TSU.

Tab. 2.3 summarizes a few of the relevant design parameters of these detectors.

Chapter 3

The Online Trigger Selection

3.1 The CDF Trigger System

At the Tevatron collisions occur at a frequency of 2.5 MHz (i.e every 396 ns). With an average event size of $\sim 250\text{ Kb}$ this represents a huge amount of data which would flow through the CDF data acquisition system (DAQ). The CDF DAQ can sustain only a small fraction of this data flow, the maximum rate for storing data to disk is $\sim 200\text{ Hz}$. The trigger is the system devoted to perform a quick online selection and keep only the events interesting for physics. A rejection factor of 10000 is needed to match the DAQ capabilities. As shown in Fig. 3.1, the CDF trigger is implemented in three levels of successively tighter and more sophisticated event selections.

The first level is hardware based, while the second is a mixture of hardware and software and the third is represented by a computer cluster.

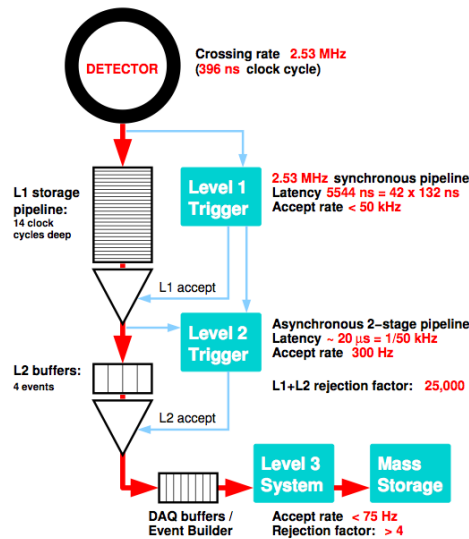


Figure 3.1: Functional block diagram of the CDF II trigger and data acquisition systems.

3.1.1 LEVEL 1

At **LEVEL 1** the decision logic is implemented in hardware, that is the selection algorithms are hard-coded into the electronic circuits of the trigger boards. In a synchronous pipeline up to 42 subsequent events can be stored for $\sim 5.5 \mu s$ while the hardware is taking a decision. If no acceptance decision is made within that time the event is lost. L1 decision are made on average in about $4 \mu s$: no dead time is expected from this level. Level 1 rejects 97% of the events, it reduces the event rates from $2.53 MHz$ to less than $40 kHz$. The L1 decision is generated using

- XFT (extremely fast tracker), which reconstructs approximate tracks ($p_T > 1.5 GeV$) in the transverse plane by exploiting information from COT superlayers. These tracks are extrapolated to the calorimeters and muon chambers parts to contribute to all trigger levels.
- the calorimeter towers, which carry information in the electromagnetic and hadronic energy deposits (these can be seed for electrons or jets identification).
- the muon “stubs” (segment of tracks reconstructed in the muon chambers), which are matched to the XFT tracks.

The XFT is a custom processor used to reconstruct two-dimensional tracks in the (r, ϕ) plane in the COT. The XFT is capable of reconstructing tracks with $p_T \gtrsim 1.5 GeV$ with an efficiency of about 95% and a fake rate of a few percent. The XFT has an angular segmentation of 1.25° , and an angular resolution of 0.3° . The momentum resolution is $\sigma_{p_T}/p_T^2 \approx 0.017 [GeV/c]^{-1}$. XFT sends the tracks to the extrapolation unit (XTRP) which feeds three L1 elements: L1 CAL, L1 TRACK, and L1 MUON. L1 CAL and L1 MUON use extrapolated tracks and information from the calorimetry and muon systems respectively to search for possible electron, photon, jets and muon candidates. A decision stage combines the information from these low-resolution physic objects, called “primitives”, into more sophisticated objects, e.g., track primitives are matched with muon stubs or tower primitives, to form muon, electron, or jet object, which are subject to basic selection. The accepted events are buffered for L2 analysis.

3.1.2 LEVEL 2

LEVEL 2 is an asynchronous system which processes events that have received a L1 accept in a FIFO (First In, First Out) manner. It is structured as a two stage pipeline with data buffering at the input of each stage. The first stage is based on dedicated hardware processor which assemble information from a particular section of the detector. The second stage consists of a computer which uses the list of objects generated by the first stage and implements in software the event selection. Each of the L2 stages is expected to take approximately $10 \mu s$ with a latency of approximately $20 \mu s$. The L2 buffers can store up to four events. After the Level 2, the event rate is reduced to about $1 kHz$ (rejection factor ~ 40). L2 purposes are:

- to cluster the energy deposited in the towers around L1 seeds, as an approximate measure of an electron photon or jet energy.
- to use calorimeter and CES chamber information to improve separation of e^\pm from γ .
- to improve the matching between XFT tracks and muon stubs in order to have a better muon signature.

- to provide a measurement of the track impact parameters (Silicon Vertex Triggers), which allow to select events with secondary vertexes from decay of long-lived heavy flavour hadrons.

The Silicon Vertex Trigger (SVT) uses SVX $r - \phi$ hits to extend XFT track primitives inside the SVX volume, closer to beam-line. The SVT improves the XFT ϕ_0 and p_T resolutions and adds the measurement of the impact parameter d_0 (original XFT track primitives are beam-line constrained).

3.1.3 LEVEL 3

LEVEL 3 is a software trigger. It consists of a cluster of ~ 300 processors which reconstruct the entire event with the same accuracy as in the off-line analysis. The final decision to accept an event is made on the basis of a list of observables indicating candidate events of physical interest (top quark production events, W/Z events, Drell-Yan events, etc.). Events that satisfy the Level 3 trigger requirements are then transferred onward to the Consumer Server/Data Logger (CSL) system for storage first on disk and later on tape. The average processing time per event in Level 3 is on the order of one second. The Level 3 leads to a further reduction in the output rate, with an accepted maximum of about 200 Hz.

3.1.4 Trigger Paths

A set of requirements that an event has to fulfill at Level 1, Level 2 and Level 3 constitutes a trigger path. The CDF II trigger system implements about 150 trigger paths, which are periodically adjusted depending on machine luminosity and physics needs. An event will be accepted if it passes the requirements of any one of these paths. The trigger system described above exploits the information of all detector subsystems and combining the measurements of the various subsystems it is possible to efficiently record, at the same time, events characterized by different signatures. Triggers which use a bandwidth fraction larger than the assigned one are prescaled. A trigger path is said to be prescaled by a factor N if it is configured to accept only one event out of N accepted events. Prescaling is dynamically implemented by luminosity-dependent factors during data taking. This is important in order to ensure that no trigger path reaches rates so high as to create unacceptable dead time to triggers on rare events of primary importance. During data taking the luminosity decreases with time, and consequently a number of prescale factors can be relaxed. The prescale factors decrease proportionally to the rate of triggered events, so as the number of recorded events is constant. Using dynamic prescaling ensures that optimal use is made for physics of the available luminosity.

The accepted events are recorded to tape and organized in “data sets” according to the trigger path which satisfy.

3.2 Trigger Paths used in the $H \rightarrow WW$ Analysis

The search $H \rightarrow WW$ exploits the leptonic decays of the weak vector bosons, which ensure a cleaner experimented signature. Therefore, the trigger paths which select events with a high p_T electron or muon are the most suitable to carry on the search. In the following we will briefly describe the online selection of the *high- p_T* electron and muon paths.

For the electrons we used the following trigger paths

ELECTRON_CENTRAL_18 This trigger path, selects electron candidates in the central region ($|\eta| < 1.1$) that satisfy

- At LEVEL 1 this trigger requires a tower in the central calorimeter with at least 8 GeV and $E_{had}/E_{EM} < 0.125$ (to distinguish the electromagnetic energy from an energy deposit due to charged hadrons) which is associated to an XFT track with $p_T > 8\text{ GeV}/c$.
- At LEVEL 2 is required an electromagnetic cluster of at least 18 GeV and $|\eta| < 1.317$.
- At LEVEL 3 we want here that $L_{shr} < 0.4$, this is a variable that compares lateral shower profiles in towers next to the seed tower to some expected profile; Δz between the COT track and the CEM shower to match within 8 cm ; a central track with $p_T \geq 9\text{ GeV}/c$ matched to an electromagnetic cluster with transverse energy, $E_T > 18\text{ GeV}$.

MET_PEM Due to the high value of the *missing transverse energy*, \cancel{E}_T , that the associated production $WH \rightarrow WWW \rightarrow \ell\nu\ell\nu\ell\nu$ tends to show, in this analysis we are also interested in the events that have an energy cluster in the plug electromagnetic calorimeter in association with \cancel{E}_T . The trigger requirements are the following

- At LEVEL 1 a plug calorimeter tower with $E_T > 8\text{ GeV}$ and $E_{had}/E_{EM} < 0.0625$ is required; a $\cancel{E}_T > 15\text{ GeV}$ is also required.
- At LEVEL 2 we want a $\cancel{E}_T > 15\text{ GeV}$ cut, a plug electromagnetic cluster object with $E_T > 20\text{ GeV}$ and $1.1 < |\eta| < 3.6$.
- LEVEL 3 requires an electromagnetic object in the plug calorimeter with $E_T > 20\text{ GeV}$, $E_{had}/E_{EM} < 0.125$ and $\cancel{E}_T > 15\text{ GeV}$.

For the muons we use

MUON_CMUP18 This trigger path selects muons with tracks in both the CMU and CMP Detectors

- At LEVEL 1 we ask for an XFT track with $p_T > 4.09\text{ GeV}/c$, associated to a CMU stub with and a CMP stub.
- At LEVEL 2 the requirement on the XFT is tightened, a track with four COT superlayers having $p_T > 15\text{ GeV}/c$.
- At LEVEL 3 the p_T cut is raised to $18\text{ GeV}/c$.

MUON_CMX18 This trigger path identifies high- p_T muons that pass through the CMX muon detector

- At LEVEL 1 is required an XFT track with $p_T > 8\text{ GeV}/c$ associated to a CMX stub and a hit in the CSX scintillator.
- LEVEL 2 tightens the XFT criteria by requiring a four layer track with $p_T > 15\text{ GeV}/c$.
- At LEVEL 3 the p_T cut is raised to $18\text{ GeV}/c$.

MUON_CMP18_PHI_GAP This trigger path accounts for gaps in ϕ coverage between the calorimeter wedges which have the CMU muon chambers attached to the outer edge. Basically the requirement is to have tracks that point towards a gap to be matched with a CMP stub and a CSP hit.

- At LEVEL 1 this trigger requires an XFT track with $p_T > 15 \text{ GeV}/c$.
- At LEVEL2 the requirements on the XFT track is confirmed and furthermore a CSP hit is matched to the track.
- At LEVEL 3 a track with $p_T > 18 \text{ GeV}/c$ and matched to CMP stub ($|x_{track} - x_{CMP}| < 20 \text{ cm}$) is required.

Chapter 4

Physical Object Reconstruction

4.1 Lepton Reconstruction and Identification

Lepton reconstruction depends on the type of lepton and its direction inside the detector, in this analysis we are interested in the identification of electrons, muons and hadronically decaying taus. In the following we will present a brief overview of the identification criteria we used in this work.

4.1.1 Electron Identification

Electrons are identified by requiring a track matched to an energy cluster in the calorimeter with an appropriate shower profile. The cluster reconstruction starts with an energetic tower in the electromagnetic calorimeter, the *seed tower*. Electrons are assumed to be massless and, in order to reconstruct the four momentum, (E, \vec{p}) , track information is used to determine the three dimensional direction, $\vec{p}/|\vec{p}|$, while the calorimetric energy measurement gives the magnitude $E \equiv |\vec{p}|$. We used the following electron categories

Tight Central Electrons (TCE) Central electrons ($|\eta| < 1.0$) with high p_T are expected to traverse the silicon and COT detectors, leaving behind a track. Then they enter the EM calorimeter where they will produce an electromagnetic shower and deposit their energy. The selection criteria applied to identify the *tight central electrons* are reported in Tab. 4.1. The observable used are

- Track p_T is the transverse momentum of the track associated to the EM cluster.
- Track z_0 is the position along the longitudinal direction at the point of closest approach to the beam-line.
- *Axial and Stereo Superlayers*, (SL) are the numbers of axial and stereo superlayers in the COT having at least 5 hits associated to the track in question.
- $Q \times \Delta x_{CES}$ is the distance in the $r - \phi$ plane between the extrapolated track and the nearest cluster reconstructed in the CES detector multiplied by the charge

of the track to account for asymmetric tails originated from bremsstrahlung radiation.

- E_{had}/E_{EM} is the ratio between the energy deposited in the hadronic calorimeter and the energy deposit in the electromagnetic one.
- E/P is the ratio of the EM cluster transverse energy to the track transverse momentum as measured by the tracking system; expected to be ~ 1 for the electrons.
- $CalIso$ is the calorimetric isolation, defined as

$$CalIso \equiv \frac{E_T^{\Delta R=0.4} - E_T^e}{E_T^e} \quad (4.1.1)$$

where $E_T^{\Delta R=0.4}$ is the transverse energy in a cone of radius $\Delta R \leq 0.4$, with $\Delta R = \sqrt{(\Delta\eta)^2 + (\Delta\phi)^2}$, around the electron cluster and E_T^e is the energy in the electron cluster.

- L_{shr} , the lateral shower profile, compares the energy distributions of the EM towers adjacent to the seed tower to the distribution derived from electron test-beam data.
- Δz_{CES} is the distance in the $r - z$ plane between the extrapolated track and the best matching CES cluster.

	TCE
Region	central ($ \eta < 1.0$)
Fiducial	track fiducial to CEM
Track p_T	≥ 10 (5 if $E_T < 20 \text{ GeV}$)
Track $ z_0 $	$\leq 60 \text{ cm}$
# Ax SL (5hits)	≥ 3
# St SL (5hits)	≥ 2
Conversion	false
E_{had}/E_{EM}	$\leq 0.055 + 0.00045 \cdot E [\text{GeV}]$
$CalIso$	≤ 0.1
L_{shr}	\leq
E/P	$< 2.5 + 0.015 \cdot E_T [\text{GeV}]$
$\Delta x \cdot Q$	$-3 \leq q \cdot \Delta x \leq 1.5 \text{ cm}$
Δz_{CES}	$< 3 \text{ cm}$
Track	Beam constrained

Table 4.1: Definition of fully identified Tight Central Electron (TCE).

Forward Electrons Electron candidate clusters in the plug calorimeter are made starting from a seed tower and adding neighboring towers within two towers in η_{det} and ϕ from the seed. The hadronic energy of the cluster is required to be less than 0.05 times the electromagnetic energy. Plug electrons have to be reconstructed in a well-instrumented region of the detector, defined as $1.2 \leq |\eta| \leq 2.0$ as measured by the PES sub-system (η_{det}^{PES}). To improve the quality of the track-cluster matching, we

require a track with hits in at least 3 layers of the silicon detector, given the COT limited coverage in the forward region. The track is further required to have $|z_0| < 60 \text{ cm}$. Additional requirements are summarized in Table 4.2. Some of the observable used to define the forward electrons are

- PEM $3 \times 3 \chi^2$ is the χ^2 of a fit to the signal shape in electron test beam data.
- PES $5 \times 9 \text{ U/V}$ are the ratios of the charge collected in the central 5 over a set of 9 PES strips in the horizontal and vertical planes.
- $\Delta R(\text{PES}, \text{PEM})$ is the angular distance between the PEM and the PES clusters.

	PHX
Region	Plug
$ \eta_{det}^{PES} $	$1.2 \leq \eta_{det}^{PES} \leq 2.0$
E_{had}/E_{EM}	≤ 0.05
PEM $3 \times 3 \chi^2$	≤ 10
PES $5 \times 9 \text{ U}$	≥ 0.65
PES $5 \times 9 \text{ V}$	≥ 0.65
$CalIso$	≤ 0.1
$\Delta R(\text{PES}, \text{PEM})$	≤ 3.0
$NSiHits$	≥ 3
Track z_0	$\leq 60 \text{ cm}$

Table 4.2: Definition of Forward Electrons (PHX)

Likelihood-Based Electrons (LBE) In order to maintain an high efficiency in rejecting fake electrons one defines a set of variables to be combined in a single discriminant to be allied in a likelihood method. The quantities considered are

- $TrkIso$ is similar to the above variable but measured using tracks instead of calorimeter towers.
- $NCotHitsAx$ is the number of Axial COT super-layers hits belonging to the track associated to the candidate electron.
- $NCotHitsSt$ is the number of Stereo COT super-layers hits belonging to the track associated to the candidate electron.
- χ_{COT}^2 is the χ^2 of the track fit computed using only the COT hits belonging to the track.
- $NSvxHits$ is the number of SVX hits belonging to the track associated to the candidate electron.

These variables, together with that defined in Sec. 4.1.1, are used to form the likelihood

$$\mathcal{L} = \frac{L_{sig}}{L_{sig} + L_{bkg}} = \frac{\prod_{i=1}^N P_i^{sig}(x_i)}{\prod_{i=1}^N P_i^{sig}(x_i) + \prod_{i=1}^N P_i^{bkg}(x_i)} \quad (4.1.2)$$

where x_i is one of the variable listed above; N is the number of ID variables, in this case, 11; P_i^{sig} and P_i^{bkg} are the probability function of getting the x_i value off the i -th ID variable given a *real* or a *fake* electron (*template* in the following).

Data is used to build signal (from real electrons) and background (from fake electrons) templates selecting sample dominated by real or by fake electrons. Real electrons are obtained selecting two events in the *Z-mass region* (i.e. with an invariant mass in the $76 < m_{\ell\ell} < 106 \text{ GeV}/c^2$ window), a *fully* identified electron and a *probe* one with opposite charge. A fully identified electron is selected through the previous variables and the cuts defined in Tab. 4.1. *Probe* electrons are required to have an identified electron-like cluster associated with a track with looser selection as listed in Tab. 4.3. The ID variables of probe objects are used to make the signal templates.

Fake electrons are obtained from a jets data sample (jets are defined in Sec. 4.1.3). This sample is selected by requiring at least one jet with energy greater than 20 GeV . One reconstructed jet with $E_T > 20 \text{ GeV}$ and a loose electron, a *fakeable* one (the definition is in Tab. 4.4), per event is required, with an invariant mass out the *Z*-peak region (i.e. $m_{\ell\ell} < 76 \text{ GeV}$ or $m_{\ell\ell} > 106 \text{ GeV}$). The ID variables of fakeable objects are used to build the background template.

	Central Electron Probe
Region	Central
Track p_T	$\geq 5 \text{ GeV}/c$
Track z_0	$\leq 60 \text{ cm}$
Conversion	false

Table 4.3: Definition of central electron probe.

	Fakeable Central Electron
Region	Central
E_{had}/E_{EM}	$\leq 0.125 + 0.00045 E[\text{GeV}]$
$CalIso$	< 0.3
Conversion	false

Table 4.4: Definition of central electron fakeable object.

4.1.2 Muon Identification

Muons traverse the entire CDF detector, depositing a negligible amount of energy in the calorimeters, and leave hits in the outer muon chambers, in cases where they point to a region which is covered by them. A muon is reconstructed starting from a track and adding track segments (stubs) formed with hits in the muon drift chambers. The track origin in the $x - y$ plane is constrained to the beam position. The muon four momentum (E, \vec{p}) is determined by measuring the track p and assuming a massless particle: $E \equiv |\vec{p}|$. Muons are reconstructed in eight non-overlapping categories. Six of them require the muons to have hits in one muon detector subsystem, and we call them stubbed muons. The other two are designed to recover muons that do not have a stub and are referred as stubless muons. To further increase acceptance we also define an extra lepton category in which both electrons and muons can fall. This category accepts leptons which fall in regions of the detector not fully instrumented (cracks) and fails electron and muon selections.

Stubbed Muon Stubbed muon candidates are required to have a reconstructed track with a fit $\chi^2/n.d.f. < 3$. The track is required to have at least three Axial and two Stereo COT super-layers with at least 5 hits. The track $|z_0|$ has to be less than 60 cm. For forward muons (BMU) we have a limited coverage from the COT drift chamber, so we removed the hits requirement and we instead require a number of hits in the chamber that is at least 60% of the expected one, based on the track direction; we also require at least three hits in the Silicon detectors and a curvature significance $C/\sigma(C) > 12$. For all muons, the distance at the closest approach of the extrapolated track to the primary vertex, which is called impact parameter (d_0), has to be less than 0.2 cm, and it is tightened to be less than 0.02 cm if the track has also hits in the Silicon detectors, giving a much precise measurement of the impact parameter. To reject background we also require the track to be isolated: $TrkIso < 0.1$, where $TrkIso$ is defined as

$$TrkIso \equiv \frac{\sum_i p_T^{i, \Delta R=0.4} - p_T}{p_T} < 0.1 \quad (4.1.3)$$

The reconstructed track is then required to be compatible with a minimum ionizing particle (*m.i.p.*) by cutting on the energy deposited in the EM and HAD towers hit by the extrapolated track. We also require calorimetric isolation

$$CalIso = \frac{E_T^{\Delta R=0.4}}{p_T^\mu} \quad (4.1.4)$$

where $E_T^{\Delta R=0.4}$ has been defined above and p_T^μ is the track transverse momentum. Stubbed muons are divided in six categories, depending on the region of the detector that the extrapolated track is pointing to, CMUP, CMU, CMP, CMX, CMxMsKs and BMU. We measure the location of an extrapolated muon track candidate with respect to the drift direction (local x) and wire axis (local z) of a given chamber. We do not take into account possible multiple scattering in the extrapolation. We refer to these requirements as fiduciality of the track to the given muon detector. The fiduciality requirements ensure that all the categories are non-overlapping: a given muon cannot be classified into two different categories. The cuts applied to each category are summarized in Tables 4.6- 4.10.

	CMUP
Region	Central
Track $\chi^2/n.d.f.$	≤ 3
$NAxL$ (5 hits)	≥ 3
$NStL$ (5 hits)	≥ 2
Track z_0	≤ 60 cm
Track d_0	≤ 0.2 cm (≤ 0.02 cm if N $SiHits > 0$)
$TrkIso$	≤ 0.1
$CalIso$	≤ 0.1
E_{EM}	$\leq 2 + \max(0, (p - 100) \cdot 0.0115)$ GeV
E_{had}	$\leq 6 + \max(0, (p - 100) \cdot 0.028)$ GeV
Δx_{CMU}	≤ 7 cm
Δx_{CMP}	$\leq \max(6.0, 150/p_T [GeV/c^2])$ cm
Fiduciality	$x\text{-fid}_{CMU} < 0$ cm $z\text{-fid}_{CMU} < 0$ cm $x\text{-fid}_{CMP} < 0$ cm $z\text{-fid}_{CMP} < -3$ cm

Table 4.5: Definition of CMUP central muons.

	CMU
Region	Central
Track $\chi^2/n.d.f.$	≤ 3
<i>NAxL</i> (5 hits)	≥ 3
<i>NStL</i> (5 hits)	≥ 2
Track z_0	$\leq 60\text{ cm}$
Track d_0	$\leq 0.2\text{ cm}(\leq 0.02\text{ cm if N SiHits} > 0)$
<i>TrkIso</i>	≤ 0.1
<i>CalIso</i>	≤ 0.1
E_{EM}	$\leq 2 + \max(0, (p - 100) \cdot 0.0115)\text{ GeV}$
E_{had}	$\leq 6 + \max(0, (p - 100) \cdot 0.028)\text{ GeV}$
Fiduciality	$x\text{-fid}_{CMU} < 0\text{ cm } z\text{-fid}_{CMU} < 0\text{ cm}$ Not CMP Fiducial Not CMX Fiducial
Δx_{CMU}	$\leq 7\text{ cm}$
Good Trigger	Run > 270062

Table 4.6: Definition of CMU central muons. CMU wasn't used till RUN 270012 due to a bug.

	CMP
Region	Central
Track $\chi^2/n.d.f.$	≤ 3
<i>NAxL</i> (5 hits)	≥ 3
<i>NStL</i> (5 hits)	≥ 2
Track z_0	$\leq 60\text{ cm}$
Track d_0	$\leq 0.2\text{ cm}(\leq 0.02\text{ cm if N SiHits} > 0)$
<i>TrkIso</i>	≤ 0.1
<i>CalIso</i>	≤ 0.1
E_{EM}	$\leq 2 + \max(0, (p - 100) \cdot 0.0115)\text{ GeV}$
E_{had}	$\leq 6 + \max(0, (p - 100) \cdot 0.028)\text{ GeV}$
Fiduciality	$x\text{-fid}_{CMP} < 0\text{ cm } z\text{-fid}_{CMP} < -3\text{ cm}$ Not CMU Fiducial
Δx_{CMU}	$\leq 7\text{ cm}$
Δx_{CMP}	$\leq \max(6.0, 150/p_T [GeV/c])\text{ cm}$
ϕ - gaps	$\phi \bmod 15^\circ \leq 2\text{ OR } \geq 13$
Good Trigger	Run > 229764

Table 4.7: Definition of CMP central muons.

Stubless Muon Stubless muons are recovered by selecting an isolated high-pT track which deposited in the calorimeter an amount of energy consistent with a minimum ionizing track. Two categories are defined

- CMIOCES are the central stubless muons fiducial to the central calorimeter.
- CMIOPEs are the forward stubless muons fiducial to the plug calorimeter.

The requirements of these two categories are reported in Table 4.11 and 4.12.

CrkTrk To further increase the acceptance the leptons that fall in a crack of the sub-detectors are recovered. To specifically select these leptons and to preserve the

	CMX
Region	Central
Track $\chi^2/n.d.f.$	≤ 3
<i>NAxL</i> (5 hits)	≥ 3
<i>NStL</i> (5 hits)	≥ 2
Track z_0	$\leq 60\text{ cm}$
Track d_0	$\leq 0.2\text{ cm}(\leq 0.02\text{ cm if N SiHits} > 0)$
<i>TrkIso</i>	≤ 0.1
<i>CalIso</i>	≤ 0.1
E_{EM}	$\leq 2 + \max(0, (p - 100) \cdot 0.0115)\text{ GeV}$
E_{had}	$\leq 6 + \max(0, (p - 100) \cdot 0.028)\text{ GeV}$
Fiduciality	$x\text{-fid}_{\text{CMX}} < 0\text{ cm } z\text{-fid}_{\text{CMX}} < -3\text{ cm}$ $-0^\circ < \phi < 75^\circ\text{ OR}$ $105^\circ < \phi < 225^\circ\text{ OR}$ $315^\circ < \phi < 360^\circ$ $\rho_{\text{cot}} > 140\text{ cm}$
Δx_{CMX}	$\leq \max(6.0, 125/p_T [\text{GeV}/c])\text{ cm}$
ϕ - gaps	$\phi \bmod 15^\circ \leq 2\text{ OR } \geq 13$
Good Trigger	Run ≥ 227704

 Table 4.8: Definition of CMX central muons. The exit radius, ρ_{cot} is defined as $\rho_{\text{cot}} = (z_{\text{cot}} - z_0) \cdot \tan \theta$

	CMXsKs
Region	Central
Track $\chi^2/n.d.f.$	≤ 3
<i>NAxL</i> (5 hits)	≥ 3
<i>NStL</i> (5 hits)	≥ 2
Track z_0	$\leq 60\text{ cm}$
Track d_0	$\leq 0.2\text{ cm}(\leq 0.02\text{ cm if N SiHits} > 0)$
<i>TrkIso</i>	≤ 0.1
<i>CalIso</i>	≤ 0.1
E_{EM}	$\leq 2 + \max(0, (p - 100) \cdot 0.0115)\text{ GeV}$
E_{had}	$\leq 6 + \max(0, (p - 100) \cdot 0.028)\text{ GeV}$
Fiduciality	$x\text{-fid}_{\text{CMX}} \leq 0\text{ cm } z\text{-fid}_{\text{CMX}} \leq -3\text{ cm}$ $-3 (75^\circ < \phi < 105^\circ\text{ AND } \eta < 0)$ OR $(225^\circ < \phi < 315^\circ)$ $\rho_{\text{cot}} > 140\text{ cm}$
Δx_{CMX}	$< \max(6.0, 125/p_T [\text{GeV}])\text{ cm}$
ϕ - gaps	$\phi \bmod 15^\circ \leq 2\text{ OR } \geq 13$
Good Trigger	Run ≥ 227704

Table 4.9: Definition of CMXsKs central muons.

uniqueness of the categories the track has not to be fiducial to the central or plug calorimeter and we explicitly veto overlaps with stubbed muon categories. The selection criteria are similar to CMIOCES muons, but we do not require any deposit in the calorimeter, since these tracks point to or near the cracks in the calorimeter. However we still require a low calorimeter and tracking activity near the track (*CalIso* and

	BMU
Region	Forward
COT Hit Fraction	≥ 0.6
$NSiHits$	≥ 3
Track z_0	$\leq 60\text{ cm}$
Track d_0	$\leq 0.02\text{ cm}$
$C/\sigma(C)$	> 12
$TrkIso$	≤ 0.1
$CalIso$	≤ 0.1
E_{EM}	$\leq 2 + \max(0, (p - 100) \cdot 0.0115)\text{ GeV}$
E_{had}	$\leq 6 + \max(0, (p - 100) \cdot 0.028)\text{ GeV}$
$E_{EM} + E_{had}$	$> 0.1\text{ GeV}$
Fiduciality	$x\text{-fid}_{BMU} \leq 0\text{ cm}$ $z\text{-fid}_{BMU} \leq -3\text{ cm}$ PES fiducial $471.6 \leq z_{BMU} \leq 766.6$ OR $-433.0 \leq z_{BMU} \leq -764.7$
$N_{stubhits}$	> 2

Table 4.10: Definition of BMU central muons.

	CMIOCES
Region	Central
$NAxL(5\text{ hits})$	≥ 3
$NStL(5\text{ hits})$	≥ 3
Track $\chi^2/n.d.f.$	≤ 3
Track z_0	$\leq 60\text{ cm}$
Track d_0	$\leq 0.02\text{ cm}$
$TrkIso$	≤ 0.1
$CalIso$	≤ 0.1
E_{EM}	$\leq 2 + \max(0, (p - 100) \cdot 0.0115)\text{ GeV}$
E_{had}	$\leq 6 + \max(0, (p - 100) \cdot 0.028)\text{ GeV}$
$E_{EM} + E_{had}$	$> 0.1\text{ GeV}$
Fiduciality	CES Fiducial
Uniqueness	Not a CMUP, CMU, CMP, CMX, CMXMsKs

Table 4.11: Definition of CMIOCES central muons.

$TrkIso$) which is fundamental in order to reduce fake lepton identification. We further require the track not to be consistent with a conversion electron. Table 4.13 lists the detailed selection criteria applied.

4.1.3 Jet Reconstruction

The color-carrying quarks and gluons, created in the scattering process, undergo the hadronization process which produces collimated bunches of colorless hadrons (jets) which keep track of the energy and the direction of the originating parton. To reconstruct jets CDF uses a “cone algorithm”, which consists of three steps.

In the first step preclusters are built from adjacent “seed towers” (calorimeter

	CMIOPES
Region	Plug
COT hit fraction	≥ 0.6
<i>NSiHits</i>	≥ 3
Track z_0	$\leq 60 \text{ cm}$
Track d_0	$\leq 0.02 \text{ cm}$
$C/\sigma(C)$	> 12
<i>TrkIso</i>	≤ 0.1
<i>CalIso</i>	≤ 0.1
E_{EM}	$\leq 2 + \max(0, (p - 100) \cdot 0.0115) \text{ GeV}$
E_{had}	$\leq 6 + \max(0, (p - 100) \cdot 0.028) \text{ GeV}$
$E_{EM} + E_{had}$	$> 0.1 \text{ GeV}$
Fiduciality	PES Fiducial
Uniqueness	Not a BMU

Table 4.12: Definition of CMIOPES central muons.

	CrkTrk
<i>NAxL</i> (5 hits)	≥ 3
<i>NStL</i> (5 hits)	≥ 3
Track $\chi^2/n.d.f.$	≤ 3
Track z_0	$\leq 60 \text{ cm}$
Track d_0	$\leq 0.02 \text{ cm}$
$C/\sigma(C)$	> 12
<i>TrkIso</i>	≤ 0.1
<i>CalIso</i>	≤ 0.1
	OR
	≤ 0.1 using nearest EM cluster with $\Delta R = 0.05$
$E_{EM} + E_{had}$	$> 0.1 \text{ GeV}$
Fiduciality	Not PES Fiducial Not CES Fiducial
Uniqueness	Not a CMUP, CMU, CMP, CMX, CMXMsKs

Table 4.13: Definition of CrkTrk central muons.

towers with $E_T > 1 \text{ GeV}$). The size of these preclusters is limited to $2R_{\text{cone}} \times 2R_{\text{cone}}$ in the η - ϕ plane, where R_{cone} is the parameter of the jet algorithm which controls the size of the jets.

After that for each precluster a cone is defined by all seed towers inside the precluster and all towers with $\Delta R = \sqrt{\Delta\eta^2 + \Delta\phi^2} < R_{\text{cone}}$ with respect to the highest E_T tower. The centroids of the cones are calculated. The identification of the members of the cones and the calculation of their centroids is repeated until the old centroids (the cone axes) agree with the new ones.

In the last step overlapping stable cones have to be treated because each calorimeter tower may only belong to one jet. A pair of overlapping cones is merged if more than 75% of the transverse energy of one of the cones is shared by the other one. Otherwise they are separated using an iterative algorithm. The towers are redistributed to the cone whose centroid is closer and the centroids are recalculated until a stable configuration is reached.

The transverse energy and the position of the reconstructed jet are then given by $E_T^{\text{jet}} = \sum_i E_T^i$, $\eta = \frac{1}{E_T^{\text{jet}}} \sum_i E_T^i \eta^i$, $\phi = \frac{1}{E_T^{\text{jet}}} \sum_i E_T^i \phi^i$, where E_T^i , η^i and ϕ^i are the energy and the position of the i -th tower.

4.2 Hadronic Tau Reconstruction

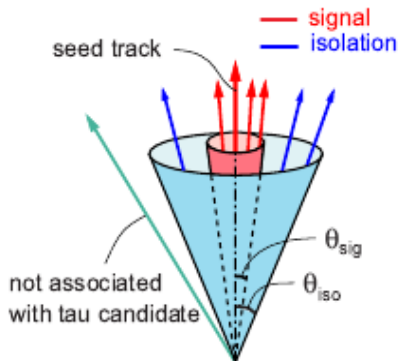


Figure 4.1: Tau signal cone and isolation annulus for tracks and π^0 's.

Tau leptons have two main decay modes, *leptonic decays* into the final states $e\nu_e\nu_\tau$ and $\mu\nu_\mu\nu_\tau$ and *hadronic decays*, $\tau \rightarrow X_h\nu_\tau$, with X_h a system of hadrons, mostly charged and neutral pions. By hadronic reconstruction, we mean the reconstruction of the hadronic system X_h and call it “hadronic tau”. In this analysis we focus only on the hadronic tau decays. Unlike the case of electrons and muons, since the tau neutrino escapes detection, a complete reconstruction of the tau four momentum is precluded.

Taus appear in the detector as a narrow calorimeter cluster matched to a collimated bunch of tracks. The reconstruction procedure starts with finding a seed calorimeter tower with $E_T^{\text{seed tower}}$ greater than some threshold; adjacent shoulder towers with energy $E_T^{\text{sh tower}}$ are added to form the tau calorimeter cluster. The number of tower contributing to the tau cluster, N^{tower} , is required to be small due to the narrowness of tau energy deposit. The next step is to find a seed track for the tau candidate that has a transverse momentum $p_T^{\text{seed track}}$ greater than some fixed threshold. In the case of many tracks, the one with higher p_T is chosen. The direction of the seed track is defined as the *reference direction*. Other COT tracks are associated to the tau based on their proximity to the selected seed track. These shoulder tracks are associated to the tau if they have a transverse momentum $p_T^{\text{sh track}} > 1 \text{ GeV}/c$ and are included in a cone of opening angle θ_{sig} (*signal cone*) around the reference direction. Tracks in the signal cone, are considered tau decay products. Outside the signal cone an isolation annulus is defined as $\theta_{sig} < \theta < \theta_{iso}$, see Fig. 4.1.

Neutral pions are associated with the tau candidate following the same procedure as for shoulder tracks. They are reconstructed using CES clusters to determine the position and the CEM to assign the energy. The π^0 four momenta are then calculated using the reconstructed π^0 energy, the π^0 mass and the direction from the tau production vertex to the π^0 cluster position. The tau reconstruction cuts are summarized in Tab. 4.14. Most of the jets are also reconstructed as taus and a tighter selection

has to be applied to reduce the overwhelming jet contamination. The identification criteria are

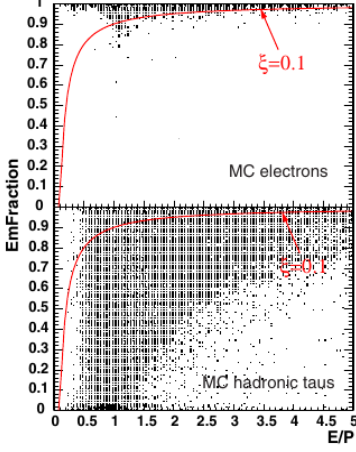


Figure 4.2: Electromagnetic fraction vs. E/P for MC taus and electrons. Entries with $\xi > 0.1$ are in the region below the solid line.

- transverse energy of the tau calorimetric cluster: $E_T^{\text{clu}} > 10 \text{ GeV}$;
- transverse momentum of the seed track: $p_T^{\text{seed trk}} > 10 \text{ GeV}/c$;
- impact parameter of the seed track: $|d_0^{\text{seed trk}}| < 1 \text{ cm}$;
- seed track z_0 : $|z_0^{\text{seed trk}}| < 60 \text{ cm}$;
- CES detector fiduciality: $9 < |z_{CES}^{\text{seed trk}}| < 230 \text{ cm}$;
- track isolation, defined as the scalar sum of the p_T 's of all tracks with $p_T > 1 \text{ GeV}/c$ in the isolation cone: $I_{\text{trk}} < 2 \text{ GeV}/c$;
- no tracks with $p_T > 1.5 \text{ GeV}/c$ in the isolation cone;

- π^0 isolation, defined as the sum of the E_T 's of all π^0 's with $E_T > 1 \text{ GeV}$ reconstructed in the isolation cone: $I_{\pi^0} < 1 \text{ GeV}$;
- number of tracks with $p_T > 1 \text{ GeV}/c$ in the signal cone: $N_{\text{trk}}^{\text{sig cone}} = 1$ (“1-prong taus”) or 3 (“3-prong taus”);
- total charge of the tracks associated to the reconstructed tau: $|\sum Q_{\text{trk}}| = 1$;
- ratio of the total energy deposited in the calorimeter to the total momentum of the tracks associated to the tau: $E^{\text{clu}} / \sum p_{\text{trk}} > 0.8$;
- visible energy of the tau, reconstructed using tracks and π^0 's associated to the tau: $E_T^{\text{trk}+\pi^0} > 15 \text{ GeV}/c$ for 1-prong taus and $E_T^{\text{trk}+\pi^0} > 20 \text{ GeV}/c$ for 3-prong taus;
- visible mass of the tau: $M^{\text{trk}+\pi^0} < 1.8 \text{ GeV}/c^2$ for 1-prong taus and $M^{\text{trk}+\pi^0} < 2.2 \text{ GeV}/c^2$ for 3-prong taus;
- to reject electrons reconstructed as taus: $\frac{E_{\text{tot}}}{|\vec{p}|} (0.95 - E_{\text{em}}/E_{\text{tot}}) > 0.1$.

4.3 Missing Energy

Neutrinos interact with matter weakly and thus cannot be detected directly with the CDF detector. An indirect way to account for the escaping neutrinos is to measure the energy unbalance in the detector.

Tau Reconstruction	
$E_T^{seed\ trk}$	$> 6\ GeV$
$E_T^{sh\ trk}$	$> 1\ GeV$
N^{trk}	≤ 6
θ_{sig}	$\min(0.17, \frac{5[rad/GeV]}{E_T^{cl}}) rad$
θ_{iso}	$0.52\ rad$
$p_T^{seed\ trk}$	$> 6\ GeV$
$p_T^{sh\ trk}$	$> 1\ GeV$
E_T^{cl}	$> 9\ GeV$
p_T	$> 15\ GeV$ for 1-prong $> 20\ GeV$ for 3-prong
$\Delta z^{sh\ trk}$	$< 5\ cm$

Table 4.14: Tau reconstruction cut.

The energy and momentum in the transverse plane are initially taken to be zero, we can thus define the transverse component of the missing energy as

$$\vec{E}_T = - \sum_i E_T^i \hat{n}_i, \quad (4.3.1)$$

where E_T^i is the transverse energy measured in the i -th tower of the calorimeter and \hat{n}_i is the projection of the versor pointing from the event vertex to the i -th calorimeter tower onto the plane perpendicular to the beam axis.

4.4 Fake Leptons

The probability for jets to fake a lepton, the *fake rate*, is measured in the jet samples and corrected for small contribution of real isolated leptons. The jet-like objects that pass a very loose selection of lepton cuts, the *denominator objects*, are counted. Different lepton categories has different denominator objects and all of these objects may pass a full lepton definition. The master formula for the fake rate is given by

$$f_i = \frac{N_i(\text{Identified Leptons}) - \sum_{j \in \text{EWK}} N_i(\text{Identified Leptons})}{N_i(\text{Denominator Objects}) - \sum_{j \in \text{EWK}} N_i(\text{Denominator Objects})} \quad (4.4.1)$$

where the number real leptons have been subtracted from the numerator and denominator. More than one jet sample is used to estimate the fake rate and the average of these estimation is used as the fake probability.

4.5 Trigger Efficiency and Lepton Scale Factor

4.5.1 Trigger Efficiency

The efficiency is a measure of how often a given trigger path will successfully identify a certain kind of event. A lepton that could have triggered the event is called a *triggerable lepton*. Electrons and stubbed muons are triggerable leptons if $E_T > 20\ GeV$, each can be triggered by only one trigger path. Stubless muons and *CrkTrk* are not considered triggerable leptons. The trigger selection criteria are looser than that applied on the

offline selection so, indicating with N_L the number of events that passed a certain trigger path and with N_T the number of events that passed a certain trigger path and the offline selection, the efficiency is defined as

$$\epsilon_{\text{ID}} = \frac{N_T}{N_L}. \quad (4.5.1)$$

Central and forward electrons trigger efficiencies are measured selecting $W \rightarrow e\nu$ events requiring an identified triggerable electron and a significant missing transverse energy. For muon trigger efficiencies $Z \rightarrow \mu\mu$ events are selected with invariant mass of the two identified muons, $m_{\ell\ell}$, in the Z -peak mass region ($76 < m_{\ell\ell} < 106 \text{ GeV}/c^2$).

4.5.2 Lepton Scale Factor

Monte Carlo and collected data may have differences on the lepton identification (ID) efficiency that have to be taken into account. To this end a *scale factor*, s^{lep} , measured in the $Z \rightarrow \ell\ell$ events, is introduced. This correction factor is given by

$$s^{\text{lep}} = \frac{\epsilon^{\text{Data}}}{\epsilon^{\text{MC}}} \quad (4.5.2)$$

where ϵ^{Data} is the lepton identification efficiency for real data while ϵ^{MC} is for simulated data samples. The scale factor is measured for each lepton category and for several groups of run periods. We select events with one fully identified lepton (*tag*) and a second object, the *probe*, that passes looser and well simulated requirements. The tag and probe leptons are required to have opposite charge and an invariant mass $\pm 5\sigma$ around the Z peak: $76 < m_{\ell\ell} < 106 \text{ GeV}/c^2$. We also require $\cancel{E}_T < 15 \text{ GeV}$ for $e\mu$ events and $\cancel{E}_T < 25 \text{ GeV}$ for the other combinations. This ensures that the sample is orthogonal to the others used to perform the Higgs search. The identification efficiency is

$$\epsilon^\ell = \frac{N_\ell}{N_{\text{Probe}}} \quad (4.5.3)$$

where N_ℓ is the number of leptons in the selected Z events and N_{Probe} is the number of probe objects. Tab. 4.15 and Tab. 4.16 lists the measured scale factors for different run periods.

Lepton Category	Period 0	Period 1 - 4	Period 5 - 7	Period 8 - 10
CMUP	0.973 ± 0.012	0.938 ± 0.009	0.932 ± 0.013	0.955 ± 0.009
CMU	0.000 ± 1.000	0.000 ± 0.500	0.000 ± 0.577	0.000 ± 0.577
CMP	0.000 ± 1.000	0.000 ± 0.500	0.000 ± 0.577	0.965 ± 0.032
CMX	1.027 ± 0.016	1.020 ± 0.017	1.026 ± 0.019	1.007 ± 0.014
CMXMsKs	0.000 ± 1.000	0.000 ± 0.500	0.000 ± 0.577	0.930 ± 0.036
BMU	1.127 ± 0.032	1.107 ± 0.025	1.076 ± 0.032	1.099 ± 0.021
CMIOCES	1.049 ± 0.019	1.060 ± 0.015	1.085 ± 0.018	1.086 ± 0.014
CMIOPEs	1.000 ± 0.000	1.005 ± 0.020	1.029 ± 0.025	0.980 ± 0.018
<i>CrkTrk</i>	0.958 ± 0.015	0.978 ± 0.012	0.976 ± 0.015	0.973 ± 0.012
TCE	1.007 ± 0.005	0.995 ± 0.005	0.987 ± 0.006	0.975 ± 0.004
LBE	1.055 ± 0.029	1.047 ± 0.027	1.078 ± 0.034	1.174 ± 0.024
PHX	0.997 ± 0.005	1.004 ± 0.004	1.018 ± 0.005	1.000 ± 0.004
PLBE	1.158 ± 0.044	1.241 ± 0.041	1.282 ± 0.051	1.359 ± 0.035

Table 4.15: Lepton Scale Factors.

Lepton Category	Period 11 - 12	Period 13	Period 14 - 21	Period 22 - 38
CMUP	0.924 ± 0.011	0.937 ± 0.011	0.883 ± 0.006	0.848 ± 0.004
CMU	0.000 ± 0.707	0.000 ± 1.000	0.000 ± 1.000	0.874 ± 0.008
CMP	0.893 ± 0.022	0.987 ± 0.022	0.881 ± 0.012	0.830 ± 0.008
CMX	0.981 ± 0.018	0.986 ± 0.020	0.959 ± 0.007	0.947 ± 0.005
CMXMsKs	0.935 ± 0.032	0.890 ± 0.033	0.898 ± 0.015	0.871 ± 0.010
BMU	1.064 ± 0.028	1.142 ± 0.037	1.048 ± 0.016	1.047 ± 0.012
CMIOCES	1.204 ± 0.019	1.186 ± 0.022	1.155 ± 0.014	1.435 ± 0.015
CMIOPEs	0.955 ± 0.023	0.998 ± 0.037	0.949 ± 0.013	0.936 ± 0.009
<i>CrkTrk</i>	0.990 ± 0.020	0.952 ± 0.021	0.971 ± 0.010	0.961 ± 0.007
TCE	0.965 ± 0.006	0.973 ± 0.006	0.975 ± 0.003	0.957 ± 0.002
LBE	1.239 ± 0.030	1.168 ± 0.034	1.151 ± 0.015	1.210 ± 0.012
PHX	1.000 ± 0.004	1.002 ± 0.006	1.027 ± 0.002	1.026 ± 0.002
PLBE	1.217 ± 0.039	1.376 ± 0.052	1.310 ± 0.022	1.408 ± 0.017

Table 4.16: Lepton Scale Factors.

Chapter 5

The Trilepton Signature

5.1 Motivation

Since no single channel has sensitivity to probe the Standard Model Higgs boson production by itself, the strategy of the Standard Model Higgs searches at the Tevatron is to explore all accessible channels and then combine the results together.

The CDF searches for the decay mode $H \rightarrow WW$ focused on the study of events with muons and electrons in the final state, which provide a clean experimental signature with a relatively low background level.

This work is the first in CDF to extend the search to the channel with electrons, muons and hadronic taus in the final state. In particular we consider an experimental signature with three leptons (electrons, muons, taus) and a large missing transverse energy, \cancel{E}_T . Such a signature is mainly sensitive to a Standard Model Higgs produced in association to an electro-weak boson W or Z and successively decaying to two bosons, $WH \rightarrow WWW$ and $ZH \rightarrow ZWW$, where the W and Z decay leptonically. In the case $ZWW \rightarrow \ell\bar{\ell}\ell'\nu'\ell''\nu''$ one of the leptons is not reconstructed. We expect a large \cancel{E}_T from the undetected neutrinos. In the rest of this chapter the analysis strategy is presented together with the results obtained.

5.2 Event Selection

The search is carried out in $p\bar{p}$ collision data collected with the high- p_T lepton and the plug electron trigger paths (see Sec. 3.2)

- electron triggers: ELECTRON_CENTRAL_18 and MET_PEM;
- muon triggers: MUON_CMUP18, MUON_CMX18, and MUON_CMP18_PHI_GAP.

We use the full CDF Run II dataset, collected between February 2002 and September 2011, corresponding to a total integrated luminosity of 9.7 fb^{-1} .

In this analysis we used the following lepton categories

- electrons: TCE, LBE, Forward Electrons;
- muons: CMUP, CMU, CMP, CMX, BMU, CMIOCES, CMIOPEs, *CrkTrk*;
- taus: hadronic taus.

The definitions are given in chapter 4.

The events with three hadronic taus do not satisfy the trigger requirements as described in Sec. 3.2. A preliminary study has shown that events with two hadronic taus plus a muon or electron have a very unfavorable signal to background ratio, therefore such events are rejected.

We select events with three reconstructed leptons, of which one is an hadronic tau. Furthermore we require

- the total charge to be ± 1 ;
- the leptons to be associated to the same interaction vertex so $|\Delta z_{max}| < 4\text{ cm}$, where Δz_{max} is the maximum distance along the z -coordinate at the point of closest approach to the beam line between the lepton tracks.
- the p_T of the electrons and muons to be $> 20\text{ GeV}/c$ and $> 10\text{ GeV}/c$ respectively, while the hadronic tau must have a p_T greater than $15\text{ GeV}/c$ or $20\text{ GeV}/c$ for 1-prong and 3-prong taus respectively.

5.3 Backgrounds

The signature we are looking for is similar to that of a number of known Standard Model processes which mimic our signal. The dominant processes which pass the above selection can be divided in two categories

- events with three real leptons
 - WW and WZ
- events with *fake* leptons
 - $Z/W + jets$ this is the dominant background of this analysis. In this category a jet is misidentified as an hadronic tau;
 - $Z + \gamma$ here the γ can be misidentified as a lepton or a hadronic tau;
 - WW , where one W decays hadronically and the jets fake two leptons;
 - $t\bar{t}$ a $t\bar{t}$ couple decays in a pair of b -jets with two W bosons, the W bosons decay leptonically and one of the b -jets is reconstructed as a hadronic tau.

5.4 Background Modeling

Several Monte Carlo samples are used to model the backgrounds and estimate their contributions in the search region. There exist several Monte Carlo generators which present different features and are more suitable for a determined category of events. We use samples generated with PYTHIA [17] to model the electro-weak processes WW, WZ, ZZ and $t\bar{t}$. W and Z bosons produced in association with jets are better described by ALPGEN Monte Carlo [13]. The production of Z bosons associated to a photon is modeled with a dedicated generator written by U. Baur and E. L. Berger [5]. GEANT [8] is used to simulate the response of the CDF detector.

To normalize the Monte Carlo samples to the luminosity of the actual dataset we weight every Monte Carlo event with

$$w_i = \frac{f_{\text{SF}}^i \sigma_{\text{prod}} \mathcal{B} \mathcal{L}}{N_{\text{gen}}}, \quad (5.4.1)$$

where f_{SF}^i is a global scale factor which accounts for the Monte Carlo mismodeling of lepton trigger efficiencies and the reconstruction and identification efficiencies of leptons and taus, σ_{prod} is the production cross section of the simulated process, \mathcal{B} is the branching fraction into the detected final state, \mathcal{L} is the luminosity of the dataset corresponding to the used good run list and N_{gen} is the number of generated events in the Monte Carlo sample.

In order to check the background normalization and the Monte Carlo modeling of the observables used in the analysis, in particular the Monte Carlo reliability in simulating the fake objects, we define two independent control samples, whose selection is orthogonal to the phase space region where an enhancement of the Standard Model Higgs signal is expected, a missing transverse energy region, MET-region, and a Z -mass region.

5.4.1 MET Control Region

We select the MET control sampling requiring

- $20 < m_{\ell\ell} < 76 \text{ GeV}/c^2$ or $m_{\ell\ell} > 106 \text{ GeV}/c^2$ (Z mass veto), where ℓ are same flavor opposite charge leptons.
- $10 < \cancel{E}_T < 20 \text{ GeV}$.

Tab. 5.1 reports the events in data which pass this selection and the expected contributions from the background and signal processes. The agreement between data and the total background is good. Fig. 5.1 show the data-MC comparison for three representative kinematical distributions, other distributions can be found in Appendix B.1.

CDF Run II	$\int \mathcal{L} = 9.7 \text{ fb}^{-1}$	
	$m_H = 160 \text{ GeV}/c^2$	
Z/W + jets	90 ±	15
Z + γ	5.3 ±	0.8
Diboson (WW, WZ, ZZ)	0.97 ±	0.18
$t\bar{t}$	0.16 ±	0.03
Total Background	97 ±	15
WH	0.0215 ±	0.0032
ZH	0.0136 ±	0.0021
VBF	0.0015 ±	0.0003
$gg \rightarrow H$	0.0048 ±	0.0012
Total Signal	0.0414 ±	0.0041
Data	89	

HWW - trilepton channel

Table 5.1: Yields for the MET Control Region.

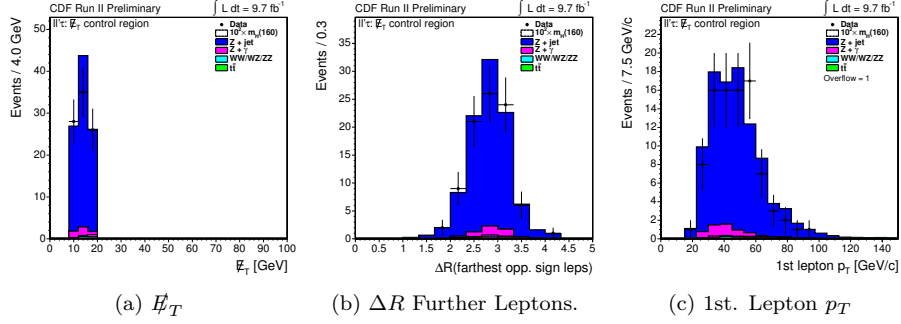


Figure 5.1: MET Control Region distribution plots.

5.4.2 Z Mass Region

This region is defined by requiring

- $76 < m_{\ell\ell} < 106 \text{ GeV}/c^2$, where ℓ are same flavor opposite charge leptons;
- $\cancel{E}_T > 20 \text{ GeV}$.

In Tab. 5.2 are reported the event yields for this region. In Fig. 5.2 are reported some representative variable distributions, they show that both the shape and the normalization of the Monte Carlo samples are in good agreement with the data. Other distributions are reported in Appendix B.2.

CDF Run II		
$m_H = 160 \text{ GeV}/c^2$		
$\int \mathcal{L} = 9.7 \text{ fb}^{-1}$		
Z/W + jets	45.7	± 7.4
Z + γ	1.1	± 0.2
Diboson (WW, WZ, ZZ)	3.7	± 0.6
$t\bar{t}$	0.26	± 0.05
Total Background	50.8	± 7.4
WH	0.015	± 0.002
ZH	0.055	± 0.008
VBF	0.0007	± 0.0002
$gg \rightarrow H$	0.0026	± 0.0008
Total Signal	0.0733	± 0.0078
Data	55	

HWW - trilepton channel

Table 5.2: Yields for the Z mass control region.

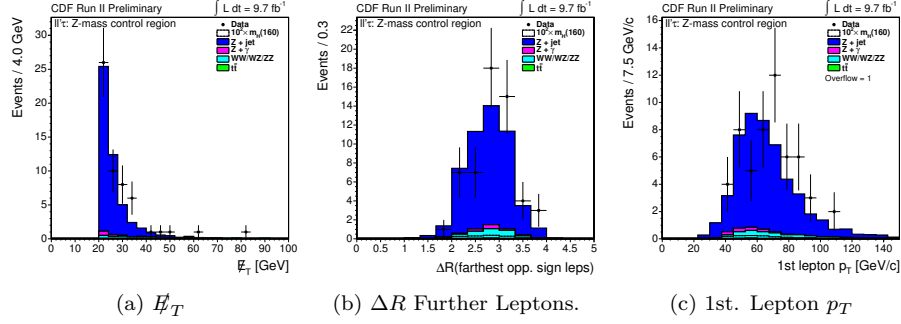


Figure 5.2: Z Control Region distribution plots.

5.4.3 Signal Region

To search for the Higgs boson is carried out in a *signal region* defined as follow

- $20 < m_{\ell\ell} < 76 \text{ GeV}/c^2$ or $m_{\ell\ell} > 106 \text{ GeV}/c^2$ (Z mass veto), where ℓ are same flavor opposite charge leptons;
- $E_T^{\text{miss}} > 20 \text{ GeV}$.

The existence of a Standard Model Higgs boson would manifest itself as an excess of the data over the expected backgrounds. The yields for this region are reported in Tab. 5.3 and as the distribution plots of some variables are shown in Fig. 5.3. In Appendix B.3 are reported other distributions.

CDF Run II		$\int \mathcal{L} = 9.7 \text{ fb}^{-1}$	
		$m_H = 160 \text{ GeV}/c^2$	
Z/W + jets	31.6	\pm	5.3
Z + γ	2.6	\pm	0.4
Diboson (WW, WZ, ZZ)	3.7	\pm	0.7
$t\bar{t}$	2.1	\pm	0.4
Total Background	40.0	\pm	5.4
WH	0.304	\pm	0.042
ZH	0.109	\pm	0.015
VBF	0.030	\pm	0.005
$gg \rightarrow H$	0.092	\pm	0.015
Total Signal	0.535	\pm	0.048
Data	28		

HWW - trilepton channel

Table 5.3: Yields for the trilepton signal sample.

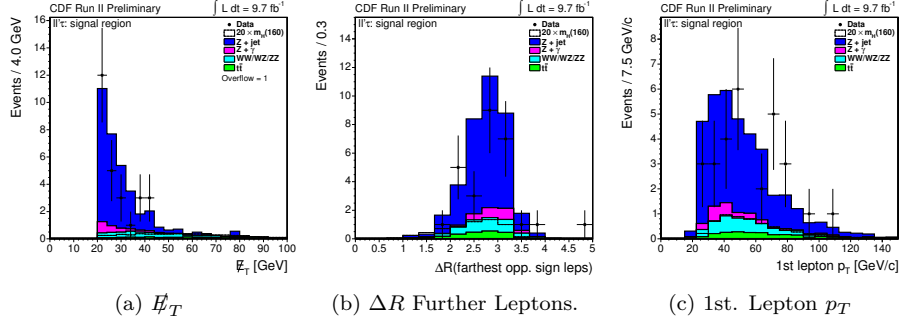


Figure 5.3: Trilepton signal region distribution plots.

5.5 Signal - Background Discrimination

To distinguish signal from background events, we used a *multivariate analysis method*, the *Boosted Decision Tree* (BDT in the following).

5.5.1 The Boosted Decision Tree

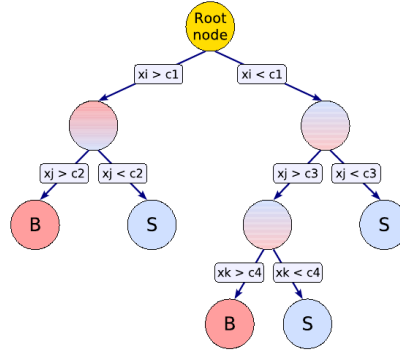


Figure 5.4: Schematic view of a decision tree.

Decision Tree A *decision tree* is a binary tree classifier based on a set of rectangular cuts applied sequentially to the variables provided as input to the tree. Fig. 5.4 shows a schematic view of a tree. The method is used to split a sample of events into two sub-samples, for example signal (S) and background (B). One defines a set of suitable variables to discriminate signal from background. The variables are ordered according to their discriminating power. Then starting with the first variable, an optimization procedure is performed to determine the splitting value that gives the best separation between one sub-sample having most background-like events and the other having more signal-like events. This is repeated for each variable until a given number of final branches, called *leaves*, are obtained, or until each leaf is pure background or pure signal. More informations can be found in [16].

Boosting After a *tree* is built as above, an event weighting is introduced in order to enhance the separation performance and make the decision robust against statistical fluctuations in the training samples. If an event is misclassified, (i.e. a signal event is classified as background or vice versa) it is *boosted* (i.e. its weight is increased). A *forest* of trees is built and the weight procedure repeated for each tree.

A score is assigned to each event, 1 if it is classified as signal and - 1 if it is classified as background. The renormalized sum of all the scores, possibly weighted, is the final score of the event. High scores mean the event is most likely signal and low scores that it is most likely background. For a detailed description of the technique see [11].

The variables used in the BDT are listed in Tab. 5.4 for three representative values of the Higgs boson mass. We use a combination of kinematical and tau identification observables

- the missing transverse energy, \cancel{E}_T ;
- the scalar sum of the transverse energies of all the reconstructed objects in the event, $\sum E_T$: \cancel{E}_T , lepton p_T 's, E_T of all jets;
- the missing energy significance, defined as $\cancel{E}_T/\sqrt{\sum E_T}$;
- the transverse momenta of the leptons and the tau, $p_T^{(1)}$, $p_T^{(2)}$, $p_T^{(3)}$, where the transverse momenta have been ordered from highest to lowest;
- the invariant mass of the two leptons and the hadronic tau, $m(\ell_1, \ell_2, \ell_3)$;
- the transverse mass of the two leptons and the hadronic tau, $m_T(\ell_1, \ell_2, \ell_3)$;
- the invariant mass of the least energetic lepton or tau and the missing energy, $m_T(\ell_3, \cancel{E}_T)$;
- the transverse mass of the two leptons, the hadronic tau, the missing energy and all the jets, $m_T(\ell_1, \ell_2, \ell_3, \cancel{E}_T, \text{jets})$;
- the invariant mass of the least energetic lepton or tau, the missing energy and all the jets, $m(\ell_3, \cancel{E}_T, \text{jets})$;
- the invariant mass of the leading and subleading leptons or tau and the missing energy, $m(\ell_1, \ell_2, \cancel{E}_T)$;
- the invariant mass of the pair of leptons closest in $\Delta\varphi$ and having opposite charge, $m(\ell^+, \ell^-)$;
- the minimum ΔR between leptons with opposite charge, $\Delta R_{min}(\ell^+, \ell^-)$;
- the maximum ΔR between leptons with opposite charge, $\Delta R_{max}(\ell^+, \ell^-)$;
- the $\Delta\varphi$ between the subleading lepton and the missing energy, $\Delta\varphi(\ell_2, \cancel{E}_T)$.

The tau ID variables are

- the seed track transverse momentum, $p_T^{\text{seed trk}}$;
- the seed track impact parameter, $d_0^{\text{seed trk}}$;
- the track isolation I_{trk} ;

- the tau visible E_T ;
- the tau visible mass;
- the scalar sum of the p_T 's of all the tracks in the isolation cone which have not been used in the tau reconstruction, $\sum_{\text{iso}} p_T^{\text{trk}}$;
- the scalar sum of the E_T 's of all the π^0 in the isolation cone which have not been used in the tau reconstruction, $\sum_{\text{iso}} E_T^{\pi^0}$;
- the p_T of the closest track to the total momentum of the tracks associated to the tau;
- the angle between the closest track and the tau track momentum, $\Delta\alpha^{\text{closest trk}}$;
- the E_T of the closest π^0 to the tau;
- the angle between the closest π^0 and the tau track momentum, $\Delta\alpha^{\text{closest } \pi^0}$.

	$m_H = 125 \text{ GeV}/c^2$	$m_H = 160 \text{ GeV}/c^2$	$m_H = 195 \text{ GeV}/c^2$
1	\not{E}_T	\not{E}_T	\not{E}_T
2	$\not{E}_T/\sqrt{\sum E_T}$	$m_T(\ell_3, \not{E}_T)$	$m_T(\ell_3, \not{E}_T)$
3	$\Delta R_{\text{min}}(\ell^+, \ell^-)$	$\not{E}_T/\sqrt{\sum E_T}$	$\not{E}_T/\sqrt{\sum E_T}$
4	$m_T(\ell_3, \not{E}_T)$	$\Delta R_{\text{MIN}}(\ell^+, \ell^-)$	$\Delta R_{\text{min}}(\ell^+, \ell^-)$
5	$\sum E_T$	$\sum E_T$	$\sum E_T$
6	$m(\ell_3, \not{E}_T, \text{jets})$	$m(\ell_3, \not{E}_T, \text{jets})$	$m(\ell_3, \not{E}_T, \text{jets})$
7	$\Delta R_{\text{max}}(\ell^+, \ell^-)$	$m(\ell_1, \ell_2, \not{E}_T)$	$m(\ell_1, \ell_2, \not{E}_T)$
8	$\Delta\varphi(\ell_2, \not{E}_T)$	$m_T(\ell_1, \ell_2, \ell_3, \not{E}_T, \text{jets})$	$m_T(\ell_1, \ell_2, \ell_3, \not{E}_T, \text{jets})$
9	$m(\ell^+, \ell^-)$	$\Delta R_{\text{max}}(\ell^+, \ell^-)$	$\Delta R_{\text{max}}(\ell^+, \ell^-)$
10	$m_T(\ell_1, \ell_2, \ell_3, \not{E}_T, \text{jets})$	$\Delta\varphi(\ell_2, \not{E}_T)$	$\Delta\varphi(\ell_2, \not{E}_T)$
11	$m(\ell_1, \ell_2, \not{E}_T)$	$p_T^{(2)}$	$p_T^{(2)}$
12	$\Delta\alpha^{\text{closest trk}}$	$p_T^{(1)}$	$p_T^{(1)}$
13	$\sum_{\text{iso}} p_T^{\text{trk}}$	$p_T^{(3)}$	$p_T^{(3)}$
14	$p_T^{\text{closest trk}}$	$\Delta\alpha^{\text{closest trk}}$	$\Delta\alpha^{\text{closest trk}}$
15	τ visible mass	$\sum_{\text{iso}} p_T^{\text{trk}}$	$\sum_{\text{iso}} p_T^{\text{trk}}$
16	$m(\ell_1, \ell_2, \ell_3)$	τ visible mass	τ visible mass
17	I_{trk}	$p_T^{\text{closest trk}}$	$p_T^{\text{closest trk}}$
18	$p_T^{(1)}$	$m_T(\ell_1, \ell_2, \ell_3)$	$m_T(\ell_1, \ell_2, \ell_3)$
19	$\Delta\alpha^{\text{closest } \pi^0}$	$m(\ell^+, \ell^-)$	$m(\ell^+, \ell^-)$
20	τ visible E_T	I_{trk}	I_{trk}
21	$m_T(\ell_1, \ell_2, \ell_3)$	$p_T^{\text{seed trk}}$	$p_T^{\text{seed trk}}$
22	$p_T^{\text{seed trk}}$	$E_T^{\text{closest } \pi^0}$	$E_T^{\text{closest } \pi^0}$
23	$E_T^{\text{closest } \pi^0}$	τ visible E_T	τ visible E_T
24	$p_T^{(2)}$	$\Delta\alpha^{\text{closest } \pi^0}$	$\Delta\alpha^{\text{closest } \pi^0}$
25	$d_0^{\text{seed trk}}$	$m(\ell_1, \ell_2, \ell_3)$	$m(\ell_1, \ell_2, \ell_3)$
26	$\sum_{\text{iso}} E_T^{\pi^0}$	$d_0^{\text{seed trk}}$	$d_0^{\text{seed trk}}$
27	$p_T^{(2)}$	$\sum_{\text{iso}} E_T^{\pi^0}$	$\sum_{\text{iso}} E_T^{\pi^0}$

Table 5.4: Ranking of the BDT input variables in the trilepton channel for $m_H = 125, 160, 195 \text{ GeV}/c^2$. The variables are defined in the text.

We saw that the better results are achieved if we trained the BDT using all signal samples, $WH, ZH, gg \rightarrow H, VBF$ against all Monte Carlo background sample, $Z/W + \text{jets}, Z + \gamma, t\bar{t}$, dibosons; each event is properly weighted. The input samples are split in a *training sample* and a *testing sample*. The BDT trained on the training

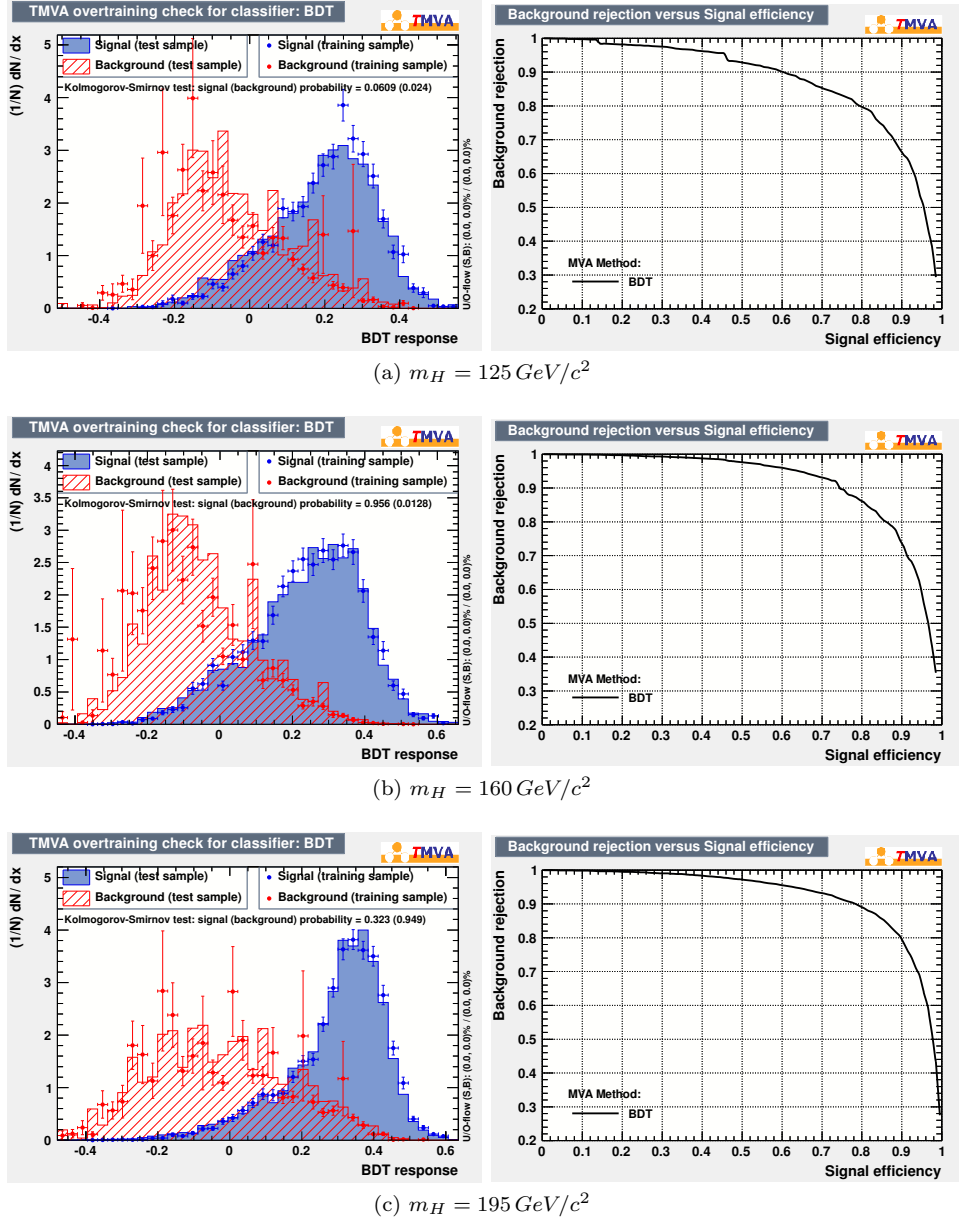
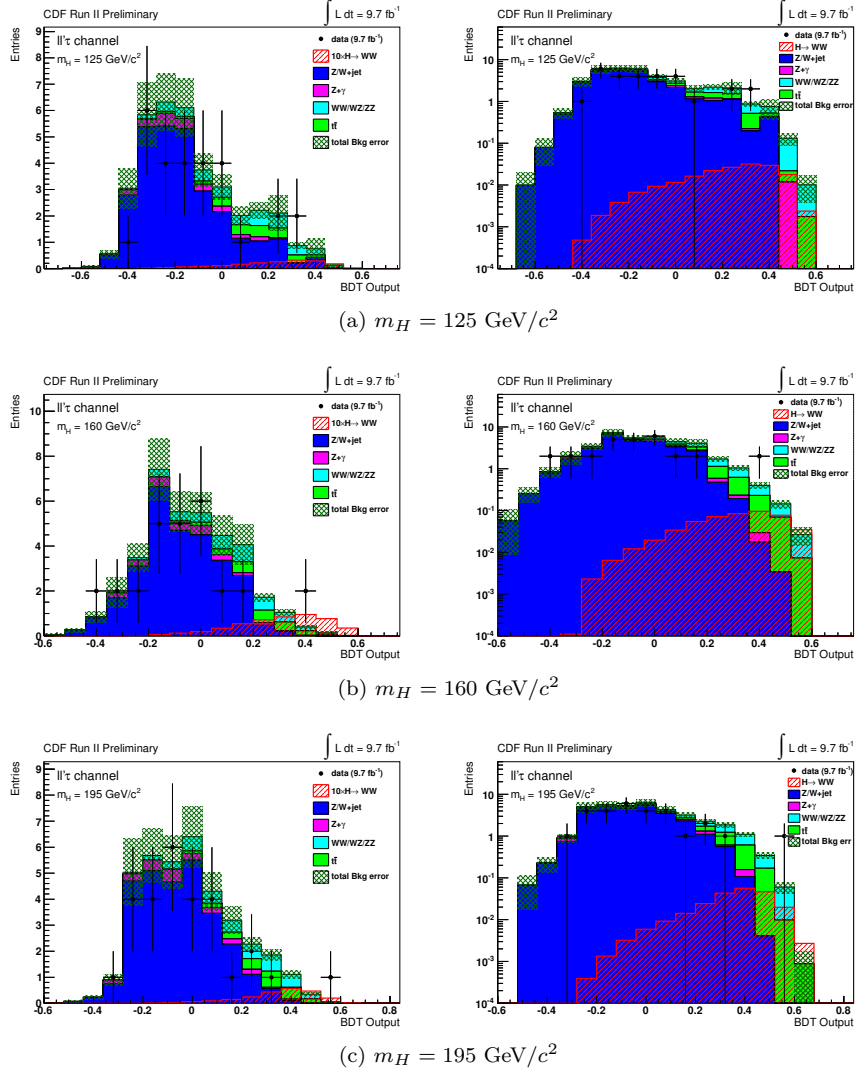


Figure 5.5: BDT output (left) and background rejection rate versus signal efficiency (right) for three representative Higgs mass hypotheses in the trilepton channel.

sample is then applied to the testing sample. In Fig. 5.5 are reported the comparison between the training and testing sub-samples (left) and the background rejection versus signal efficiency (right). A Kolmogorov-Smirnov test is performed and the agreement is good. We optimized the BDT training parameters for three different mass hypotheses for the Standard Model Higgs boson, namely $m_H = 125, 160, 195 \text{ GeV}/c^2$ and saw that the best results are obtained when considering 200 trees with maximum depth of 2 nodes and using the Gini index as separation method with the adaptive

Figure 5.6: Trilepton BDT templates for Higgs masses 125, 160 and 195 GeV/c^2 .

boosting algorithm with boosting parameter of 0.5. Due to the low statistics we suffered some overtraining which required a little pruning we thus used the *Const-Complexity* method to remove the statistical insignificant branches. We let the BDT algorithm to calculate for each boosting the best pruning strength, at the end of the pruning a validation of the sample is performed. The distribution plots are reported in Appendix A.

5.6 Systematic Uncertainties

Our Monte Carlo estimation of the background and signal contributions is affected by systematic uncertainties. The systematic uncertainties affect the normalization of the Monte Carlo samples (*rate* uncertainties) through the Eq. (5.4.1). The main sources of

systematics are reported in Tab. 5.5 and Tab. 5.6. The rate uncertainties are divided into three categories.

Cross Section Systematics The cross section calculation is used to normalize both signal and background Monte Carlo samples. Due to the perturbative nature of the theory, errors associated to the approximation are to be taken into account. The Parton Distribution Functions (PDF), used to calculate the cross section of hard scattering, have two main source of uncertainties, one arise from our limited knowledge of the partonic cross section; the other is our ignorance on the PDF itself.

Acceptance Systematics We group in this category all the sources of systematic uncertainties that vary the number of selected events either for the detector geometry or for the event selections applied;

Luminosity Uncertainties Accounts for the error on the luminosity measurement which affect the number of events predicted by the simulations.

Uncertainty source	WW	WZ	ZZ	tt	$Z+\text{jet}$	$W+\text{jet}$	$Z\gamma$
Cross section	6.0	6.0	6.0	10.0			5.0
Measured W cross-section						12.0	
Measured Z cross-section					9.7		
PDF Model	2.6	1.9	2.4	1.4	5.4	4.2	4.0
Higher order diagrams	10.0	10.0	10.0	10.0			11.0
Trigger Efficiency	2.0	2.0	2.0	2.0	2.0	2.0	2.0
Lepton ID Efficiency	3.1	3.1	3.1	3.1	3.1	3.1	3.1
τ ID Efficiency	1.3	2.1	1.8	1.1			1.4
Jet into τ Fake rate	4.2	4.5	4.2	5.1	6.6	6.4	0.07
Lepton into τ Fake rate	0.6	0.5	0.3	0.2	0.5	0.0	0.7
Luminosity	5.9	5.9	5.9	5.9	5.9	5.9	5.9
Total	14.5	14.6	14.5	16.7	14.7	15.8	13.9

Table 5.5: Systematic uncertainties on the background for the trilepton channel (expressed in %).

Source	$gg \rightarrow H$	WH	ZH	VBF
Cross Section	14.3	5.0	5.0	10.0
PDF Model	2.4	1.9	1.8	2.1
Higher order diagrams		10.0	10.0	10.0
Trigger Efficiency	2.0	2.0	2.0	2.0
Lepton ID Efficiency	3.1	3.1	3.1	3.1
τ ID Efficiency	0.1	1.4	1.6	0.07
Jet into τ Fake rate	0.6	3.5	2.9	3.8
Lepton into τ Fake rate	0.08	0.1	0.1	0.07
Luminosity	5.9	5.9	5.9	5.9
Total	16.1	13.8	13.7	16.3

Table 5.6: Systematic uncertainties on the signals in the trilepton channel (expressed in %).

5.7 Limit Calculation

Since no significant excess of the data over the expected background were observed, in the distribution of the BDT outputs, we use those distributions to set a 95% confidence level (C.L.) limit. We adopt a Bayesian method [12] and for each considered

Higgs boson mass hypothesis, a likelihood, \mathcal{L} , is built that is the product of Poisson probabilities of observing in the i -th bin of the input histogram n_i events, given an expectation of μ_i

$$\mathcal{L}(R|\vec{\theta}, \vec{n}) = \prod_i \frac{\mu_i^{n_i} e^{-\mu_i}}{n_i!} \cdot \prod_k e^{-\frac{\theta_k^2}{2}} \quad (5.7.1)$$

with

$$\mu_i = R \cdot s_i(\vec{\theta}) + b_i(\vec{\theta}), \quad (5.7.2)$$

written as the sum of the signal $s_i(\vec{\theta})$ and background $b_i(\vec{\theta})$ expectations. Since s_i can also be written as $s_i = L \cdot \epsilon \cdot \sigma_H^{SM}$, where L is the integrated luminosity, ϵ the detector acceptance and σ_H^{SM} is the Standard Model Higgs boson production cross section, R is a multiplicative factor on σ_H^{SM} . Each of the signal and background predictions depend on the parameters θ_k , called *nuisance parameters*. They are used to take into account systematic uncertainties

$$s_i(\vec{\theta}) = s_i \cdot \prod_k (1 + u_i^k \cdot \theta_k) \quad (5.7.3)$$

$$b_i(\vec{\theta}) = b_i \cdot \prod_k (1 + u_i^k \cdot \theta_k) \quad (5.7.4)$$

where u_i is the relative systematic error that is associated to the prediction s_i/b_i , since it depends on the index i , it is easy to implement uncertainties of all the histograms bins together (*rate systematics*) or independently on each bin (*shape systematics*). The index k allows to take into account different source of systematic uncertainties; the dependence on the indexes i and k makes it easy to combine results from different searches, when more than one histogram is used, the index i runs over each bin of each histogram. The Likelihood is integrated over each nuisance parameter $\vec{\theta}$ and evaluated for the observed number of events \vec{n} . The result, normalized to unit area, is the posterior $\mathcal{L}(R)$. The 95% upper limit R^{95} is then calculated solving the equation

$$\frac{\int_0^{R^{95}} \mathcal{L}(R) dR}{\int_0^{+\infty} \mathcal{L}(R) dR} = 0.95. \quad (5.7.5)$$

5.8 Results

We used the BDT output distributions (see Appendix A) to compute, with the method described in Sec. 5.7, a 95% confidence level limit on the production cross section on nineteen different Standard Model Higgs boson mass hypotheses. Tab. 5.7 report the expected in absence of signal limit (*median*) and the observed one. The same results are also graphically reported in Fig. 5.7, the $\pm\sigma$ and $\pm 2\sigma$ bands are also included where the median is allowed to fluctuate in absence of signal.

The maximum sensitivity is reached at $165 \text{ GeV}/c^2$ where the agreement between the expected limit (12.2) and the observed one (12.1) is good. The maximum sensitivity at $165 \text{ GeV}/c^2$ is what we expected for $H \rightarrow WW$ processes (see Fig. 1.3) as well as the loss of sensitivity for low masses ($m_H < 130 \text{ GeV}/c^2$) where the dominant process is $H \rightarrow b\bar{b}$.

Higgs Mass [GeV/c^2]	-2σ	-1σ	Median	$+1\sigma$	$+2\sigma$	Observed
110	108.8	137.2	193.2	268.1	360.67	156.0
115	61.3	77.6	106.4	151.2	203.6	120.1
120	37.8	46.9	65.0	95.5	135.4	53.7
125	25.0	31.5	43.9	63.4	88.1	38.8
130	18.0	21.5	29.2	40.8	59.4	24.4
135	13.9	17.0	23.0	32.0	46.3	18.8
140	11.2	14.1	19.4	27.4	37.4	16.7
145	10.1	12.4	17.0	24.7	33.2	13.5
150	10.6	12.9	17.2	23.9	34.4	14.6
155	9.2	11.7	15.6	21.6	40.0	15.5
160	7.9	9.4	12.4	17.5	23.9	12.6
165	7.7	9.3	12.2	16.9	23.6	12.1
170	8.3	10.0	13.3	18.6	26.7	14.0
175	9.4	11.6	15.4	21.7	31.1	13.9
180	10.3	12.6	17.2	24.1	32.3	14.6
185	12.4	15.6	21.2	30.3	43.7	19.0
190	15.1	18.4	24.2	34.6	49.1	24.1
195	17.0	20.7	27.8	39.5	56.0	26.7
200	19.5	24.4	32.2	46.1	67.3	25.7

Table 5.7: Observed and expected limits for the trilepton channel.

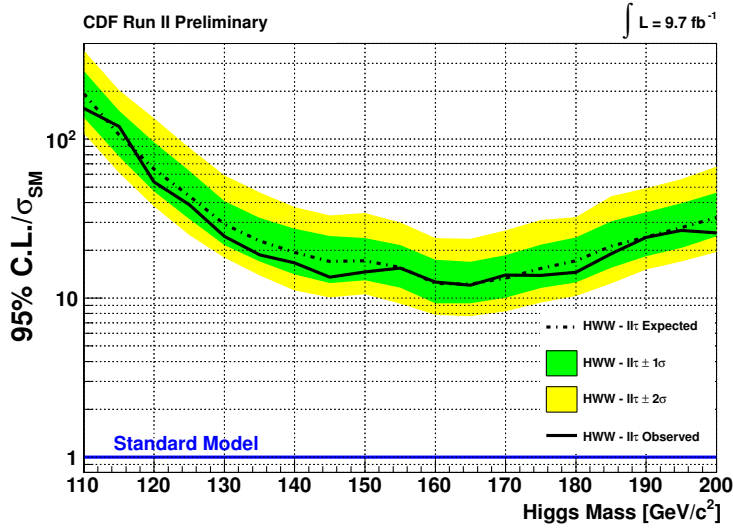


Figure 5.7: Observed and expected (median, for the background-only hypothesis) 95% C.L. upper limits on the ratios to the SM cross section, as functions of the Higgs boson mass. The limits are expressed as a multiple of the SM prediction for test masses (every $5 \text{ GeV}/c^2$). The points are joined by straight lines for better readability. The bands indicate the 68% and 95% probability regions where the limits can fluctuate, in the absence of signal.

Chapter 6

Conclusions

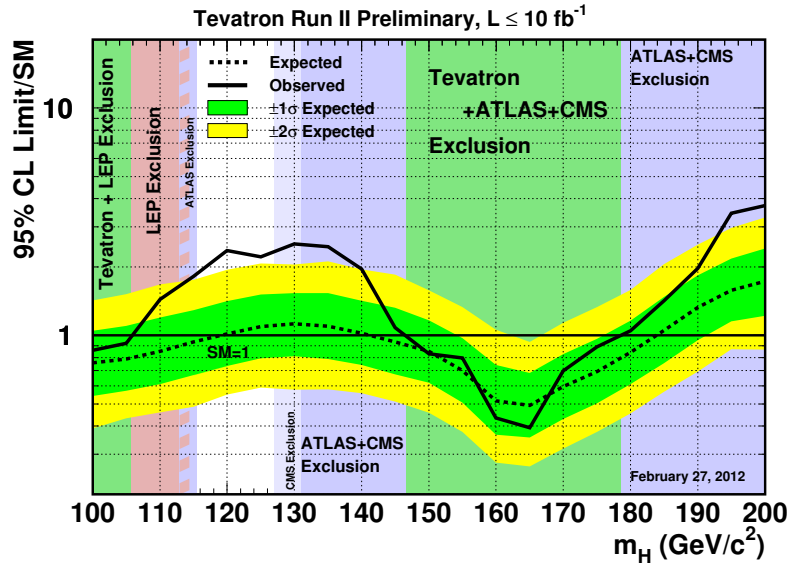


Figure 6.1: CDF and DØ combined limit.

2012 will likely be a crucial year in the quest for the Higgs boson, which has represented one of the main topics in the Elementary Particle field for over forty years. The Tevatron final dataset is being analyzed and the Large Hadron Collider is going to deliver four times more data. In this context, the search reported in this thesis has explored for the first time the experimental signature with two leptons and one hadronic tau in the final state. The interest for this signature arise because no single channel has the sensitivity to probe the Standard Model Higgs boson by itself and the strategy adopted by the CDF collaboration is to explore all possible channels and then combine the results.

The search was carried on the full CDF Run II dataset of 9.7 fb^{-1} , we modeled our background samples, mainly composed of *dibosons events* (WW , WZ , ZZ), $Z/W + jets$, $Z + \gamma$ and $t\bar{t}$, using a Monte Carlo calculation of the $p\bar{p}$ collisions followed by a complete simulation of the CDF II detector response. The reliability of our Monte

Carlo predictions is tested in two control samples, dominated by the same processes which represent backgrounds for our search. In the final sample we expect 40 ± 5.4 background events and 0.54 ± 0.05 signal events for a Higgs mass hypothesis of $160 \text{ GeV}/c^2$ whereas in data we observe 28 events.

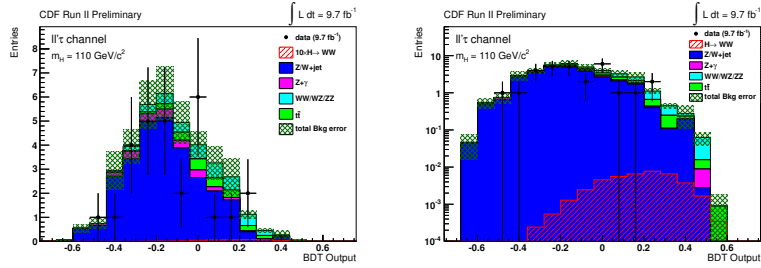
We exploited a boosted decision tree, to discriminate the signal from the background and found no statistically significant excess in the distributions of the BDT output. We thus used a Bayesian method to set a 95% confidence level limit on the Standard Model Higgs boson production cross section which, for a Higgs boson mass hypothesis of $160 \text{ GeV}/c^2$, is 12.6. The expected 95% confidence level upper limit for the same mass is 12.4. We also presented the limit calculations for other nineteen mass hypotheses in the range between $110 \text{ GeV}/c^2$ and $200 \text{ GeV}/c^2$.

Our analysis was included in the final CDF and DØ combination, Fig. 6.1 shows the 95% C.L. expected and observed limit for the nineteen mass hypotheses considered. The search excludes the existence of a Standard Model Higgs boson with mass $147 < m_H < 179 \text{ GeV}/c^2$ and $100 < m_H < 106 \text{ GeV}/c^2$ at 95% C.L. An excess with a significance of 2.2σ is seen that might be interpreted as coming from a Higgs boson with a mass in the region of $115 < m_H < 135 \text{ GeV}/c^2$.

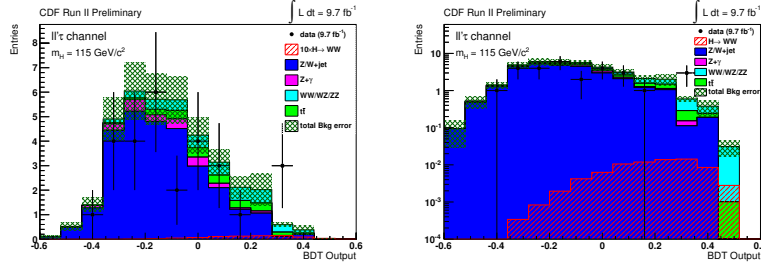
Our analysis contributed to the overall result for the 0.3%, 1% and 3% for a Standard Model Higgs boson mass hypothesis of 125, 160 and $190 \text{ GeV}/c^2$ respectively.

Appendix A

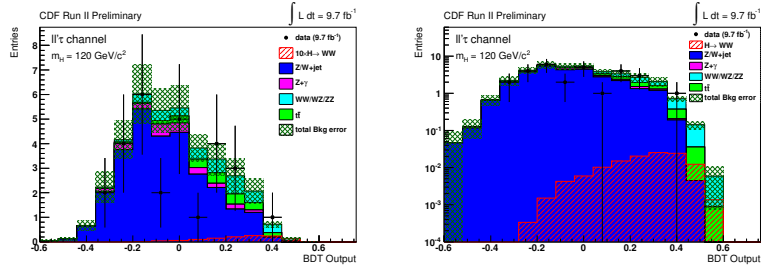
BDT Distribution Plots



(a) $m_H = 110 \text{ GeV}/c^2$

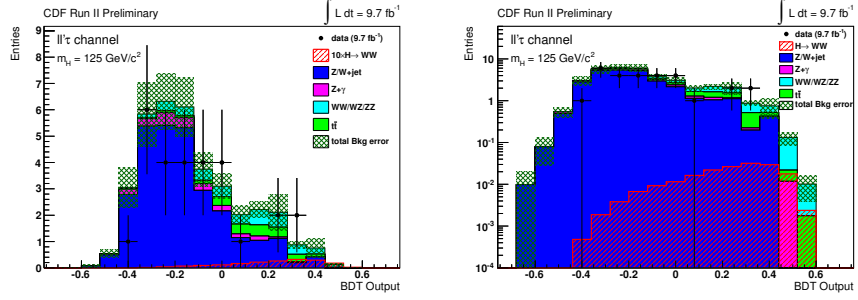


(b) $m_H = 115 \text{ GeV}/c^2$

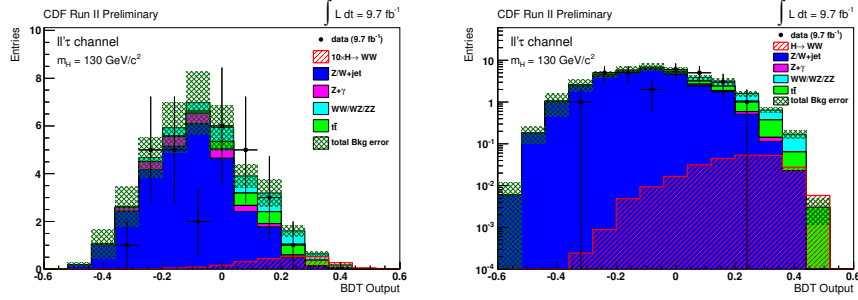


(c) $m_H = 120 \text{ GeV}/c^2$

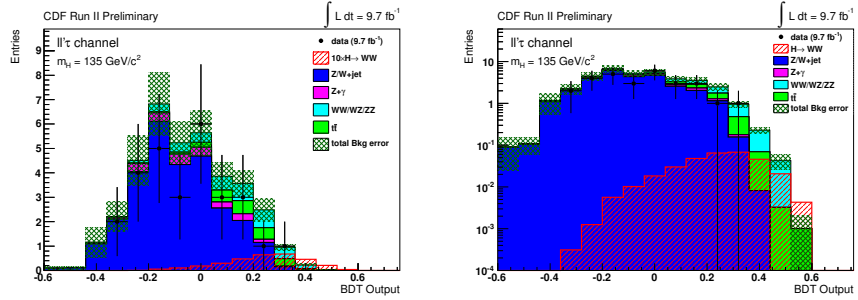
Figure A.1: Trilepton BDT templates for Higgs masses 110, 115 and 120 GeV/c^2 .



(a) $m_H = 125 \text{ GeV}/c^2$

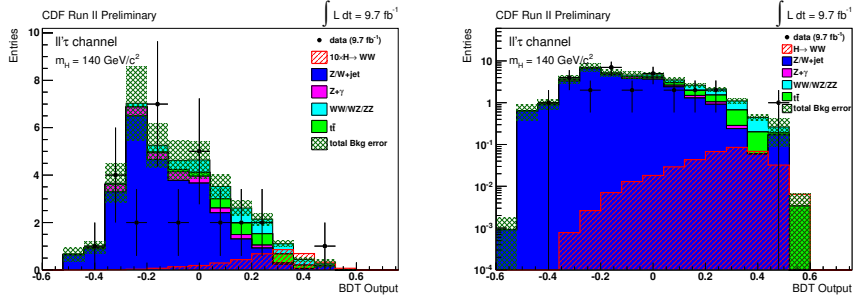


(b) $m_H = 130 \text{ GeV}/c^2$

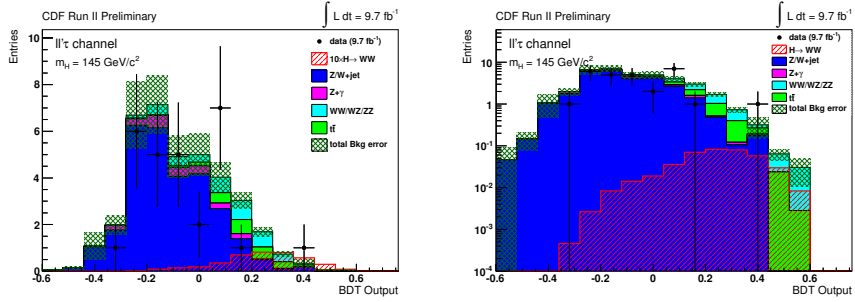


(c) $m_H = 135 \text{ GeV}/c^2$

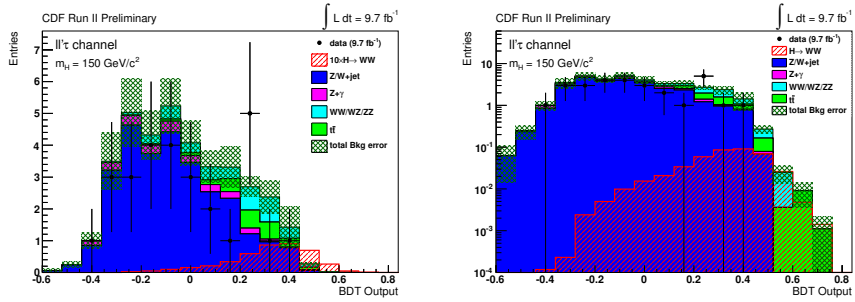
Figure A.2: Trilepton BDT templates for Higgs masses 125, 130 and 135 GeV/c^2 .



(a) $m_H = 140 \text{ GeV}/c^2$

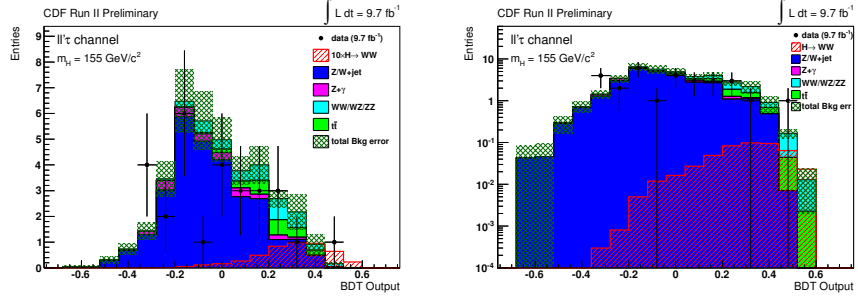


(b) $m_H = 145 \text{ GeV}/c^2$

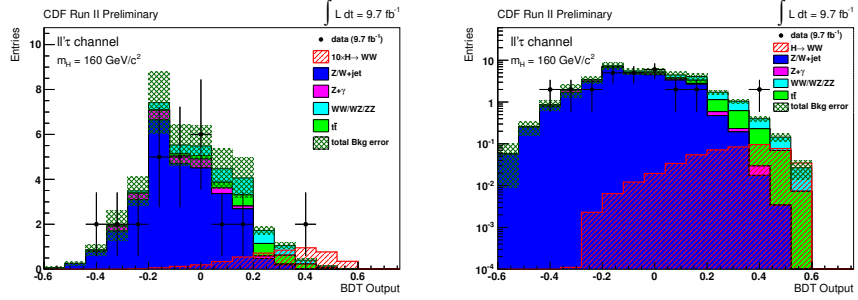


(c) $m_H = 150 \text{ GeV}/c^2$

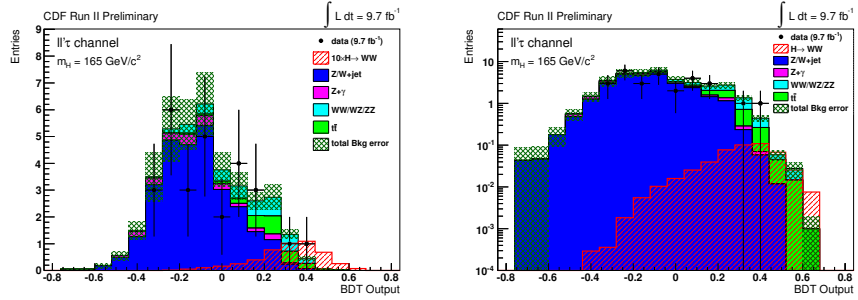
Figure A.3: Trilepton BDT templates for Higgs masses 140, 145 and 150 GeV/c^2 .



(a) $m_H = 155 \text{ GeV}/c^2$

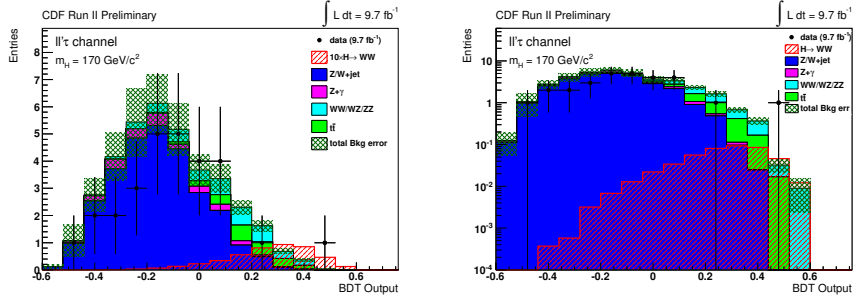


(b) $m_H = 160 \text{ GeV}/c^2$

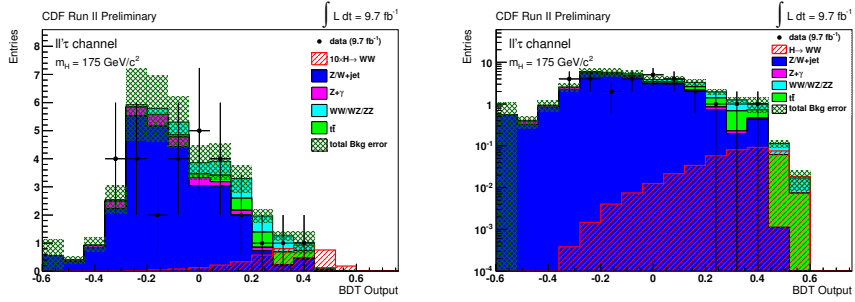


(c) $m_H = 165 \text{ GeV}/c^2$

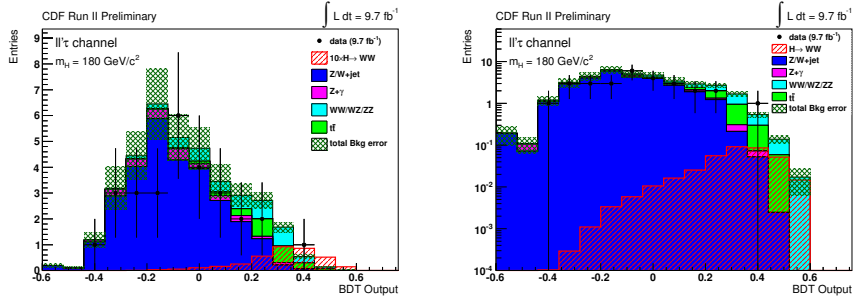
Figure A.4: Trilepton BDT templates for Higgs masses 155, 160 and 165 GeV/c^2 .



(a) $m_H = 170 \text{ GeV}/c^2$

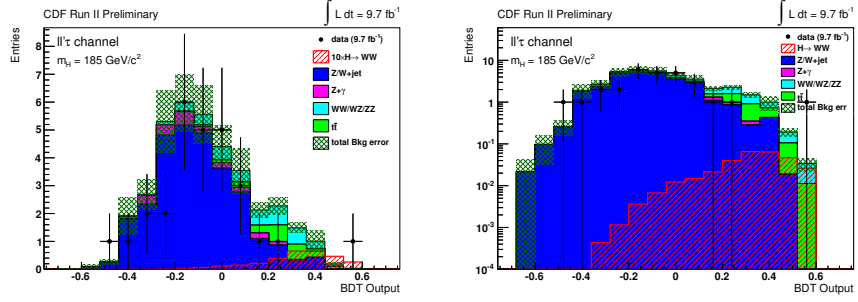


(b) $m_H = 175 \text{ GeV}/c^2$

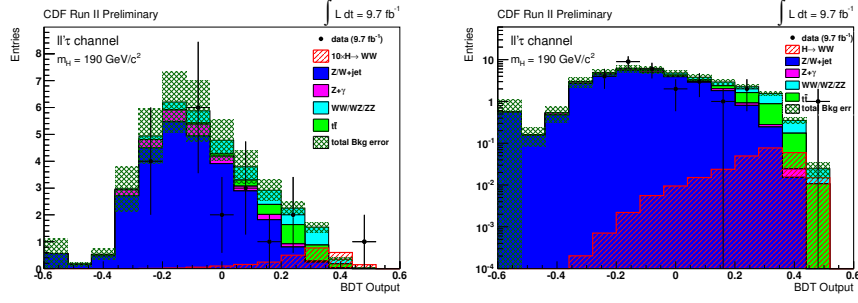


(c) $m_H = 180 \text{ GeV}/c^2$

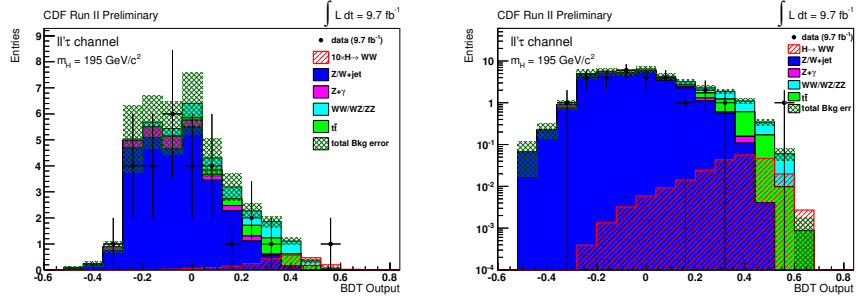
Figure A.5: Tripleton BDT templates for Higgs masses 170, 175 and 180 GeV/c^2 .



(a) $m_H = 185 \text{ GeV}/c^2$

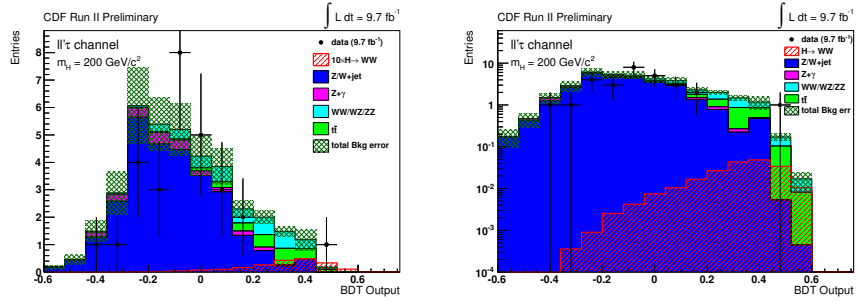


(b) $m_H = 190 \text{ GeV}/c^2$



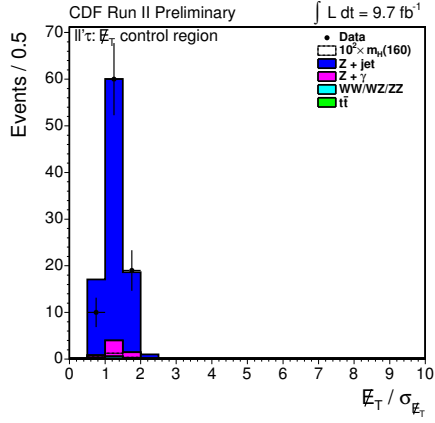
(c) $m_H = 195 \text{ GeV}/c^2$

Figure A.6: Tripleton BDT templates for Higgs masses 185, 190 and 195 GeV/c^2 .

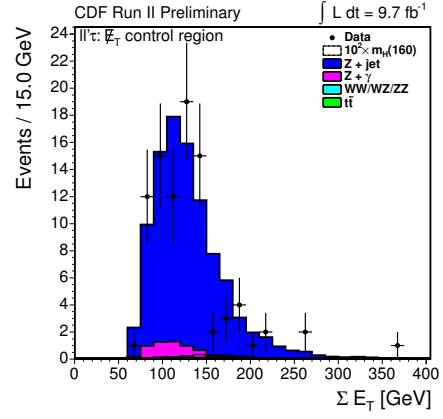


(a) $m_H = 200 \text{ GeV}/c^2$

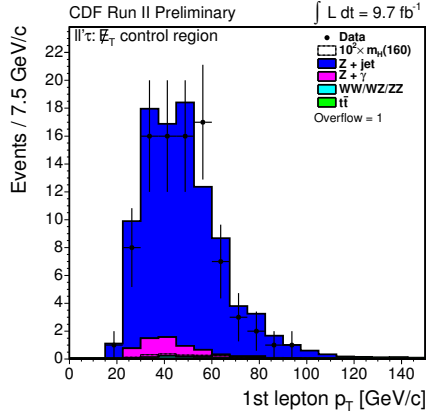
Figure A.7: Tripleton BDT template for the Higgs mass 200 GeV/c^2 .



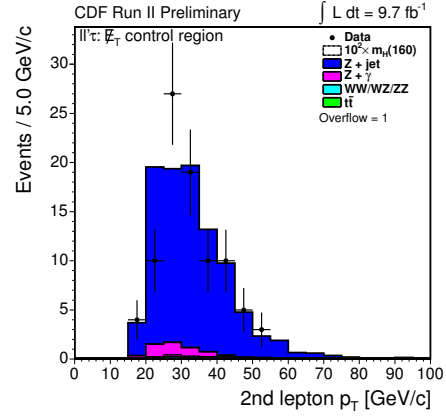
(a) Missing energy significance.



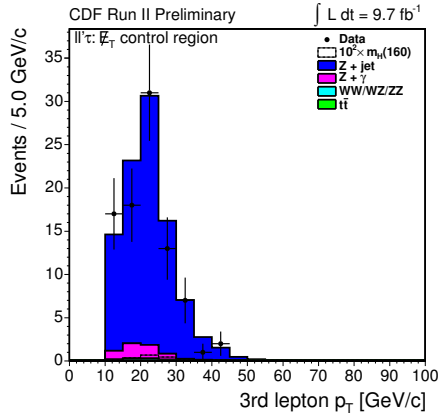
(b) E_T sum of all the reconstructed objects in the event.



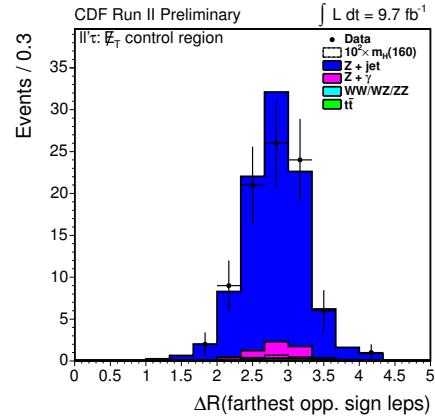
(c) Transverse momentum of the leading lepton.



(d) Transverse momentum of the sub-leading lepton.



(e) Transverse momentum of the least energetic lepton.



(f) ΔR between the farthest opposite-signed leptons.

Figure B.2: Data-MC comparison in the triplepton MET control region.

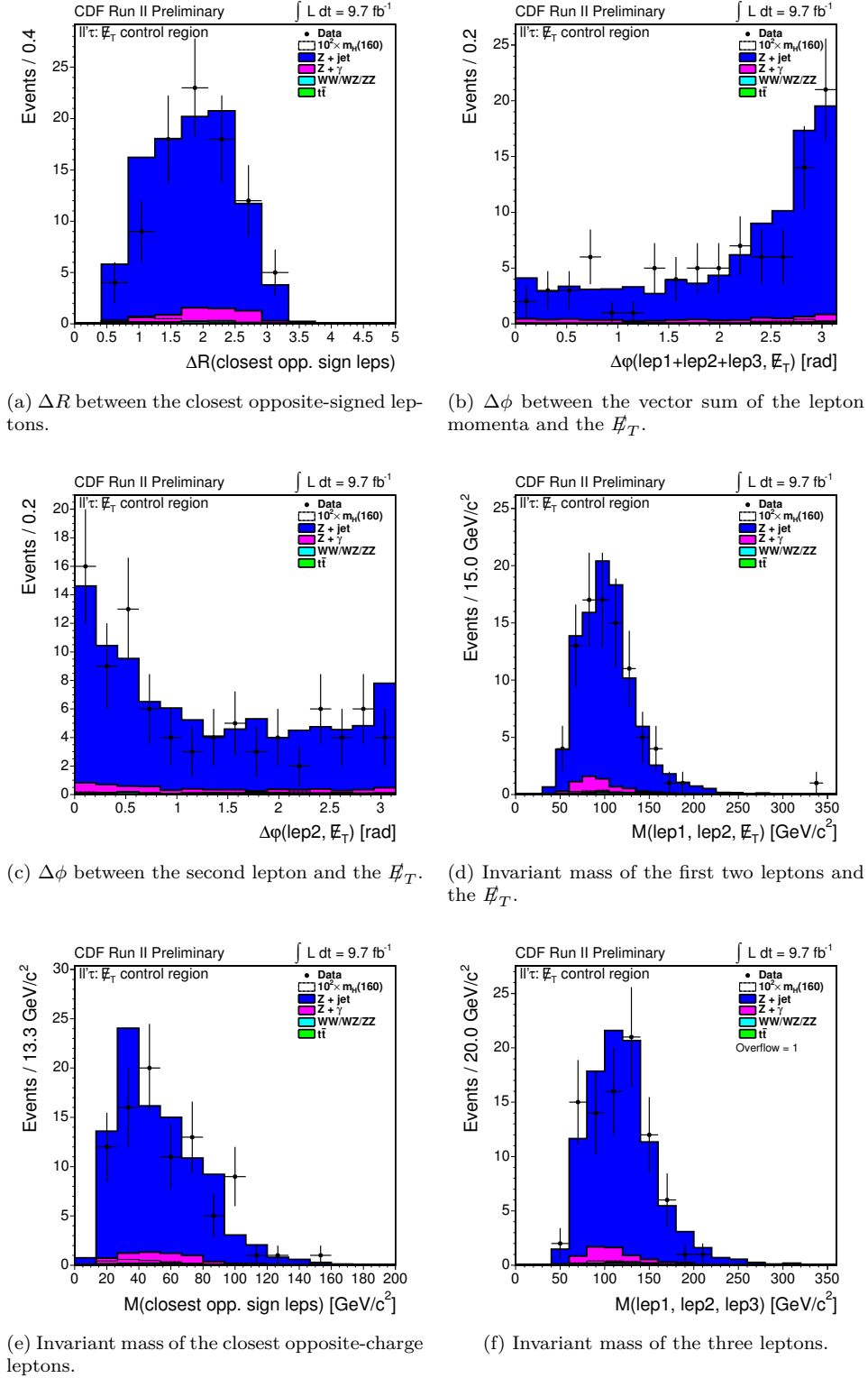
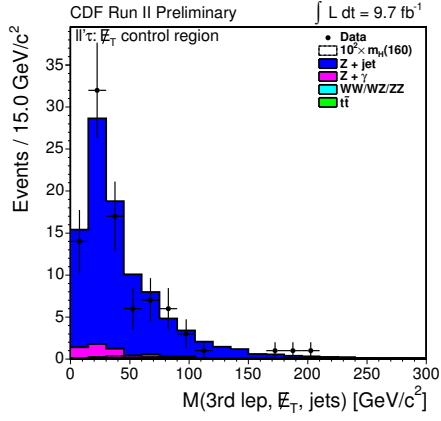
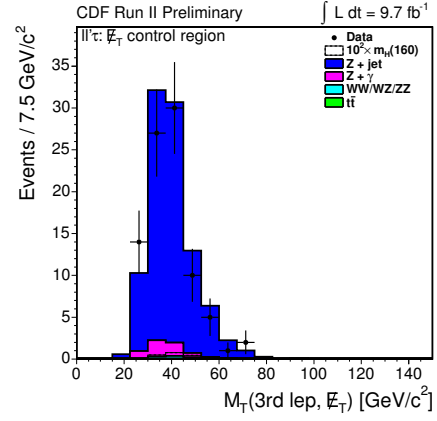


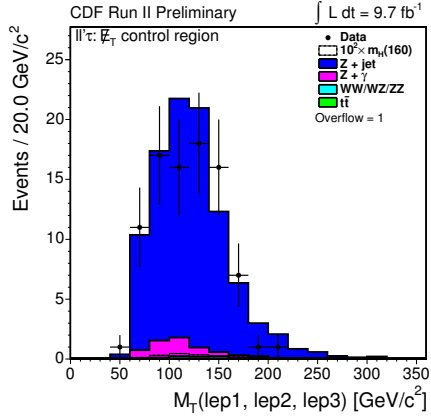
Figure B.3: Data-MC comparison in the trilepton MET control region.



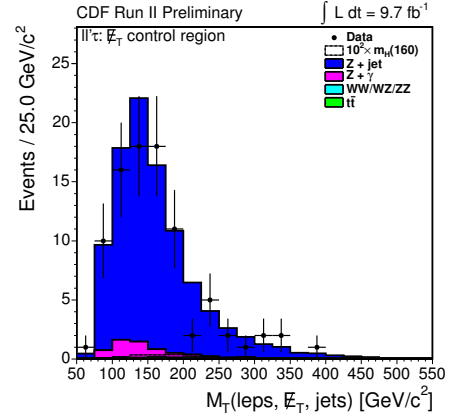
(a) Invariant mass of the third lepton, the E_T and the jets.



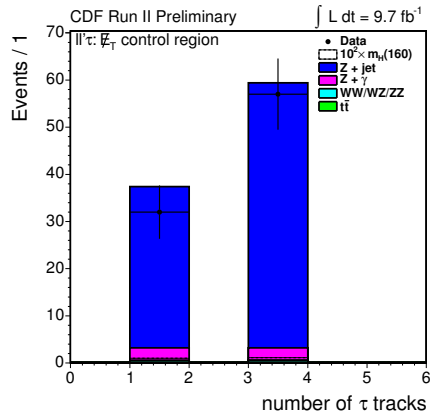
(b) Transverse mass of the third lepton and the E_T .



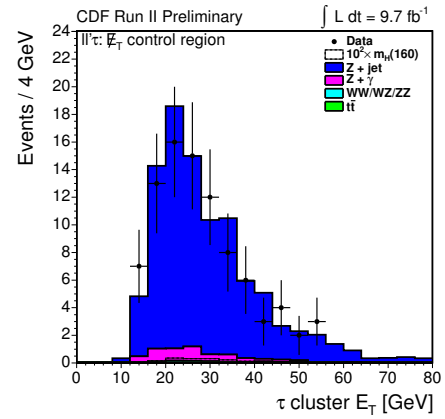
(c) Transverse mass of the three leptons.



(d) Transverse mass of the three leptons, the E_T and the jets.

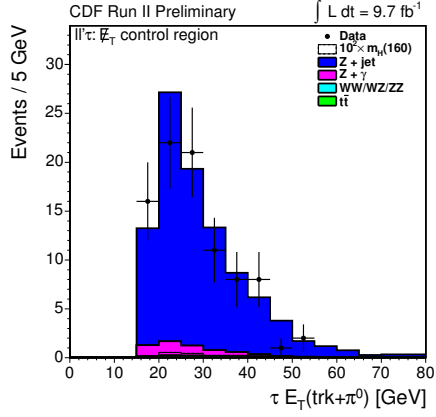


(e) Number of tracks of the reconstructed τ .

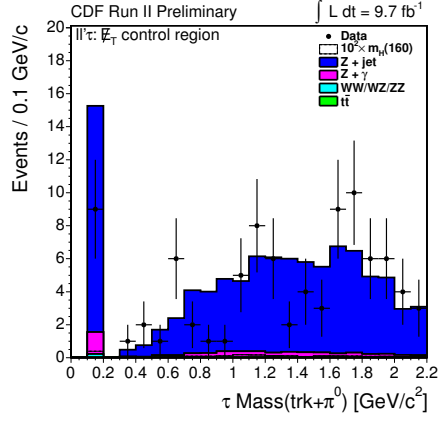


(f) Transverse energy of the τ calorimetric cluster.

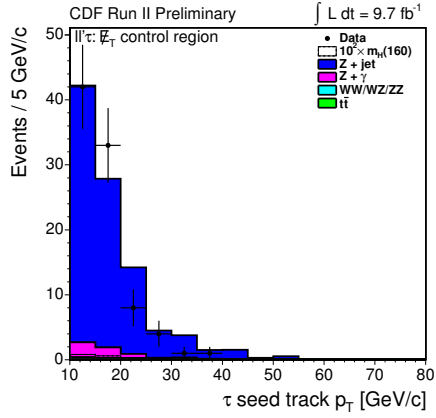
Figure B.4: Data-MC comparison in the trilepton MET control region.



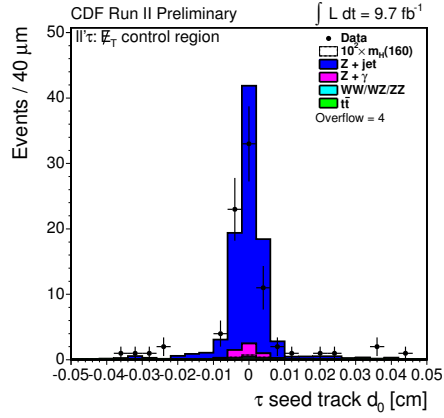
(a) Transverse energy of tracks and π^0 's in the τ signal cone.



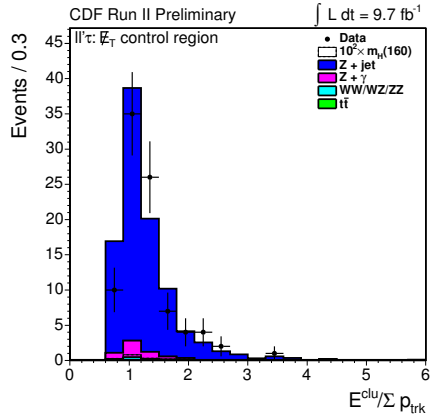
(b) Mass of tracks and π^0 's in the τ signal cone.



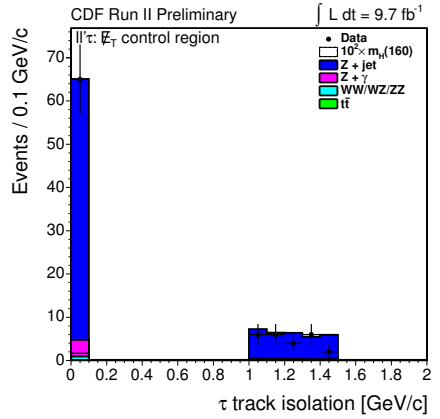
(c) Transverse momentum of the τ seed track.



(d) Impact parameter of the τ seed track.

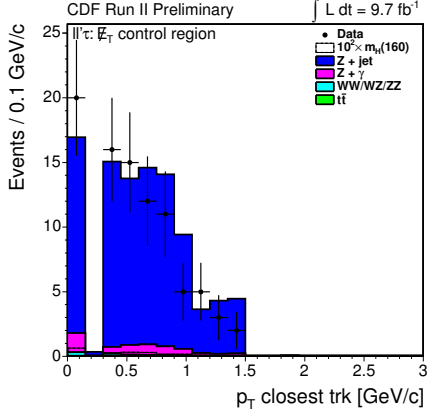


(e) Ratio of the τ cluster energy to the total momentum of the tracks associated to the τ .

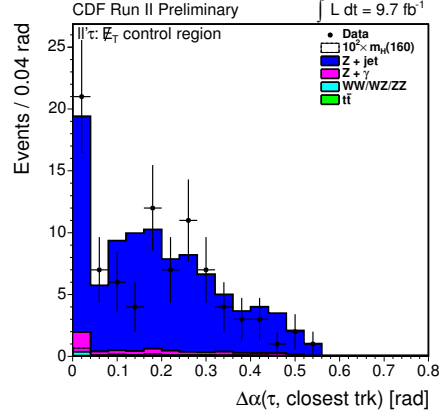


(f) τ track isolation.

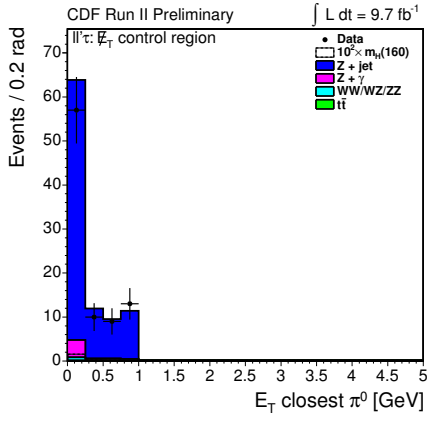
Figure B.5: Data-MC comparison in the trilepton MET control region.



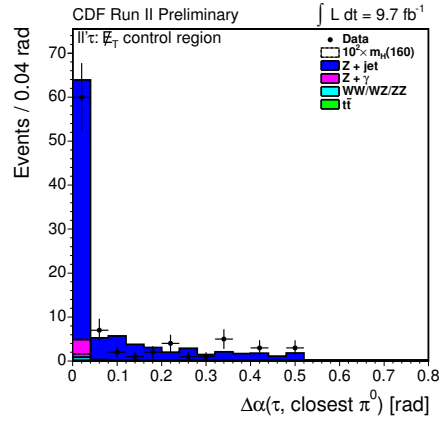
(a) p_T of the closest track to the τ .



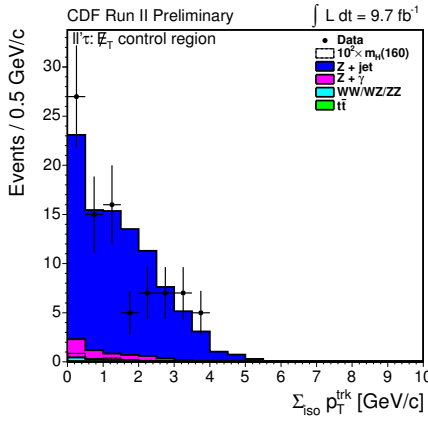
(b) Angle between the τ and the closest track.



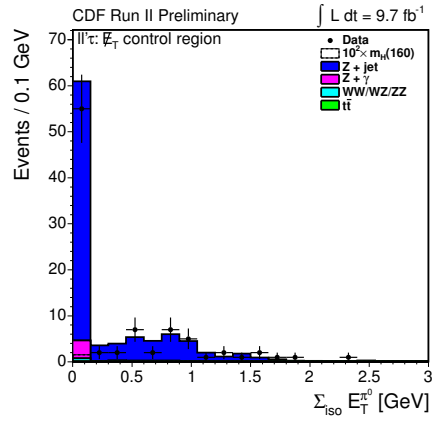
(c) E_T of the closest π^0 to the τ .



(d) Angle between the τ and the closest π^0 .

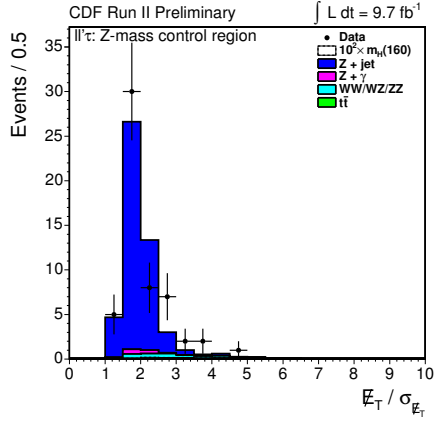


(e) Sum of p_T of all tracks in the τ isolation cone.

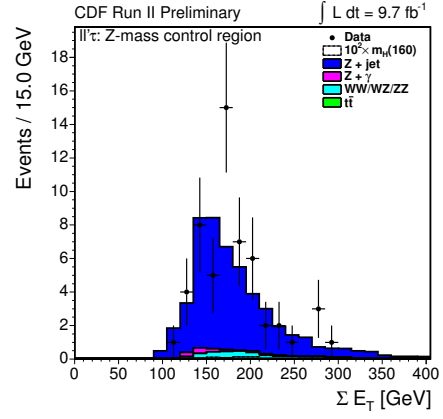


(f) Sum of E_T of all π^0 's in the τ isolation cone.

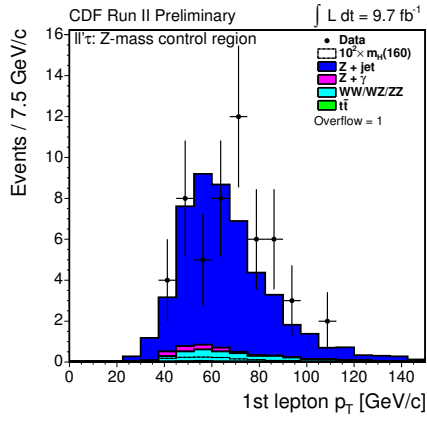
Figure B.6: Data-MC comparison in the tripleton MET control region.



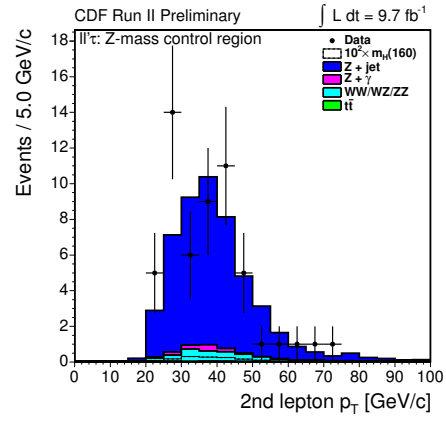
(a) Missing energy significance.



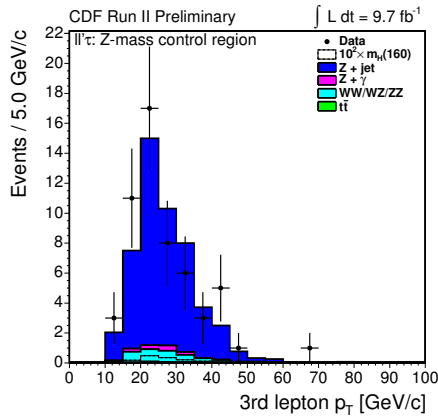
(b) E_T sum of all the reconstructed objects in the event.



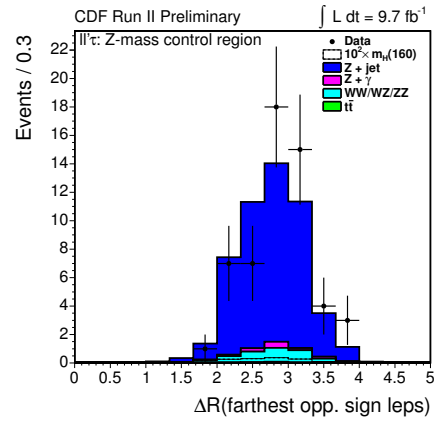
(c) Transverse momentum of the leading lepton.



(d) Transverse momentum of the sub-leading lepton.



(e) Transverse momentum of the least energetic lepton.



(f) ΔR between the farthest opposite-signed leptons.

Figure B.8: Data-MC comparison in the tripleton Z -mass control region.

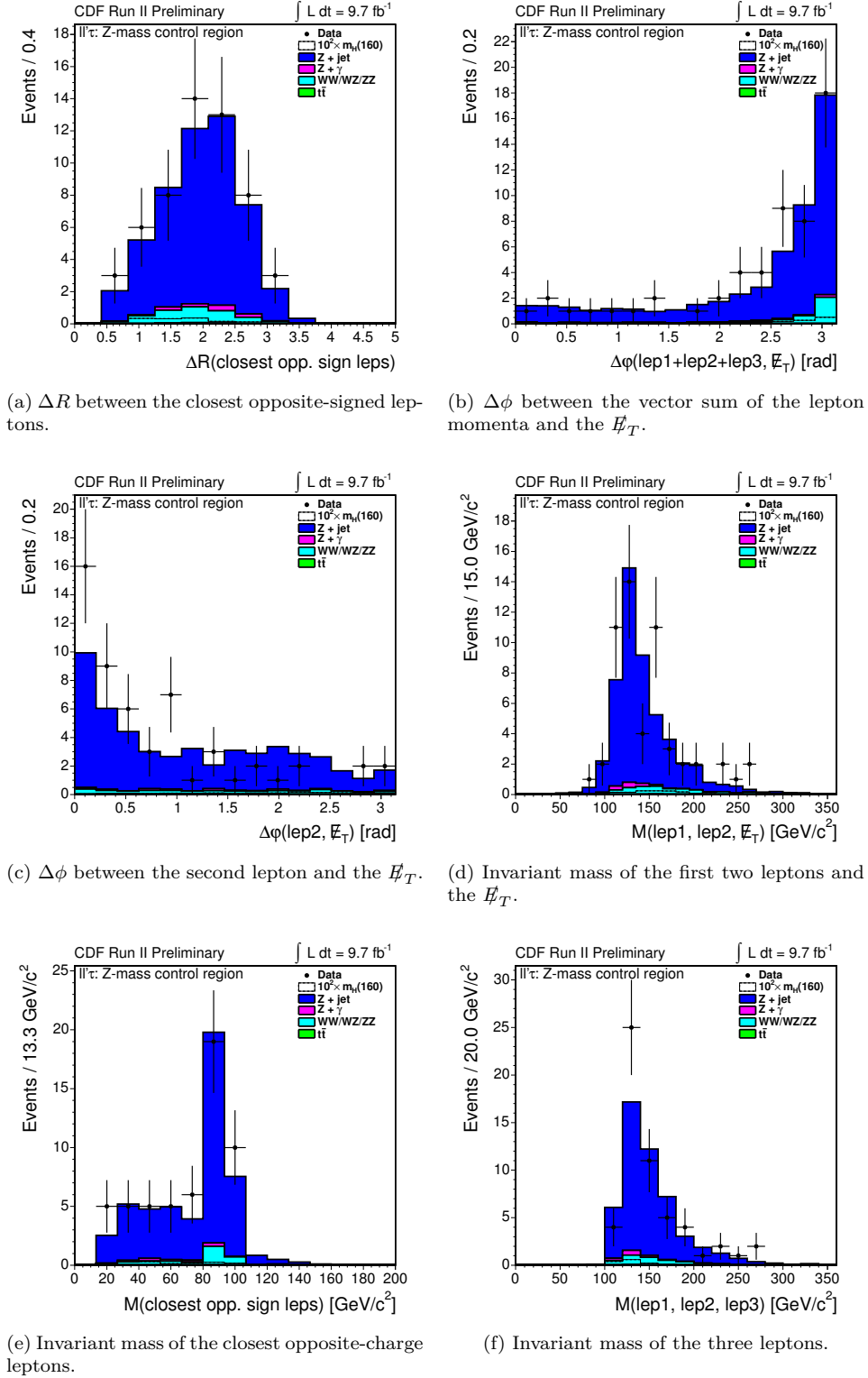
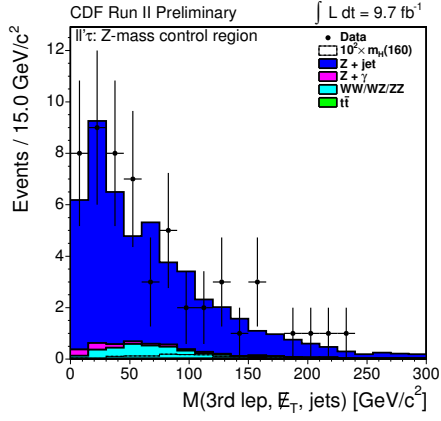
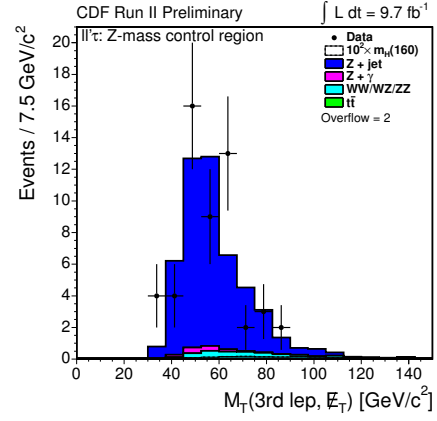


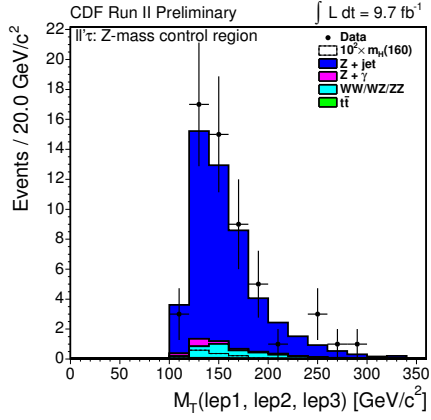
Figure B.9: Data-MC comparison in the trilepton Z-mass control region.



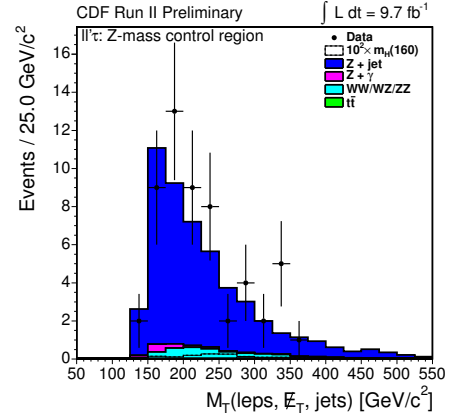
(a) Invariant mass of the third lepton, the E_T and the jets.



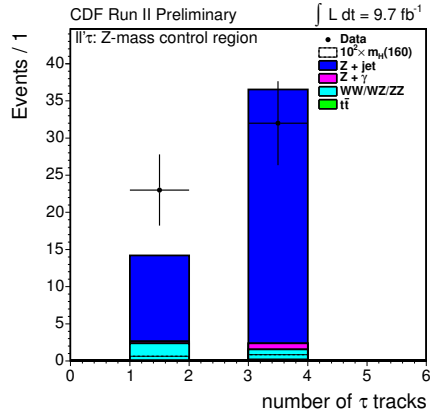
(b) Transverse mass of the third lepton and the E_T .



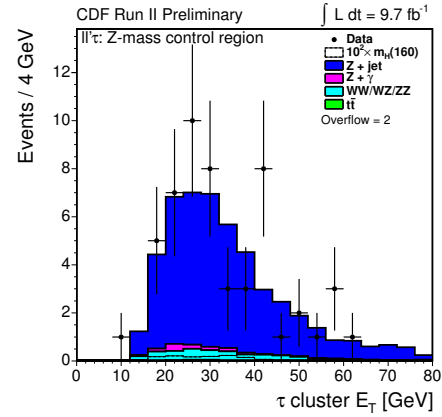
(c) Transverse mass of the three leptons.



(d) Transverse mass of the three leptons, the E_T and the jets.

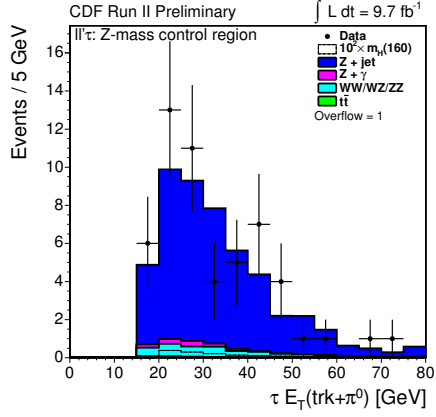


(e) Number of tracks of the reconstructed τ .

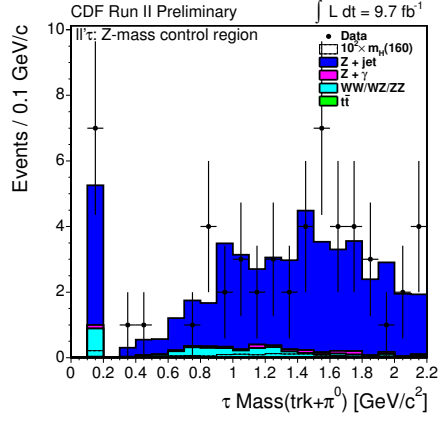


(f) Transverse energy of the τ calorimetric cluster.

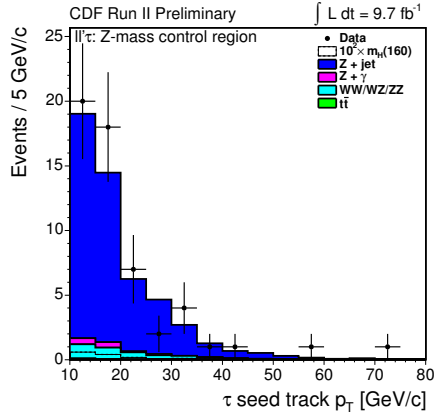
Figure B.10: Data-MC comparison in the trilepton Z-mass control region.



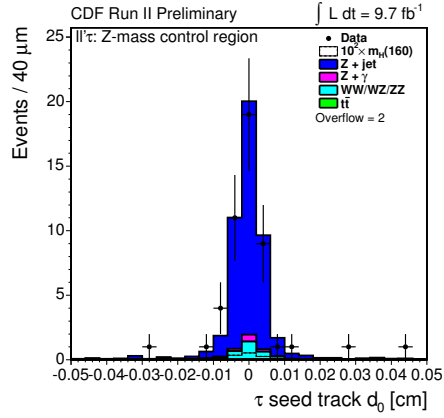
(a) Transverse energy of tracks and π^0 's in the τ signal cone.



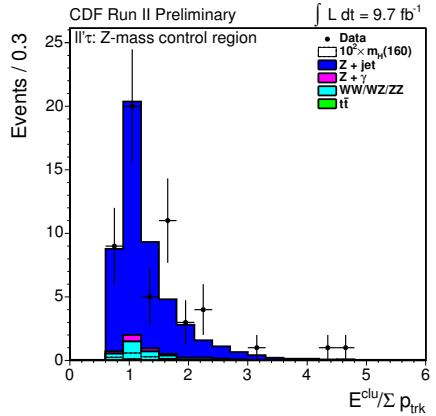
(b) Mass of tracks and π^0 's in the τ signal cone.



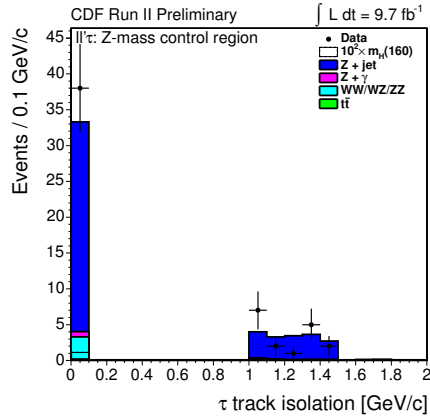
(c) Transverse momentum of the τ seed track.



(d) Impact parameter of the τ seed track.

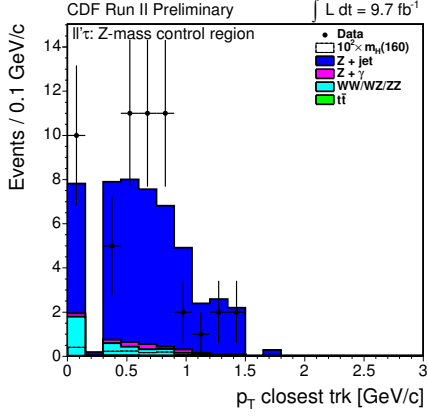


(e) Ratio of the τ cluster energy to the total momentum of the tracks associated to the τ .

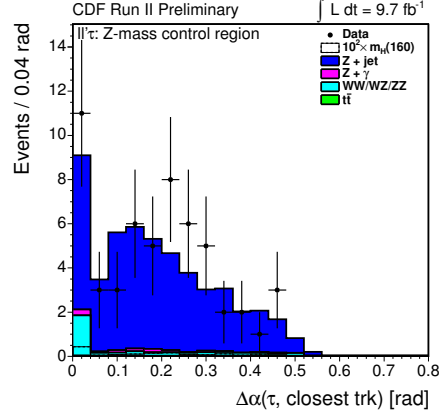


(f) τ track isolation.

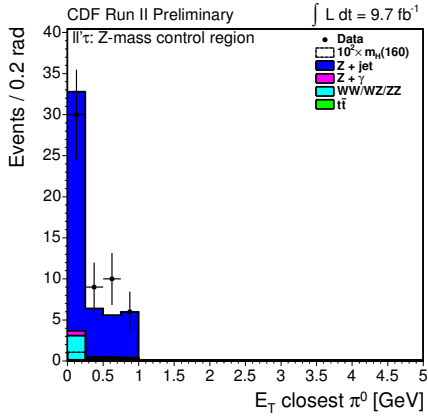
Figure B.11: Data-MC comparison in the triplepton Z-mass control region.



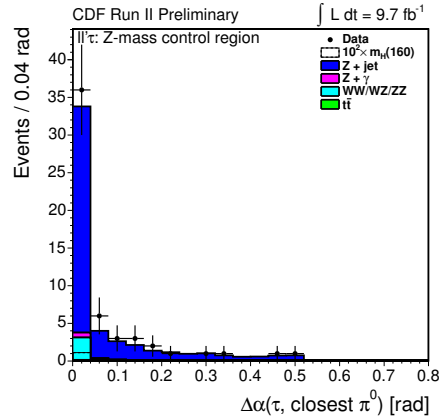
(a) p_T of the closest track to the τ .



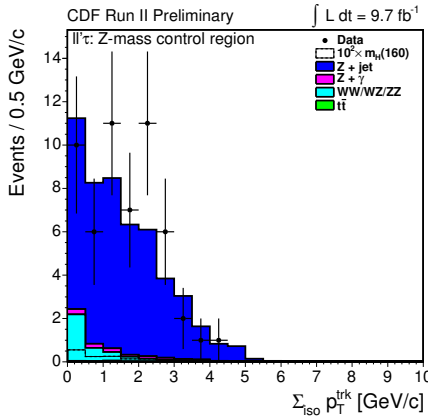
(b) Angle between the τ and the closest track.



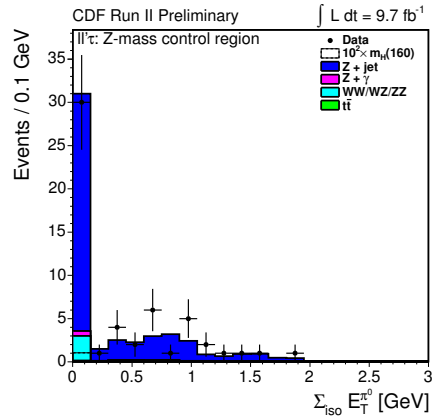
(c) E_T of the closest π^0 to the τ .



(d) Angle between the τ and the closest π^0 .

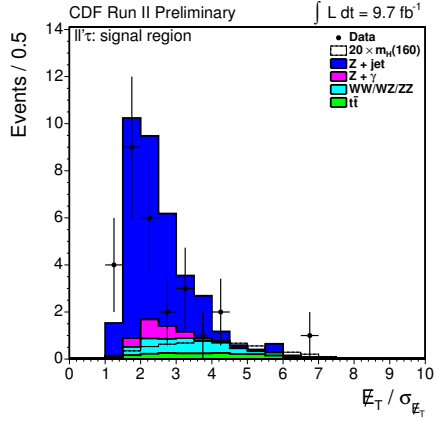


(e) Sum of p_T of all tracks in the τ isolation cone.

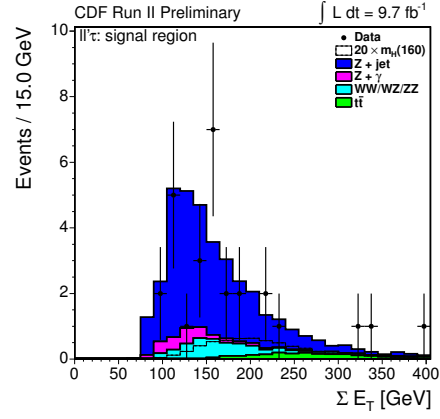


(f) Sum of E_T of all π^0 's in the τ isolation cone.

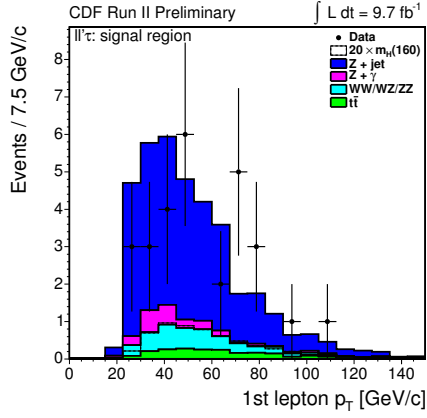
Figure B.12: Data-MC comparison in the trilepton Z -mass control region.



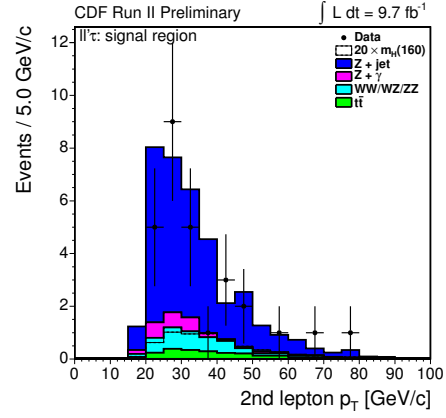
(a) Missing energy significance.



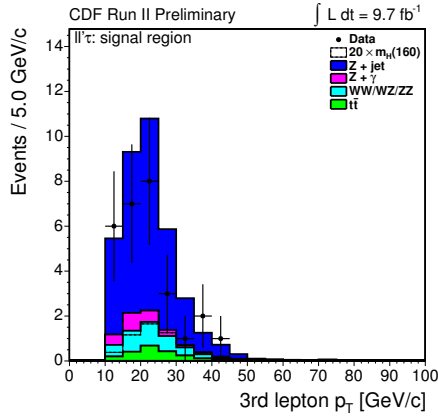
(b) E_T sum of all the reconstructed objects in the event.



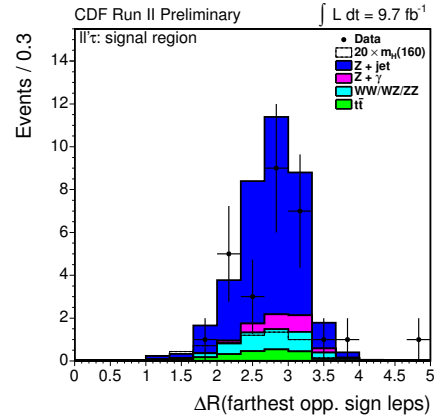
(c) Transverse momentum of the leading lepton.



(d) Transverse momentum of the sub-leading lepton.



(e) Transverse momentum of the least energetic lepton.



(f) ΔR between the farthest opposite-signed leptons.

Figure B.14: Data-MC comparison in the trilepton signal region.

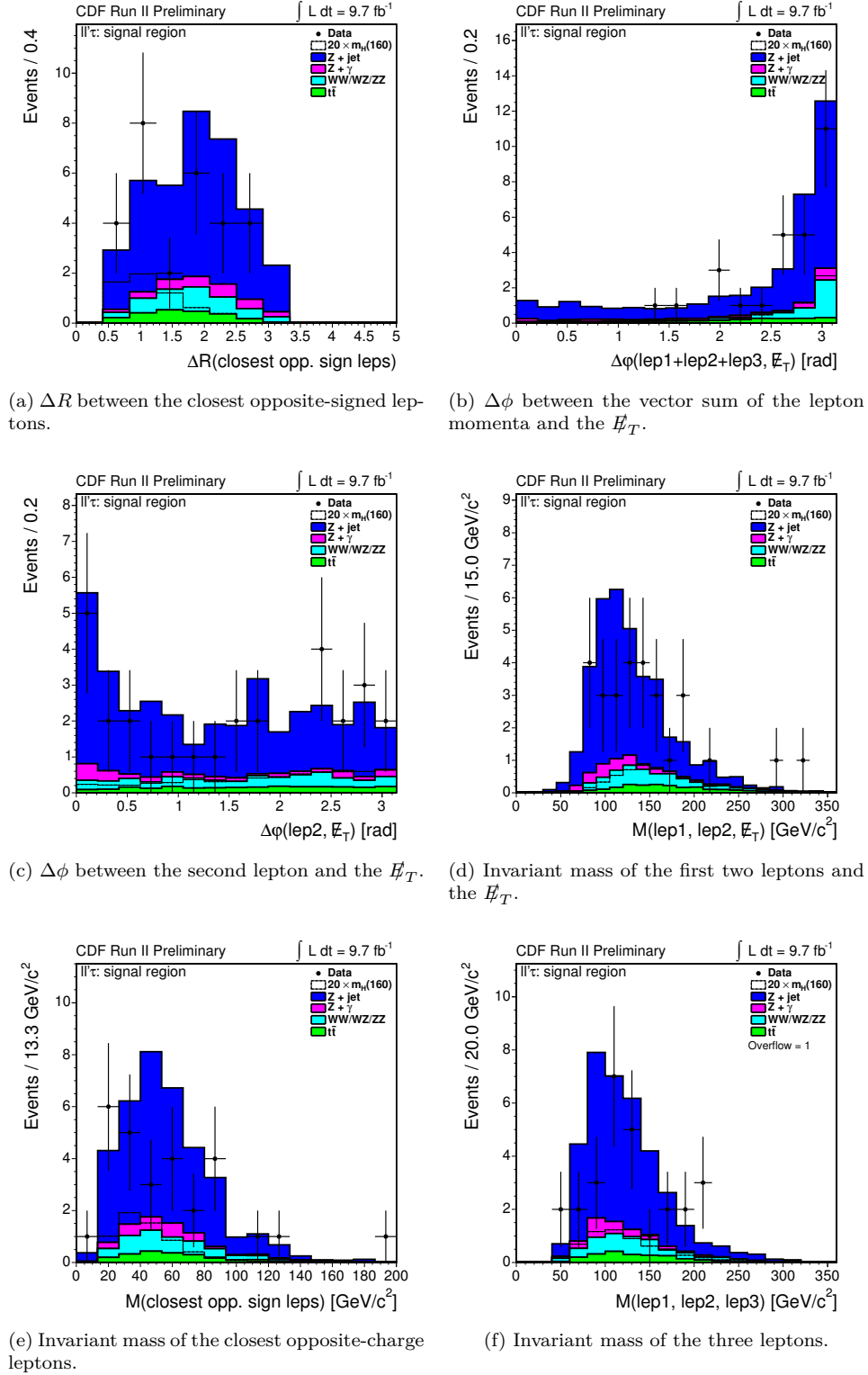
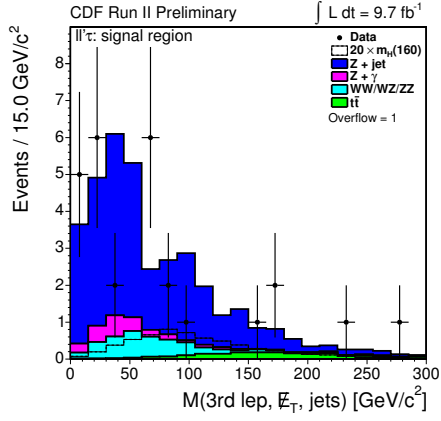
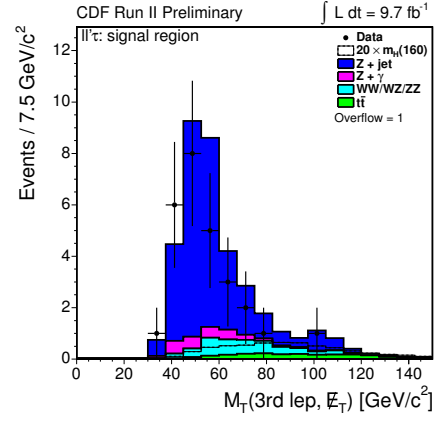


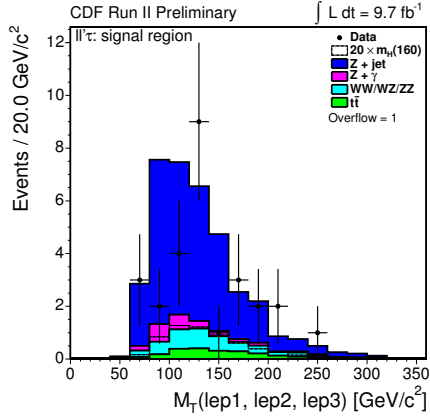
Figure B.15: Data-MC comparison in the trilepton signal region.



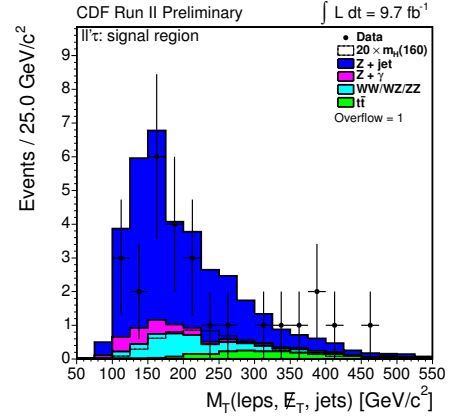
(a) Invariant mass of the third lepton, the E_T and the jets.



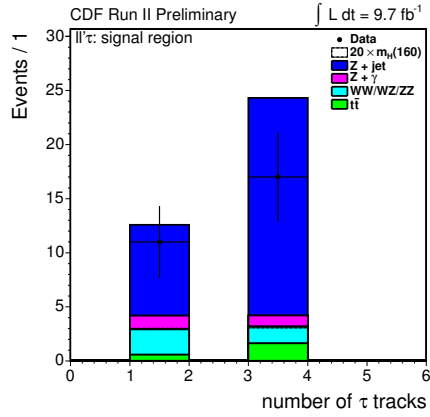
(b) Transverse mass of the third lepton and the E_T .



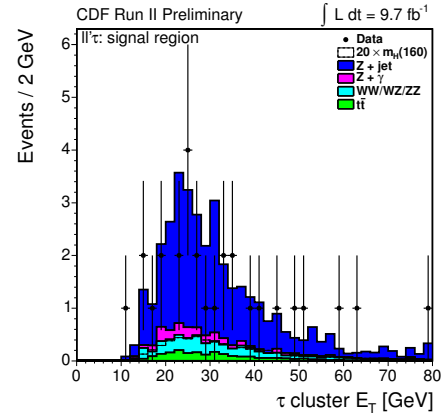
(c) Transverse mass of the three leptons.



(d) Transverse mass of the three leptons, the E_T and the jets.

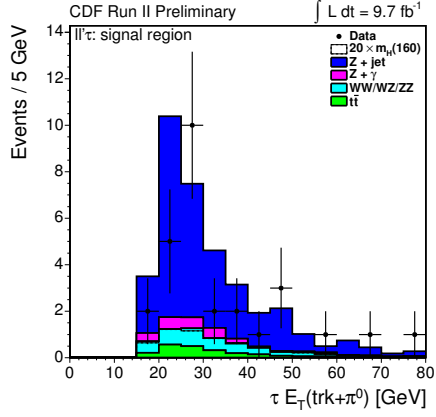


(e) Number of tracks of the reconstructed τ .

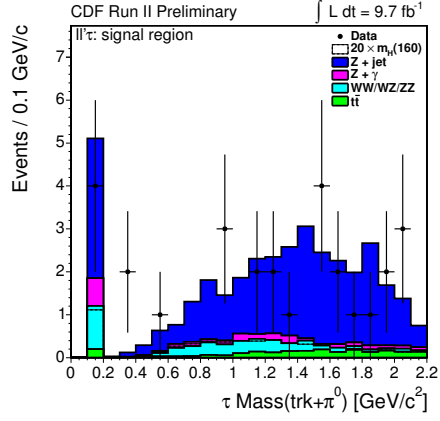


(f) Transverse energy of the τ calorimetric cluster.

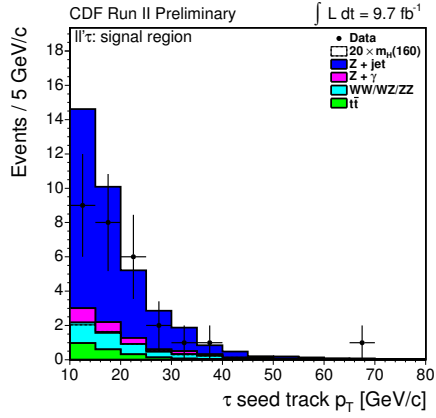
Figure B.16: Data-MC comparison in the tripleton signal region.



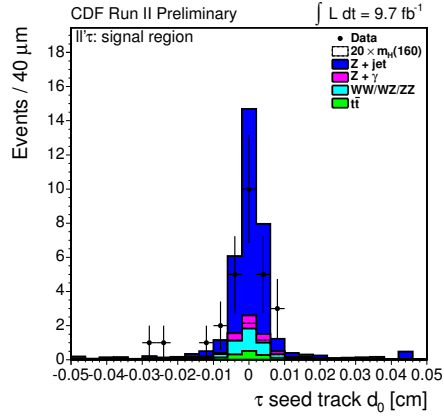
(a) Transverse energy of tracks and π^0 's in the τ signal cone.



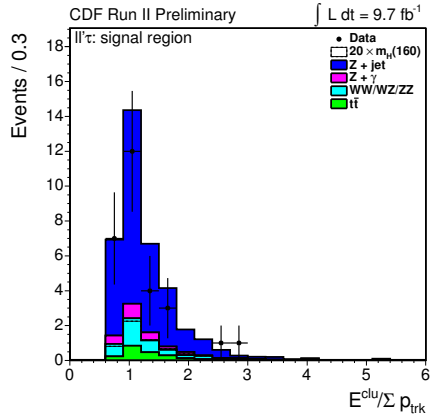
(b) Mass of tracks and π^0 's in the τ signal cone.



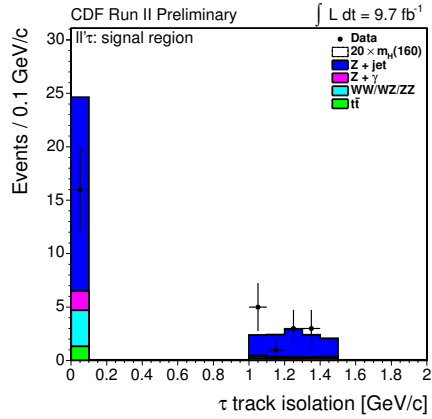
(c) Transverse momentum of the τ seed track.



(d) Impact parameter of the τ seed track.

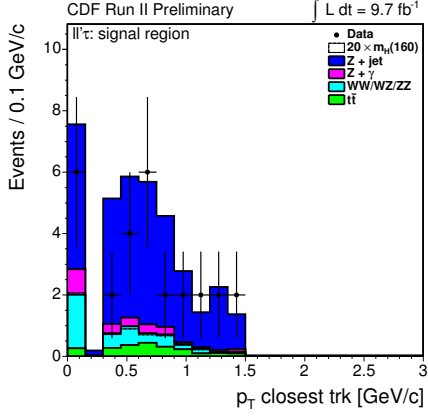


(e) Ratio of the τ cluster energy to the total momentum of the tracks associated to the τ .

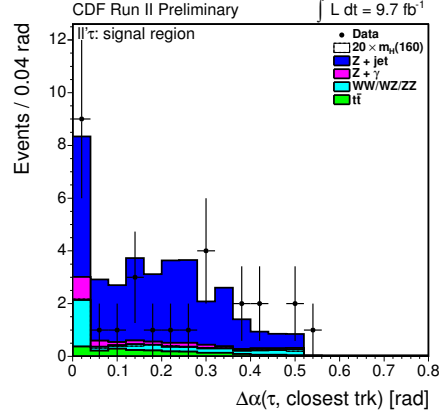


(f) τ track isolation.

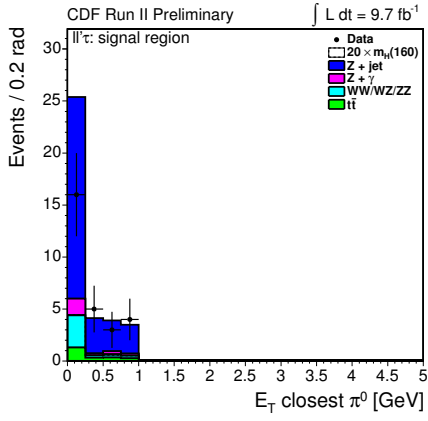
Figure B.17: Data-MC comparison in the trilepton signal region.



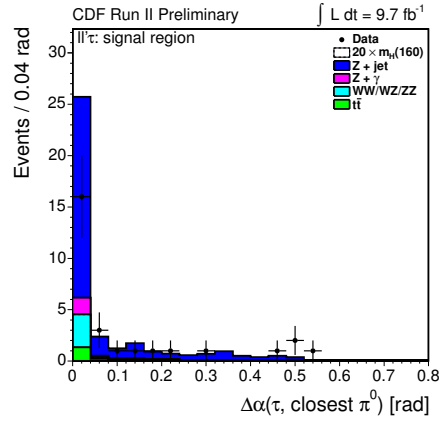
(a) p_T of the closest track to the τ .



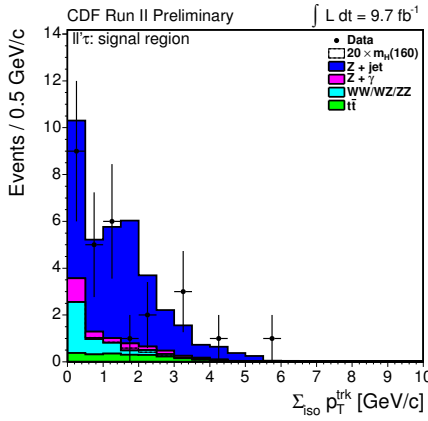
(b) Angle between the τ and the closest track.



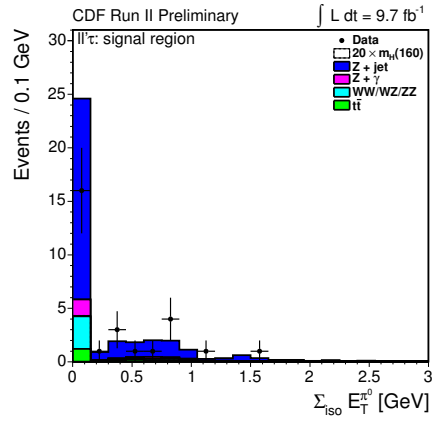
(c) E_T of the closest π^0 to the τ .



(d) Angle between the τ and the closest π^0 .



(e) Sum of p_T of all tracks in the τ isolation cone.



(f) Sum of E_T of all π^0 's in the τ isolation cone.

Figure B.18: Data-MC comparison in the trilepton signal region.

Bibliography

- [1] <http://www-cdf.fnal.gov/cdfsims/validation/cot/cotVal.html>.
- [2] T. Affolder et al. “CDF central outer tracker”. In: *Nucl. Instrum. Meth.* A526 (2004), pp. 249–299.
- [3] G. Ascoli et al. “Central Muon Level-1 Trigger Electronics”. In: (). FERMILAB-PUB-87-188-E.
- [4] B. Ashmanskas et al. “The CDF Silicon Vertex Trigger”. In: *Nuclear Instruments and Methods in Physics Research A* 518 (Feb. 2004), pp. 532–536. DOI: [10.1016/j.nima.2003.11.078](https://doi.org/10.1016/j.nima.2003.11.078). eprint: [arXiv:physics/0306169](https://arxiv.org/abs/physics/0306169).
- [5] U. Baur and E. L. Berger. “Probing the weak-boson sector in $Z\gamma$ production at hadron colliders”. In: *Phys. Rev. D* 47 (11 1993), pp. 4889–4904. DOI: [10.1103/PhysRevD.47.4889](https://doi.org/10.1103/PhysRevD.47.4889). URL: <http://link.aps.org/doi/10.1103/PhysRevD.47.4889>.
- [6] R. Blair et al. “The CDF-II detector: Technical design report”. In: (). FERMILAB-DESIGN-1996-01.
- [7] P. Gatto. “Performance of the new tracking system at CDF II”. MA thesis. University of Padova, 2001.
- [8] E. Gerchtein and M. Paulini. *CDF detector simulation framework and performance*. 2003. URL: <http://www.citebase.org/abstract?id=oai:arXiv.org:physics/0306031>.
- [9] C. M. Ginsburg. “CDF Run 2 muon system”. In: *The European Physical Journal C - Particles and Fields* 33 (0 2004). [10.1140/epjcd/s2004-03-1795-6](https://doi.org/10.1140/epjcd/s2004-03-1795-6), s1002–s1004. ISSN: 1434-6044. URL: <http://dx.doi.org/10.1140/epjcd/s2004-03-1795-6>.
- [10] F. Halzen and A. D. Martin. *Quark and Leptons: An introductory Course in Modern Particle Physics*. John Wiley & Sons INC, 1984.
- [11] Andreas Hoecker et al. “TMVA: Toolkit for Multivariate Data Analysis”. In: *PoS ACAT* (2007), p. 040. arXiv:[physics/0703039](https://arxiv.org/abs/physics/0703039).
- [12] Thomas Junk. “Confidence Level Computation for Combining Searches with Small Statistics”. In: *NUCL.INSTRUM.METH.A* 434 (1999), p. 435. URL: [doi:10.1016/S0168-9002\(99\)00498-2](https://doi.org/10.1016/S0168-9002(99)00498-2).
- [13] M. L. Mangano et al. “ALPGEN, a generator for hard multiparton processes in hadronic collisions”. In: *JHEP* 0307 (2003), p. 001. URL: [doi:10.1088/1126-6708/2003/07/001](https://doi.org/10.1088/1126-6708/2003/07/001).
- [14] S. Menzemer. “A tracking and alignment software package for the CDF II silicon detector”. MA thesis. University of Karlsruhe, 2002.

- [15] D. Mohl. “Physics and technique of stochastic cooling”. In: *Phys. Reports* 58 (1980).
- [16] B. P. Roe et al. “Boosted decision trees as an alternative to artificial neural networks for particle identification”. In: *Nuclear Instruments and Methods in Physics Research A* 543 (May 2005), pp. 577–584. DOI: [10.1016/j.nima.2004.12.018](https://doi.org/10.1016/j.nima.2004.12.018). eprint: [arXiv:physics/0408124](https://arxiv.org/abs/physics/0408124).
- [17] T. Sjöstrand, S. Mrenna, and P. Skands. “PYTHIA 6.4 physics and manual”. In: *Journal of High Energy Physics* 5 (May 2006), p. 26. DOI: [10.1088/1126-6708/2006/05/026](https://doi.org/10.1088/1126-6708/2006/05/026). eprint: [arXiv:hep-ph/0603175](https://arxiv.org/abs/hep-ph/0603175).
- [18] F. D. Snider. “Tracking at CDF: Algorithms and experience from Run I and Run II”. In: *Nuclear Instruments and Methods in Physics Research A* 566 (Oct. 2006), pp. 133–141. DOI: [10.1016/j.nima.2006.05.139](https://doi.org/10.1016/j.nima.2006.05.139).
- [19] I. Vila. “Performance and First Physics Results of the SVT Trigger at CDF II”. In: *ArXiv High Energy Physics - Phenomenology e-prints* (2003). eprint: [arXiv:hep-ph/0307165](https://arxiv.org/abs/hep-ph/0307165).